Sheri I. Imsdahl

Effect of Microdiscectomy on the Biomechanics of the Lumbar Facet Joints

Sheri I. Imsdahl

A dissertation submitted in partial fulfillment of
the requirements for the degree of

Doctor of Philosophy

University of Washington
2015

Reading Committee:

Randal P. Ching, Chair
William R. Ledoux
Nathan J. Sniadecki

Program Authorized to Offer Degree:
Department of Mechanical Engineering

University of Washington

Abstract

Effect of Microdiscectomy on the Biomechanics of the Lumbar Facet Joints

Sheri I. Imsdahl

Chair of the Supervisory Committee:
Research Associate Professor Randal P. Ching
Department of Mechanical Engineering

A microdiscectomy is the surgical standard of care for a lumbar disc herniation and is the most common lumbar spine surgery performed in the United States. The procedure can be done in "partial" (PD) and "subtotal" (SD) fashions, with the latter being the more aggressive of the two techniques. Currently, there is limited information regarding the effects of microdiscectomy on the biomechanics of the lumbar spine. As a first step in addressing this issue, this research aimed to understand how PD and SD affect the mechanics of the lumbar facet joints at the level of surgery.

The response of the facet joints was described by (1) the three-dimensional kinematics (3D) of the facets and (2) the strains in the capsular ligament surrounding the joint. These metrics were explored in two separate *in vitro* investigations using human cadaveric spinal specimens. In both studies, the specimens were tested with a spine simulator that applied pure moments to the superior vertebra while allowing unrestricted motion of the specimen. The specimens were tested during physiological motions of: flexion-extension (FE), lateral bending (LB), axial rotation, and combined FE with LB. The studies employed a repeated measures approach whereby each specimen was tested with its disc intact and in post-PD and -SD states. The kinematics of the facets were determined via a rigid-body, point-based registration technique; and the capsular strains were measured with a custom 3D digital image correlation system.

Of the two procedures, only SD was shown to significantly increase the motion of the facets and the strains in the capsular ligament. Increased motion could lead to mechanical overload of the facets, potentially resulting in degenerative changes at the joint and subsequent pain. Additionally, neuroanatomical studies have shown that the capsular ligament is innervated with mechanosensitive nociceptors. Thus, SD patients may also be at risk of experiencing pain that originates from the capsule. These potential outcomes should be weighed by clinicians when deciding on the best course of treatment for their patients.

Acknowledgements

There are many people who supported me throughout the completion of this degree, and I would like to take the opportunity to acknowledge them. I am sincerely grateful to my advisor, Dr. Randal Ching, for his exceptional mentorship during my graduate studies. His teaching and guidance were instrumental to both the success of this research and my development as an engineer. I have the utmost respect and appreciation for the level of care that he extends toward his students, and I am very thankful for having had the chance to work with him.

I am further indebted to the members of my doctoral supervisory committee (Dr. Peter Johnson, Dr. William Ledoux, and Dr. Nathan Sniadecki) for sharing their time with me and reviewing this dissertation. Their insightful comments and questions helped me think critically about my work and improve the overall quality of this dissertation.

I am very thankful for my fellow graduate students—both past and present—at the Applied Biomechanics Laboratory. In particular, I would like to thank Shannon Kroeker (who mentored me through the early stages of my degree) and my current “lab brothers” Jeff Campbell and Jed White. Graduate school would not have been nearly as enjoyable without them, and I am very grateful for their friendship and support.

Various parts of this research were definitely a group effort, and I was fortunate to work with some truly wonderful individuals. Foremost among my collaborators were Dr. Michael Lee and Dr. Richard Bransford. I am very appreciative of the roles they played in helping me undertake this research, as well as for giving me a glimpse into the world of orthopaedic surgery. I am especially indebted to Shizue Haffeman-Udagawa, who assisted me with specimen preparation and testing during a crucial point in my degree. The relative ease with which we completed testing was—in no small part—due to her presence and care for detail. I would also like to acknowledge Jane Shofer, who performed all the statistical analyses (on a very tight timeline!). I am grateful for her patience in talking through the results with me and furthering my understanding of statistics.

Finally, I would like to express my heartfelt appreciation for the steadfast encouragement of my friends and family. Special thanks are due to my youngest sister, Amy, who joined me at the University of Washington in 2012. I will forever be grateful for having had the chance to share my life in Seattle with her. And last—but certainly not least—I would like to acknowledge my parents, John and Rita, to whom this dissertation is dedicated. Thank you both for everything.

Table of Contents

List of Figures

List of Tables

Chapter 1. Introduction

1.1 Disc Herniation

Lumbar disc herniation is one of the most common causes of low back pain (LBP) and sciatica. It occurs when a tear forms in the outer layer of the intervertebral disc (annulus fibrosus), allowing the disc's inner gelatinous core (nucleus pulposus) to extrude outward beyond the disc space (Figure 1.1). The herniation typically occurs on the posterolateral side, where the annulus is relatively thin and the disc is not reinforced by either the anterior or posterior longitudinal ligaments [1]. Though herniations are usually the result of age-related annular degeneration and weakening, they can also arise from trauma, heavy lifting, and occupational driving of motor vehicles [2].

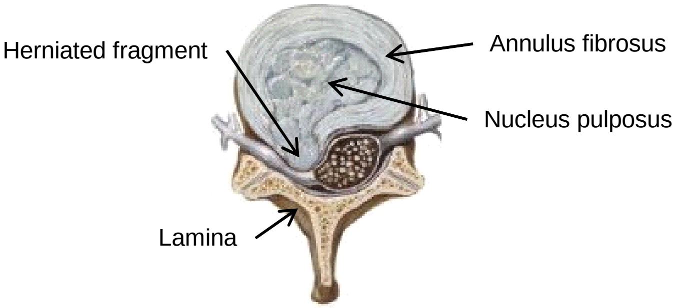

Figure 1.1: Cross-section of a herniated disc, depicting the breached annulus and a herniated fragment compressing on a nerve root. (Adapted from Hansen and Netter [3].)

Patients with symptomatic lumbar disc herniations generally present with acute or chronic intermittent LBP, sciatica, sensory changes, reflex loss, and muscle weakness. The mechanistic cause of pain tends to be multifactorial, involving: (1) mechanical stimulation of the nerve endings in the outer annulus, (2) compression of the spinal cord or its associated nerve roots, and (3) chemical inflammation induced by the herniated fragment [2].

1.2 Treatment

Though most patients can be treated successfully by nonoperative means, many opt for surgery out of a desire to quickly resolve their symptoms. Severe and progressive neurological and motor deficits are considered to be absolute indications for surgery. These situations are rare, however, and the majority of cases are not as straightforward. Nevertheless, most physicians would agree that the *relative* indications for surgery are: (1) failure of an adequate period of nonoperative treatment (generally 6 weeks to 4 months), (2) recurrent sciatica or neurological deficits after a successful period of nonoperative treatment, (3) a herniation into a stenotic spinal canal, or (4) intractable pain [4].

1.2.1 Microdiscectomy

A microdiscectomy is the surgical standard of care for a lumbar disc herniation. It is the most common lumbar spine surgery in the United States [5], with nearly 300,000 performed annually [6]. There are two methods of disc removal used for microdiscectomy procedures. The first, referred to as "subtotal" microdiscectomy (SD), was described by O'Connell [7] and involves excision of the herniated fragment with aggressive curettage of the disc space. Advances in surgical lighting and microscopy during the twentieth century promoted the development of a more conservative technique, known as "partial" microdiscectomy (PD). This approach, described by Williams [8] and Spengler [9], involves removal of the herniated fragment alone with minimal invasion of the disc space. Both procedures require partial resection of the lamina to allow the surgeon to see and access the site of herniation. [The laminae (left and right) are flat sheets of bone that project posteromedially from the pedicles and join at the midline to form the spinous process (Figure 1.1)].

1.2.2 Subtotal versus Partial Microdiscectomy

The choice between SD and PD remains unclear. SD, by nature of its more aggressive technique, has been criticized for injuring the nucleus and endplate, leading to accelerated degeneration and subsequent pain. On the other hand, PD has been criticized for increasing the risk of reherniation, since more disc material is left behind to potentially herniate later.

The literature seems to support both these claims. McGirt et al. [10] reviewed a number of previously reported case series and comparative studies in an effort to assess the short- and long-term outcomes after PD and SD. The authors reported similar short-term outcomes (6 months to 2 years postoperatively), with the incidence of recurrent back or leg pain being 14.5% and 14.1% for PD and SD, respectively. A significant increase in long-term (> 2 years postoperatively) back or leg pain was reported with SD versus PD (27.9% versus 11.6%, respectively; $P < 0.0001$). PD, however, was linked with a twofold increase in reherniation compared with SD (7% versus 3.5%, respectively; $P < 0.0001$). A comparable review by Watters and McGirt [11] had similar findings.

1.3 Significance

Currently, there is a paucity of data regarding the effects of microdiscectomy on the biomechanics of the lumbar spine. As a first step in addressing this issue, this study aimed to understand how PD and SD affect the mechanics of the lumbar facet joints.

From a clinical perspective, there were several reasons for undertaking this research. Throughout the human body, studies have shown a correlation between altered joint mechanics, degenerative processes, and pain. Clinical studies of the knee, for example, imply that abnormal motion often *precedes* degeneration, rather than the other way around [12–15]. Abnormal motion shifts loading to regions of the articular surface that are loaded infrequently and are thus poorly suited to accommodate the increased stress. This initiates a cascade of degenerative changes in the cartilage, which can ultimately manifest in osteoarthritis and pain [16–18]. Multiple researchers have hypothesized that kinematic changes at the facet joint could result in osteoarthritis, facet atrophy, and narrowing of the intervertebral foramen along a similar path [19,20].

In addition to osteoarthritis, altered facet joint mechanics may lead to pain stemming from the capsular ligament that surrounds the joint. Neurophysiological studies have revealed a population of small-diameter sensory neurons in the capsule that signal both the presence *and* magnitude of capsular strain due to joint motion [21]. In an electrophysiological study with goats, Lu et al. [21] found that approximately 47% strain is required to activate nociceptors within the capsule. However, because the researchers did not take any measures of behavioral sensitivity, it was unknown whether this threshold was also associated with the onset of pain. In fact, in two other studies, persistent allodynia (pain from a stimulus that is not normally painful) was seen in rats that experienced capsular strains of 33.6 ± 3.1% [22] and 21.5 ± 12.3% [23]. This suggests that the strain threshold for pain could be much lower than that reported by Lu et al. [21]. Based on the allodynia studies, it is reasonable to consider any strain above 21.5% as a potential source of pain. These investigations provide further rationale for studying facet joint mechanics, since nonphysiological motion could produce capsular strains that are sufficiently large to elicit pain.

Taken together, the aforementioned studies demonstrate the importance of understanding whether surgical disc excision affects the biomechanical response of the lumbar spine and—specifically—of the facet joints. The results of this research provide data for objectively comparing PD and SD while offering insights on whether either procedure might put the facet joints at risk for degenerative changes and pain.

1.4 Objectives and Hypotheses

As previously stated, the purpose of this study was to determine how PD and SD affect the mechanics of the lumbar facet joints *at the level of surgery*. The response of the facet joints was described by (1) the three-dimensional (3D) kinematics of the facets and (2) the strains in the capsular ligament surrounding the joint.

This research was conducted to test the following hypotheses:

- H_1: After PD and SD, the facets exhibit significantly more motion in response to physiological loads. The increases after SD are significantly greater than the increases after PD.
- H_2: After PD and SD, the capsular ligament experiences significantly greater strains in response to physiological loads. The increases after SD are significantly greater than the increases after PD.
- H_3: After SD, physiological loading produces strains in the capsular ligament that exceed the threshold for pain (21.5%) [23]. The strain threshold is not surpassed after PD.

1.5 Study Outcomes

The above hypotheses were evaluated using two separate investigations. The study outcomes were:

- Study #1: The 3D kinematics (translations and rotations) of the facets when the disc is intact and in post-PD and -SD states.
- Study #2: The full-field surface strains of the capsular ligament when the disc is intact and in post-PD and -SD states.

This document presents the research that was conducted for each of these studies (Study #1: Chapter 4 and Study #2: Chapter 6). For the second study, the capsular ligament strains were measured with an optical technique known as digital image correlation, or DIC. The design and validation of a custom 3D-DIC system are described in Chapter 5. Also included are: an introduction to lumbar spinal anatomy with particular emphasis given to the facet joint (Chapter 2); a summary of published studies on facet joint mechanics and mechanotransduction (Chapter 3); and a final discussion of the results to summarize the research (Chapter 7).

Chapter 2. Anatomy

2.1 Anatomy of the Lumbar Spine

The lumbar spine is one of five regions (cervical, thoracic, lumbar, sacrum, and coccyx) of the human spine. It is located below the thoracic region and directly above the sacrum. There are five vertebrae in the lumbar spine, which are referred to as L1-L5 traveling from top to bottom. Vertebrae vary in size and certain geometrical characteristics from one region to the next. However, a typical vertebra consists of a vertebral body, vertebral arch (pedicles and laminae), and seven processes (spinous process, two transverse processes, and four articular processes) (Figure 2.1). Mobility between any two vertebrae is provided by the intervertebral disc and two facet joints, thus defining the intervertebral joint as a three-joint system.

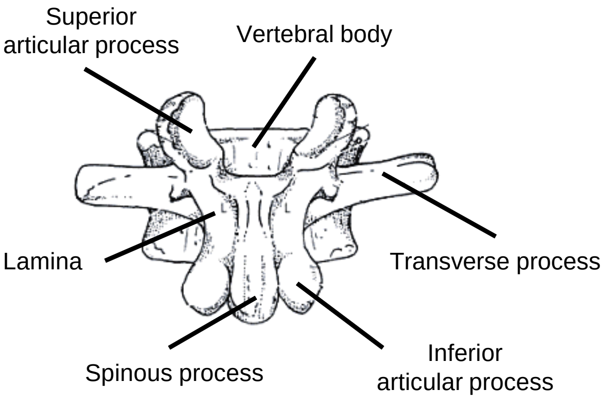

Figure 2.1: Lumbar vertebra. (Adapted from Bogduk [24].)

2.2 Anatomy of the Intervertebral Disc

The intervertebral discs are interposed between the bodies of adjacent vertebrae. They allow for the flexibility of the spine while acting as natural shock absorbers and transmitting the loads that arise from body weight and muscle activity. The disc is a complex structure comprised of two basic elements: the nucleus pulposus and the annulus fibrosus (Figure 2.2). The nucleus pulposus is the gelatinous core of the disc and consists of collagen and elastin fibers suspended in a highly hydrated aggrecan-containing gel. The hydrated proteoglycans are essential for maintaining the osmotic pressure of the disc, which imbues it with its load-bearing capabilities. The nucleus is surrounded by the annulus fibrosus, which is made up of dense rings (lamellae) of fibrocartilage that insert on the vertebral endplates. Each lamella has unidirectional fibers angled at approximately 60 deg to the vertical axis, with the orientation occurring in opposite directions in successive layers. In addition to containing the nucleus, the annulus functions to evenly distribute pressure across the disc and resist the stresses that arise from compression, bending, and torsion of the spine [25,26].

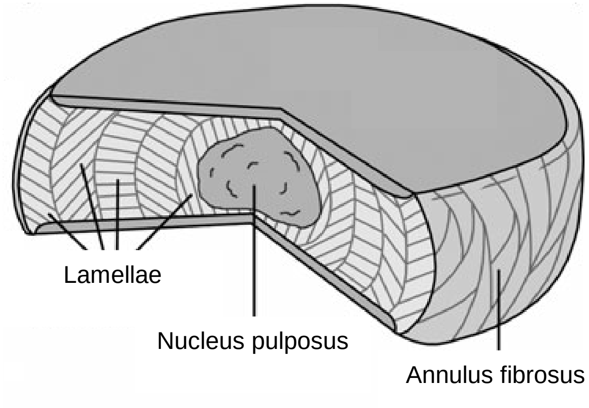

Figure 2.2: Structure of the intervertebral disc. (Adapted from Raj [26].)

2.3 Anatomy of the Lumbar Facet Joint

The lumbar facet joints are classified as true synovial joints and are formed by the articulation of the inferior articular processes of one vertebra with the superior articular processes of the vertebra below (Figure 2.3). The joints are comprised of both hard and soft tissues, including: (1) the bony articular processes whose articulating surfaces are covered with cartilage; (2) a thin connective tissue known as the synovium that borders the cartilage; and (3) a capsular ligament that envelops the entire joint. These tissues act together to guide and constrain the motion of the spine and transfer the loads applied to the spinal column.

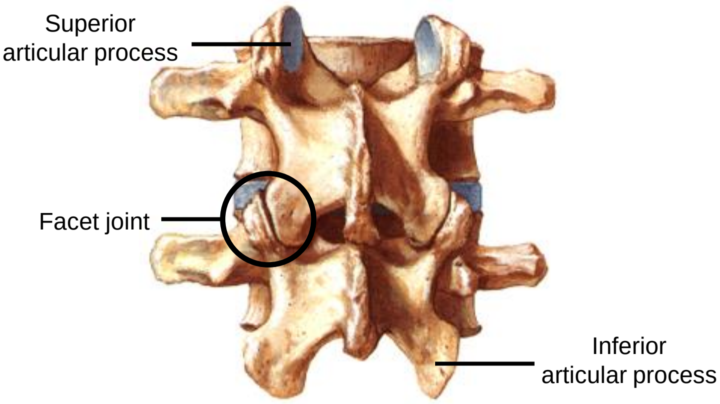

Figure 2.3: The facet joints are formed by the articulation of a vertebra's inferior articular processes with the superior articular processes of the vertebra directly beneath it. There are two facet joints (left and right) in each spinal motion segment. (Adapted from Thompson and Netter [27].)

2.3.1 Bony Articular Processes

The bony articular processes protrude from the laminae of each vertebra, forming two posterolateral columns that help support axial compressive loads along the spine.

The orientation of the articular surfaces varies with vertebral level. Masharawi et al. [28] studied thoracolumbar facet orientation using 240 human vertebral columns from the osteological collection of a museum. In the sagittal plane, they measured the angle between the facets and the posterior vertebral body height; and in the transverse plane, they measured the angle between the facets and the vertebral body length (Figure 2.4).

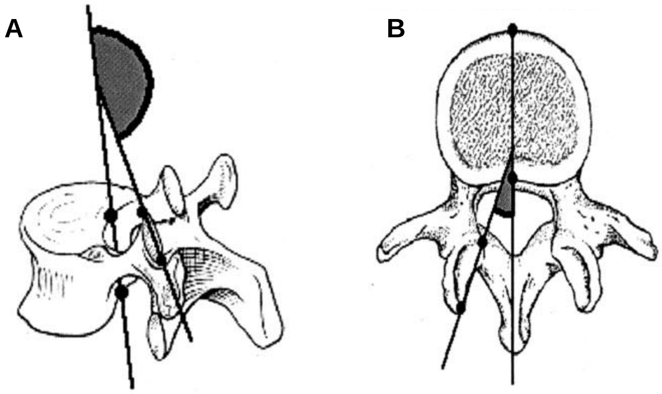

Figure 2.4: Angle of the facets in the (A) sagittal and (B) transverse planes. The angles are shown for the superior facets, though a similar process was adopted for the inferior facets. (Adapted from Masharawi et al. [28].)

According to their results, the sagittal angle remains fairly constant for the superior facets (~170º), whereas for the inferior facets, it steadily decreases from approximately 165º at L1 to 150º at L5. Consequently, as one moves down the spine, the orientation of the inferior facets in the sagittal plane becomes increasingly incongruent with that of the superior facets. This disharmony within joints does not manifest in the transverse plane. The superior and inferior facets of each vertebra are generally well aligned. The facets of L1 and L2 are closely oriented with the midsagittal plane (~30º). The facets of the lower lumbar levels are oriented less with that plane, with the angle gradually increasing to approximately 50º at L5.

The orientation of the articular surfaces has important implications for the kinematics of the spine. Because the lumbar facets are generally vertically inclined, the joints are most mobile under sagittal plane loading. During axial rotation, the opposing facets come into contact, resulting in smaller movements. Despite the decrease in flexibility, this resistance to axial rotation serves to protect the intervertebral disc and spinal cord from potentially damaging, nonphysiological motions.

2.3.2 Cartilage Layer

A thin layer of hyaline cartilage covers the articulating surface of each facet. The cartilage layer in the cervical facet joints has been researched more extensively than that of the lumbar facet joints. Yoganandan et al. [29] reported that the cartilage is thickest at the geometrical center of the facet and gradually thins outward, where a layer of subchondral bone is exposed at the outermost edge. The cartilage cover was stated to be 90% in the upper cervical spine (C1-C2) and 68% in the lower cervical spine (C3-C7). In general, the cartilage was thicker in the upper cervical spine, and a gender difference was noted. Accordingly, the mean thickness was 0.9 mm in males and 0.6 mm in females in the upper cervical spine, whereas in the lower cervical spine, it was 0.5 mm in males and 0.4 mm in females. Following these findings, Womack et al. [30] used experimental data from C3-C7 to develop a single analytical function that described the perimeter of the cartilaginous region and the cartilage thickness across the facet surface. The shape of the thickness distribution was found to be in good agreement with the mid-sagittal profile given by Yoganandan et al. [29]. Recently, Woldtvedt et al. [31] used the methods of Womack et al. [30] to describe the three-dimensional (3D) distribution of cartilage thickness in the lumbar facet joints. The mean thickness was reported to be 0.58 mm and 0.63 mm for the inferior and superior facets, respectively.

The cartilage layer enables nearly frictionless motion between the articulating surfaces while supporting compressive, tensile, and shear loads that develop across the joint. Its function is largely due to the structure of the cartilage tissue. Articular cartilage is a composite material, consisting of fluid (water) and solid (chondrocytes, collagen fibers, and proteoglycans) phases. Through the depth of the cartilage there are three distinct zones, each with a unique structural organization and mechanical function (Figure 2.5). The outermost layer, called the lamina splendens, is the region where contact occurs with the opposing facet. It is sparsely populated with chondrocytes and collagen fibers that are oriented tangentially to the surface. The orientation of the collagen fibers allows the cartilage to resist the tensile and shear stresses that develop when the facets slide relative to one another. The middle layer, or transitional zone, contains an increased number of chondrocytes and larger collagen fibers that are arranged in a random fashion. In the final layer, or deep zone, the chondrocytes are stacked in columns that are perpendicular to the surface and parallel to the collagen fibers. The transitional and deep zones contain a high concentration of proteoglycans, which increases with depth. The proteoglycans attract water, which improves the incompressibility of the material. Therefore, these layers resist the compressive and hydrostatic stresses that develop in the joint [32].

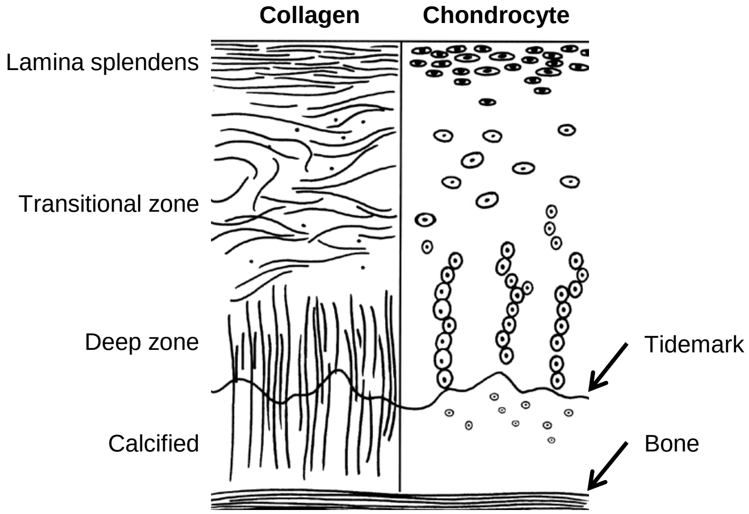

Figure 2.5: Layered structure of articular cartilage. The appearance and organization of the collagen fibers and chondrocytes are shown on the left and right, respectively. (Adapted from Browne and Branch [33].)

2.3.3 Synovium and Menisci

The synovium is a thin connective tissue that surrounds the margins of the articular cartilage. In addition to providing mechanical resistance to the relative motion of the facets, the synovium is responsible for producing and secreting synovial fluid to nourish the cartilaginous surfaces and minimize the friction between them. The synovium also regulates exchanges between blood and the synovial fluid and contains macrophages to remove waste that accumulates in the joint cavity.

Examined from the inside of the joint, the synovial membrane has a smooth surface, but in some areas, it forms folds which project into the joint space. Also called menisci, the synovial folds help protect the articular cartilage (Figure 2.6). Because they are wedged between the opposing articular surfaces, they help compensate for any incongruencies between them. The folds also provide increased surface area on which to distribute the loads that are transferred through the joint. There are three types of menisci which are present in the facet joints: adipose tissue pads, fibro-adipose meniscoids, and connective tissue rims. The adipose tissue pads and fibro-adipose meniscoids are located on the peripheral rims of the superior and inferior regions of the joint. In the sagittal plane, they have a triangular cross-section. The base of the triangle is attached to the capsular ligament, and the apex extends into the joint cavity by as much as 4 mm. The connective tissue rims wrap around the remaining portion of the bony processes with a slight inward taper [34].

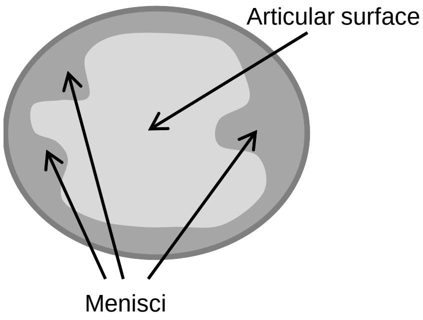

Figure 2.6: Idealized sketch of a facet's articular surface showing the menisci protruding into the joint space.

2.3.4 Capsular Ligament

The capsular ligament surrounds the synovium to completely enclose the facet joint. The lumbar facet capsule has non-uniform thickness and has been reported to be thinner in the posterior region

(2.0 mm) than the superior and inferior regions (2.4 mm) [35]. In a morphological study by Yamashita et al. [36], the authors identified two distinct layers in the capsule. The outer layer is a strong connective tissue formed by dense bundles of collagen fibers linked by proteoglycans. The inner layer is composed of elastin fibers interspersed with fibroblasts. Its histological features are similar to those of the ligamentum flavum, which blends with the fibers to form the anterior aspect of the capsule.

The morphology of the capsule is highly dependent on location. Though the outer layer contains parallel bundles of fibers, the fiber lengths and directions are different in the superior, middle, and inferior portions of the joint. In the superior and middle parts, the fibers are 13-17 mm in length and run in the mediolateral direction. In both these regions, the medial ends of the fibers attach to the posteromedial aspect of the lamina. However, in the superior region, the lateral attachment is at the superolateral aspect of the superior articular process; and in the middle region, it is at the posterior aspect of the mamillary process. In the inferior portion of the joint, the fibers are 15-20 mm long and run in the superomedial to inferolateral direction. The medial ends of the fibers attach to the inferomedial aspect of the lamina, and the lateral ends attach to the posterior aspect of the base of the superior articular process [36].

The purpose of the capsular ligament is to resist tensile forces that develop when the joint rotates and translates. Because the fibers cross over the joint gap and are generally oriented in the mediolateral direction, they permit mobility in the sagittal plane while helping to stabilize the joint in the transverse plane.

Chapter 3. Facet Joint Mechanics and Mechanotransduction

3.1 Mechanics of the Lumbar Facet Joints

There are several studies that have focused on the mechanics of the facet joint separate from those of the intervertebral joint. Their metrics can be broadly grouped into three main categories, which include:

- Facet kinematics.
- Capsular ligament strains.
- Facet contact forces and pressures.

Though all these metrics are interrelated, in the lumbar spine, the first two categories have been less studied than the third and are thus the focus of this investigation. The following subsections document and summarize the current state of knowledge regarding these metrics.

3.1.1 Facet Kinematics

Only a handful of studies have made quantitative measurements of lumbar facet kinematics. Wood et al. [37] used an instrumented spatial linkage to measure facet motion in dogs during various functional activities. During walking, they observed that the opposing facets at L2-L3 glided over one another in a ventral to dorsal slope, with an average excursion of 3.4 ± 1.3 mm. This was a landmark study in the sense that it was the first investigation to numerically characterize the motion of the lumbar facets. However, there are substantial differences between canine and human lumbar spines, in terms of their relative proportions [38], orientations, and mechanical properties [39]. Thus, it is difficult to draw inferences from Wood et al.'s [37] results on the kinematics of *human* lumbar facets.

In a later study, Kozanek et al. [40] employed a dual MRI modeling and fluoroscopic image matching technique to measure the range of motion (ROM) of human lumbar facets *in vivo*. Subjects performed maximal trunk bending along the three primary axes of motion [flexion-extension (FE), lateral bending (LB), and axial rotation (AR)] under physiological weight-bearing. The researchers found that facet motion was dependent on vertebral level. Whereas the facets of the cranial levels

(L2-L3 and L3-L4) were more mobile in FE, the facets at L4-L5 were more mobile in LB and AR. During FE, the facets primarily rotated about the mediolateral axis (mean: 2.0-6.0 deg) and translated in the superoinferior direction (mean: 2.0-4.0 mm). In contrast, during LB and AR, the facets did not rotate or translate in a dominant direction. Rather, their motion constituted a coupling of rotations (mean: < 5.0 deg) and translations (mean: 3.0 mm) in different directions.

Kozanek et al. [40] described facet motion in a coordinate system whose axes were aligned with the anatomical directions of the body. This reference frame is well-understood from a clinical point of view. However, since the facets are not oriented with any of the conventional anatomical planes, it does not explicitly provide information on facet articulation and separation. To address this issue, Jegapragasan et al. [41] developed a facet-based coordinate system oriented with the surface of the facets, such that facet in-plane and out-of-plane motion could be described. To demonstrate the utility of this reference frame, the researchers performed an *in vitro* study with human cadaveric lumbar spines (L1-S1). Specimens were subjected to 7.5 Nm bending moments in FE, LB, and AR, and facet translations were measured at each vertebral level. Regardless of level or side, the researchers found that under each loading condition, the facets predominantly translated in a single direction. In FE and LB, it was in the superoinferior direction along the plane of the opposing facet; and in AR, it was normal to this surface. These results contradicted the findings of Kozanek et al. [40], which showed more variability due to changing facet orientation along the length of the lumbar spine [28,42]. Despite this difference, the total magnitude of translation was similar between studies.

3.1.2 Capsular Ligament Strains

Straining of the capsular ligament results from vertebral motion and activation of the paraspinal muscles, which surround the joint and insert on portions of the capsule [43,35,44]. Capsular strains in the cervical and lumbar spines have been shown to reach large values without any macroscopic evidence of damage or failure [45–47]. This implies that the capsule is strong and highly effective at resisting vertebral rotations and translations.

Only two studies have measured capsular strains in the lumbar spine. Both were performed *in vitro* with human cadaveric specimens. Panjabi et al. [45] applied 15 Nm bending moments to lumbar functional spinal units (FSUs) about each of the three principal axes of motion. The capsule was modeled as a series of straight-line segments based on the direction and attachment points of the fibers, which were identified with a three-dimensional (3D) morphometer. After testing, the measured vertebral motion was applied to the capsule model to determine each segment's change in length during the tests. The authors reported the average strains computed from the length data. A later study by Ianuzzi et al. [47] tested full lumbar spinal specimens (T12-S1) using a custom-built displacement-controlled loading apparatus. Specimens were subjected to FE and LB by horizontally displacing T12. Capsular plane strains were measured by optically tracking an array of markers that were glued to the surface of the capsule. The measured displacements were then incorporated into a two-dimensional (2D) isoparametric finite element model previously developed for measuring soft tissue strains [48].

The results of these studies are summarized in Table 3.1. The strains published by Panjabi et al. [45] are the mean maximum uniaxial strains from a pool of FSUs from two different levels. In contrast, Ianuzzi et al. [47] tested full lumbar spines and measured the principal strains at every level. For brevity's sake, Table 3.1 only provides data for the level where the maximum (positive) principal strain occurred.

Table 3.1: Summary of studies that have measured the capsular ligament strains in the lumbar spine.

Study	**Loading**		**Strain (%)**		**Level(s)**	
	Direction	*Magnitude (Nm)*				
Panjabi et al. [45]			Left	Right		
	Flexion	15	17.5	12.8	L3-L4 L4-L5	
	Extension		8.2	8.4		
	Right LB		9.5	2.4		
	Left LB		3.9	1.8		
	Clockwise AR		-13.9	17.0		
	Counterclockwise AR		19.3	-13.6		
Ianuzzi et al. [47]*			Left	Right	Left	Right
	Flexion	3	14.6	**14.2**	L4-L5	L5-S1
	Extension	5	7.7	**7.0**	L2-L3	L2-L3
	Right LB	4.5	8.6	9.4	L4-L5	L2-L3
	Left LB	5.5	**4.9**	**8.5**	L2-L3	L5-S1

*Moments are at L5-S1 at 40 mm of horizontal displacement of T12.
Strains are the maximum (positive) principal strains at 40 mm of horizontal displacement of T12.
Bolded values were estimated from graphs using ImageJ (National Institutes of Health, Bethesda, MD, USA).

It is difficult to directly compare the results from these studies because of their differences in methodology. Nevertheless, a few key observations were made. To begin with, both Panjabi et al. [45] and Ianuzzi et al. [47] emphasized the high level of variability in their data. The standard deviations were routinely on the same order of magnitude as the mean measurements themselves. (For instance, in left LB, Ianuzzi et al. [47] reported a maximum principal strain of 8.5 ± 7.0% in the right capsules of L5-S1.) Despite the variation, in both studies, the average strains were consistently less than 20%.

The second observation was that the strains measured by each group were comparable to one another even though the studies subjected their specimens to considerably different loads. Panjabi et al. [45] tested their specimens with 15 Nm bending moments. (This is on the higher end of what is normally used in *in vitro* studies but is still considered to be within the physiological range. For example, Adams and Dolan [49] determined that a peak bending moment of 12 Nm occurs at L5-S1 when a person flexes forward to retrieve a pen off the floor, and this moment increases as the object becomes heavier or bulkier.) In contrast, the peak bending moments applied by Ianuzzi et al. [47] were only 20-35% as large (range: 3-5.5 Nm). This result is likely due to the sigmoidal relationship between intervertebral joint angle and joint moment. For larger moments, the intervertebral angle tends to plateau, and there is a minimal increase in angle with increasing moment. Because the two studies reported similar intervertebral angles in their specimens (at the maximum applied loading), it is reasonable that they would also measure similar capsular strains.

3.2 Mechanotransduction in the Facet Joint

Mechanotransduction refers to the conversion of a mechanical stimulus into a physiological response such as pain. There are a variety of mechanisms by which this can occur, and the response can be felt across several scales, from the macroscopic tissue-level to the cellular and molecular levels [50]. Depending on the situation, mechanotransduction can contribute to the control and maintenance of the various tissues in the joint [51–54], or, it can lead to their malfunction and degeneration [55,56].

The mechanisms of mechanotransduction have been described in several synovial joints, including the facet joint. Mechanical loading of the facet joint primarily produces stretching of the capsular ligament and compression of the cartilaginous articular surfaces and subchondral bone.

Neuroanatomical studies have demonstrated that the capsular ligament is densely populated with mechanosensitive afferent units, and the morphology of many of them fit the profile of nociceptors. Thus, in the interest of identifying sources of low back pain (LBP), the mechanotransduction studies that specifically address the facet joint have focused exclusively on the capsular ligament.

3.2.1 Innervation of the Capsular Ligament

There are four main types of sensory nerves, which are classified according to their morphological and functional characteristics. Types III and IV serve as nociceptors because they are involved in pain sensation; however, each has several other functions such as temperature and crude touch sensations. Type III fibers are 1-5 μm in diameter and thinly myelinated with fast conduction velocities (2.5-20 m/sec) for transmitting information about the onset of pain. Type IV fibers are 0.5-2 μm in diameter and unmyelinated with slow conduction velocities (< 2.5 m/sec) for transmitting information about ongoing pain. Both have unencapsulated endings [57]. The presence of either of these fibers in a spinal tissue provides a structural basis for marking that tissue as a possible source of LBP.

Several histological studies have assessed the innervation of human lumbar facet capsules. Ashton et al. [58] found that facet capsules from the lower lumbar levels were immunoreactive to two neuropeptides (substance P and calcitonin gene-related peptide) that mediate the transmission of pain in the peripheral nervous system. Furthermore, all the immunoreactive nerves were less than 2 μm in diameter, consistent with the morphology of nociceptors. In a later study, McLain and Pickar [59] harvested thirteen facet capsules from L1-L4 and observed Type IV nerve endings in every specimen. The authors did not quantify their exact distribution; however, their findings seem to corroborate those of Ashton et al. [58].

Though the aforementioned studies identified likely nociceptors in the human lumbar facet capsule, neither identified their stimulus modalities. All nociceptors initiate the sensation of pain, but they can be differentiated according to whether they are sensitive to mechanical, thermal, or chemical stimuli [60]. In the field of mechanotransduction, the units of interest are those that respond to mechanical pressure or deformation of the receptor or adjacent tissue.

To that end, neuroanatomical studies have revealed mechanosensitive afferent units in the lumbar facet joints of several species, including the rat [61], rabbit [62,63], and cat [64]. In their study of the rabbit, Yamashita et al. [62] identified twenty-four mechanosensitive units at the facet joint and twelve in the surrounding muscles and tendons. Of the twenty-four units at the joint, ten were in the capsule, twelve were along the border of the capsule, and two were in the ligamentum flavum, which forms the anterior aspect of the capsule. Based on their conduction velocities, 63% of the units at the joint were classified as Type III and 8% as Type IV, with the remaining 29% having a conduction velocity greater than 20 m/sec. In general, the units at the joint had a higher mechanical threshold and lower conduction velocity than those in the muscles and tendons, indicating that they were potential nociceptors.

3.2.2 Mechanotransduction in the Capsular Ligament

With the innervation of the lumbar facet capsule well established, many researchers have turned to examining *how* these fibers respond to mechanical stimuli. Because of the difficulty in performing neurophysiological studies with humans, much of this work has been done with animal models. In an *in vivo* study with rats, Cavanaugh et al. [61] found that by probing the lumbar facet capsule, they were able to elicit slow-adapting neuronal responses from afferents in the capsule. In half of the rats studied, afterdischarges occurred, lasting from a few seconds to more than two minutes. Pickar and McLain [64] similarly observed responses from L5-L6 capsular afferents in the cat when distracting the joint in various directions. Both studies clearly demonstrated the existence of mechanosensitive afferents in the capsule; however, they were limited in that they did not quantify the exact mechanical stimulus being applied.

To bridge this gap, Lu et al. [21,65] created an *in vivo* goat model that allowed them to measure the 2D principal strains at the receptive fields of capsular afferents while applying craniocaudal stretch at the joint. In a study with nine goats [21], the authors identified thirty-two Type III and twenty-five Type IV units at C5-C6. Approximately half of these units responded to stretch with low strain thresholds (10-11%). Two (8%) of the Type IV units responded only to high strain thresholds ranging from 34-58% (mean: 47%). The remaining units were unresponsive even at the maximum stretch, which produced strains between 34 and 60%. The authors hypothesized that the low-threshold units were proprioceptors, responsible for signaling the presence and magnitude of joint motion within physiological ranges, while the high-threshold and silent units were nociceptors. The joint was not stretched to catastrophic levels, so the silent units may have had a very high strain threshold. Alternatively, it is possible that they could have been activated under inflammatory conditions, which have been shown to increase the mechanosensitivity of capsular afferents [66,67].

Lu et al. [21,65] established a quantitative relationship between strain and nerve discharge in cervical facet capsules. Though their work demonstrated that subcatastrophic stretch could activate potential nociceptors, it was unknown whether this would actually result in pain. Insights to this question were provided by an *in vivo* rat model developed by Lee et al. [22,68] in which craniocaudal distraction was applied across the C6-C7 joint. Forepaw allodynia was assessed for seven days postoperatively and used as a measure of behavioral sensitivity. Over the entire postoperative period, rats subjected to high capsular strains (33.6 ± 3.1%) exhibited significantly more allodynia than rats that experienced low strains (11.1 ± 2.3%). Furthermore, the allodynia observed with the low strain group was not significantly different than the allodynia seen with a sham group [22]. In a later study using the same model, Dong et al. [23] found that capsular strains as low as 21.5 ± 12.3% were sufficient to reliably induce allodynia and activate the integrated stress response in neurons of the dorsal root ganglion. These results suggest the existence of a mechanical threshold for tensile loading above which persistent pain is produced.

Finally, of particular note is a study by Winkelstein and Santos [69] using the aforementioned pain model with the rat. While previous work with this model implied a link between excessive capsular strain and pain, no study had investigated whether ligament tension was *required* to initiate pain from joint distraction. To address this issue, the authors applied distraction at C6-C7 after transecting the left facet capsule while leaving the right joint untouched. Throughout the seven-day postoperative period, increased allodynia was seen in the forepaw on the side with the intact capsule. It was significantly greater than the allodynia on the side with the cut capsule as well as the allodynia observed in a sham group. Additionally, there was no difference in allodynia between the cut or sham groups on any day. These results provide strong evidence that the capsular ligament plays a role in mechanically sensing and transducing painful loading conditions of the joint.

3.3 Summary

Previous biomechanical studies have shown that under physiological loads, the lumbar facets exhibit rotations and translations of considerable magnitude [37,40,41], and their motion produces strains in the capsular ligament surrounding the joint [45,47]. Though these studies provide initial insights into the mechanics of the lumbar facet joint, there are many questions that remain unanswered. This investigation sought to resolve some of these questions as well as improve upon the existing experimental methods. Specifically:

- The current body of work has focused exclusively on non-pathological spines; thus, foremost among the questions is whether the mechanics of the facet joint are affected when the disc is structurally disrupted. Addressing this issue would provide a more complete picture of the relationship between the various components of the intervertebral joint.
- The mechanics of the facet joint—and even more broadly, of the spine—are ill-defined for bending moments applied outside of the sagittal, coronal, and transverse planes. Because the normal physiological motion of the spine is generally multi-axial, this is an area that merits further investigation.
- There are many improvements that can be made in the measure of capsular ligament strains. The morphology of the capsule is highly dependent on location, with fibers ranging from 13-20 mm in length [36]. Panjabi et al. [45] modeled the capsule as a series of five straight-line segments, which is a gross simplification of its actual geometry and ignores the tissue's inhomogeneity [70]. Furthermore, inaccurate identification of the fibers' insertion points could have led to significant errors in the researchers' strain calculations. Ianuzzi et al. [47] employed a more sophisticated optical technique to measure capsular strains. However, it required the use of markers, whose presence and attachment may have altered the deformation of the underlying tissue. Additionally, the researchers used an unconventional method to load their specimens. This resulted in intervertebral joint moments on the lower end of what is considered to be the physiological range [49,71] and makes comparison with other biomechanical studies more difficult. Many of these shortcomings could be addressed by utilizing a non-contact strain measurement technique and exploring more physiological loading conditions.

Finally, with regard to mechanotransduction, the literature contains evidence that supports the theory of lumbar facet pain that is capsular in origin. A population of small-diameter sensory neurons has been identified in the lumbar facet joints of several species, and they have been shown to respond to mechanical stimulation due to joint motion [58,59,61–64]. An electrophysiological study with goats determined a strain threshold of approximately 47% to activate nociceptors within the capsule [21]. However, persistent allodynia has been produced in rats that experienced capsular strains of 33.6 ± 3.1% [22] and 21.5 ± 12.3% [23]. Thus, the threshold to produce pain may actually be much lower than the value quoted by Lu et al. [21]. Lastly, it has been demonstrated that an intact capsule is requisite for joint distraction to produce allodynia in rats [69]. Taken together, these studies reinforce the importance of capsular ligament loading as both a means of mechanotransduction within the joint and a source of pain. This provides further motivation for quantifying capsular ligament strains in pathological states and after surgical disc excision.

Chapter 4. Study #1: Facet Kinematics

4.1 Overview

The purpose of Study #1 was to measure the three-dimensional (3D) kinematics of the lumbar facets when the disc is intact and after the disc has undergone partial (PD) and subtotal (SD) microdiscectomies. This was accomplished through a controlled laboratory experiment using cadaveric spinal specimens and a repeated measures approach. The study was designed to test the following hypothesis:

- H_1: After PD and SD, the facets exhibit significantly more motion in response to physiological loads. The increases after SD are significantly greater than the increases after PD.

This chapter explains the experimental work, data processing, and analysis that were carried out in pursuit of this hypothesis (Sections 4.2 and 4.3). It then presents the results (Section 4.4) and examines them within the context of previous investigations that have made quantitative measurements of lumbar facet kinematics or looked at the effects of disc removal on lumbar spinal motion (Section 4.5). Further discussion of the research—including its clinical implications—is included in Chapter 7.

4.2 Methods

A total of nine unembalmed human cadaveric lumbar specimens were chosen for this study. The specimens were tested in two separate groups. The first had six (n = 6) L2-L5 specimens, and the second had three (n = 3) T12-L4 specimens. Though the specimen preparation and methods were slightly different between groups, the basic testing protocol and kinematic measurements at the index level (L3-L4) were the same. The following subsections describe the methodology in more detail.

4.2.1 Specimen Preparation

The nine specimens came from seven males and two females, whose ages ranged from 52 to 75 years with a mean age of 64 years. Each specimen was dissected free of all non-ligamentous soft tissue, and visual and radiographic screening were conducted to rule out any pre-existing pathology that might alter the segmental kinematics. Four fiducial markers were rigidly attached to each vertebra on its body, transverse processes, or laminae. The chosen fiducial markers were 4-mm diameter non-metallic CT beads (for the L2-L5 specimens) and orthopaedic bone screws (for the T12-L4 specimens). The beads were placed by burring shallow 4-mm diameter cavities into the bone (with a 4-mm diameter spherical drill bit) and securing the bead in the cavity with cyanoacrylate glue.

After the fiducial markers had been implanted, the specimens were prepared for multi-segmental testing. Metal screws were inserted into the terminal ends of the specimen's superior- and inferior-most vertebrae. The ends were then embedded in polymethylmethacrylate with the screws providing increased fixation with the potting compound. The specimens were potted so that the axial midline of the L3-L4 disc (the index level) was parallel to the horizon.

4.2.2 Testing Equipment

Testing was performed using a custom-designed spine simulator capable of imparting pure bending moments about a single axis or combined loading about multiple axes [72] (Figure 4.1). The specimen's superior-most vertebra was rigidly fixed to a gimbal equipped with three rotary actuators (Model FHA-17C, HD Systems, Hauppauge, NY, USA) that were independently controlled by a LabView (National Instruments Inc., Austin, TX, USA) program to induce sagittal, coronal, or transverse plane moments. The gimbal and actuator assembly floated on a series of air bearings, allowing it to freely displace with the specimen. The forces and moments transmitted through the specimen were measured by a six-axis load cell (Omega 160, ATI Industrial Automation, Apex, NC, USA) beneath the inferior-most vertebra. The load cell was connected to a data acquisition board (Model PCI 6034E, National Instruments Inc., Austin, TX, USA) that sampled at a rate of 100 Hz.

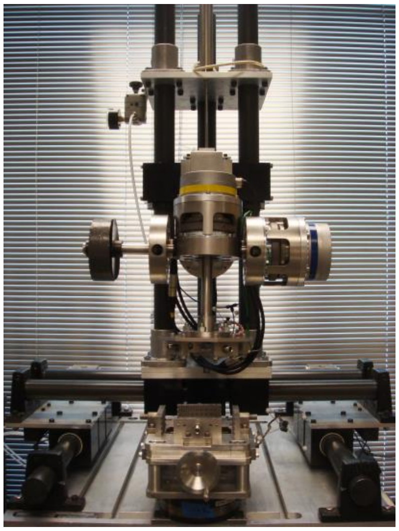

Figure 4.1: Multi-axis spine simulator.

Segmental kinematics were collected by attaching a set of four retro-reflective markers to each vertebra. The superior- and inferior-most marker sets were attached to the upper and lower simulator fixtures to which the specimen was mounted. The intervening marker sets were attached to the vertebral bodies by wires, which were held in place with screws (Figure 4.2). The marker sets were tracked with a four-camera Vicon MX13 system (Vicon Motion Systems, Lake Forest, CA, USA) sampling at a rate of 60 Hz. Within the cameras' field of view, the resolution of the system is approximately 0.05 mm/pixel.

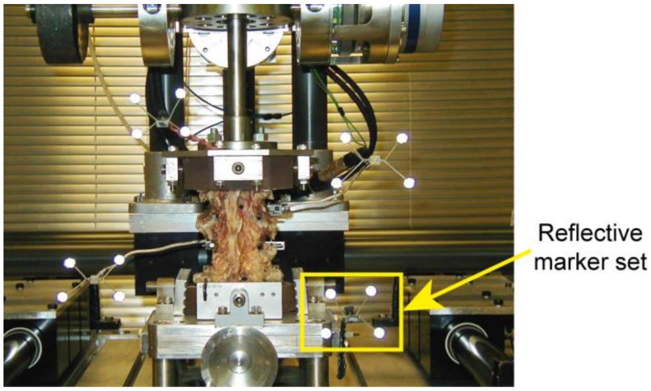

Figure 4.2: Potted specimen mounted in the spine simulator with a reflective marker set at each vertebral level.

4.2.3 Testing Protocol

Prior to testing, the fiducial markers (CT beads or orthopaedic bone screws) were digitized with a custom stylus fitted with four retro-reflective Vicon markers (Figure 4.3). For each vertebra, this process established the locations of its fiducial markers relative to its reflective marker set. This allowed the experimentally-acquired segmental kinematics to be registered with the 3D anatomical model of the specimen that was created after testing.

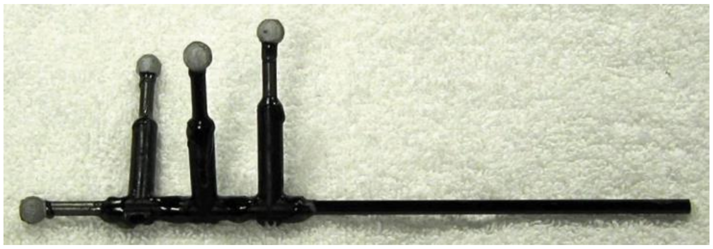

Figure 4.3: Vicon stylus used to digitize the CT bead fiducial markers. The tip of the stylus was machined to fit the spherical surface of the CT bead and calibrated to measure its center. The stylus used to digitize the orthopaedic bone screw fiducial markers had a pointed tip that fit into a small divot on the screw head.

The specimens were tested in: (1) their intact condition and post- (2) PD and (3) SD. Both surgical procedures were performed at L3-L4 by an orthopaedic surgeon and involved a posterolateral approach on the left side with partial resection of the lamina. For each of these conditions, the specimens were tested to maximum moments of: ±10 Nm in flexion-extension (FE), lateral bending (LB), and axial rotation (AR) [49,71]. Two multi-axis tests were also performed (FRLB and FLLB) in which FE and LB moments were applied simultaneously to the same limit (7 Nm) to produce a pure, off-axis bending moment with a vector-summed limit of approximately 10 Nm ($[(7\text{ Nm FE})^2 + (7\text{ Nm LB})^2]^{1/2} \approx 10$ Nm) (Figure 4.4). For the FRLB test, flexion was applied with right LB followed by extension with left LB. The FLLB test examined the opposite scheme (flexion with left LB followed by extension with right LB). The tests were conducted under continuous angular displacement control (2 deg/sec). All the tests had three complete motion cycles. The first two cycles were meant to precondition the specimen, and the third cycle was used for analysis. Figure 4.5 provides a visual representation of the entire testing protocol. Each specimen was tested over the course of several hours in a single day.

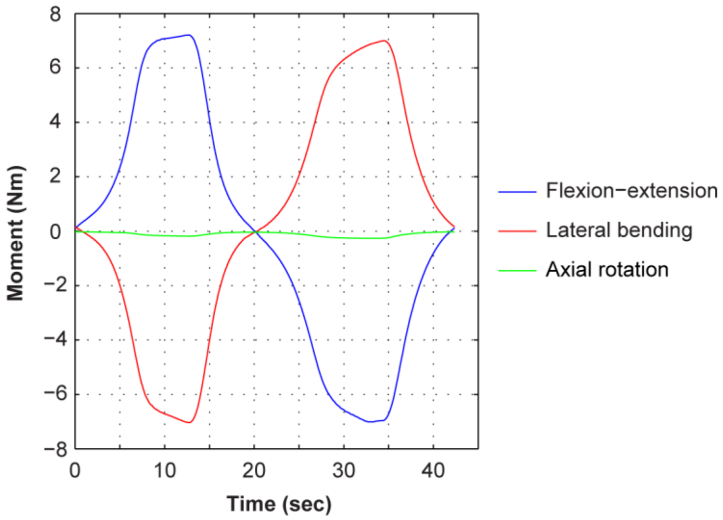

Figure 4.4: Exemplar load profile from one of the combined FE with LB tests (FLLB). The FE and LB moments were applied concurrently to the same limit (7 Nm) to produce an off-axis bending moment with a vector-summed limit of approximately 10 Nm.

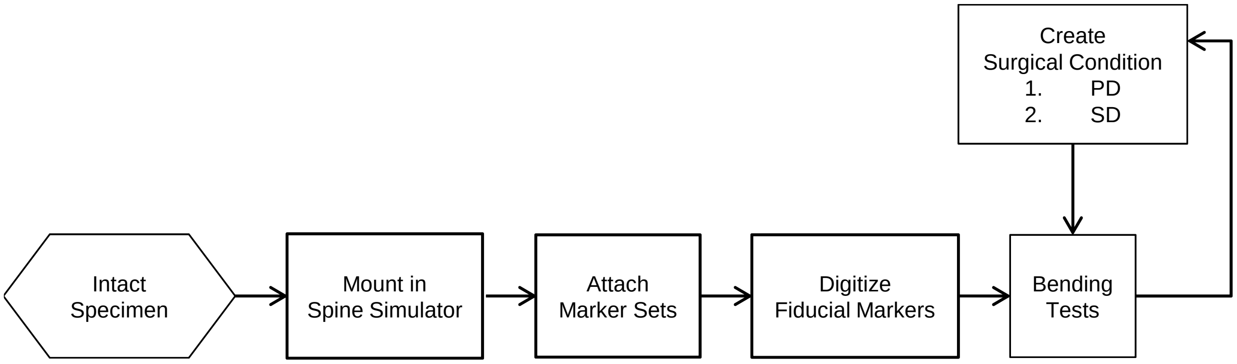

Figure 4.5: Flowchart of the testing protocol.

4.2.4 Three-Dimensional Anatomical Model

A 3D anatomical model was created for each specimen. The method of development was different for the L2-L5 and T12-L4 specimens due to the type of fiducial marker chosen for each group (CT beads versus orthopaedic bone screws, respectively).

The L2-L5 specimens were CT scanned after placement of their fiducial markers. Imaging was done in a GE LightSpeed VCT scanner (GE Healthcare, Waukesha, WI, USA) with 0.6 mm slice thickness and spacing using a bone algorithm. The data sets were segmented with SegVue (SegVue Inc., Seattle, WA, USA) to obtain a 3D reconstruction of each specimen with the attached fiducial markers (Figure 4.6). The segmented models were exported in stereolithography (STL) format and then imported into a 3D computer-aided design program (Blender, Blender Foundation, Amsterdam, Netherlands) for visualization and analysis.

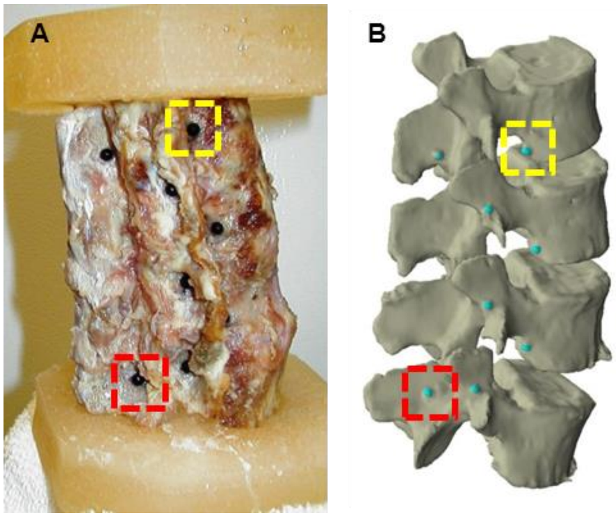

Figure 4.6: (A) L2-L5 specimen with (B) its 3D anatomical model obtained by CT scanning and segmentation. Corresponding fiducial markers (CT beads) on the L2 (yellow) and L5 (red) vertebral bodies are highlighted in each figure.

Due to budgetary constraints, the T12-L4 specimens were not imaged. At the conclusion of mechanical testing, the index level vertebrae (L3 and L4) were disarticulated from each specimen. The L3-L4 facet joints and endplates were carefully cleaned of all cartilaginous material. Each vertebra's fiducial markers, facets, and endplate were then digitized with a Polhemus FASTRAK system (Polhemus, Colchester, VT, USA). The anatomy was captured by slowly sweeping the tip of the digitizing stylus (Figure 4.7) across the facet and endplate surfaces while continuously collecting data with the Polhemus system. Approximately 13,000 data points were taken per surface.

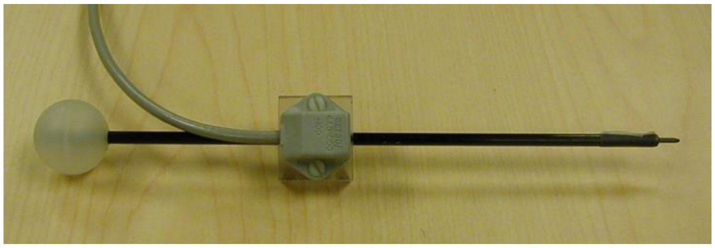

Figure 4.7: Polhemus digitizing stylus.

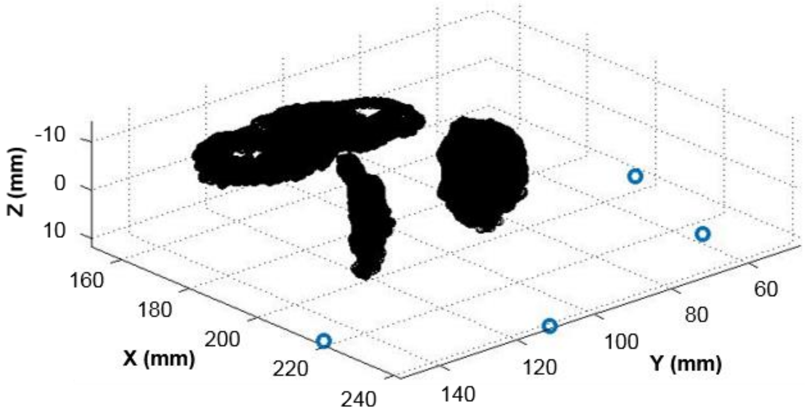

Figure 4.8: Exemplar data set collected during the post-testing digitization procedure of an L4 vertebra from a T12-L4 specimen. The facet and endplate surfaces appear in black, and the four fiducial markers are shown as blue circles. The figure is angled as though the observer were viewing the specimen from its posterolateral left side.

4.3 Data Processing and Analysis

Data processing was completed using custom programs written in MATLAB (The MathWorks Inc., Natick, MA, USA). The kinetic data were downsampled to match the kinematic data at 60 Hz. Synchronization was achieved through the use of a sync light that was triggered when the LabView program began the test. The facet kinematics *at the index level* (L3-L4) were determined via rigid-body, point-based registration in which each specimen's segmental kinematics were applied to its 3D anatomical model via the fiducial markers. This process established a series of mathematical relationships between the reflective marker sets, fiducial markers, and articular surfaces of the facets. The following three subsections describe the procedure in depth.

4.3.1 Step #1: Facet-Based Coordinate System

A coordinate system was developed for each facet based on the geometry of its articular surface [41]. The articular surface of a bone is generally identified by the presence of a thin layer of hyaline cartilage; however, the 3D anatomical model developed for each specimen only delineated its bony surfaces and fiducial markers. Therefore, the articular surface of each facet was defined computationally as the surface within a threshold distance of the opposing facet [73]. The threshold distance was chosen according to two major assumptions:

- Each articular surface was covered by a uniform layer of cartilage. The thickness of the cartilage was chosen to be 1.11 mm for the L3 facets and 1.36 mm for the L4 facets. These were conservative estimates based on Woldtvedt et al.'s [31] measurements of the maximum cartilage thickness in the lumbar facet joints.

- In the neutral position, the thickness of the joint gap was 0.6 mm. This value was within the range of gap thicknesses implemented in previous finite element models of the lumbar spine [31,74]. For the L2-L5 specimens, the neutral position was taken to be the position in which the specimens were CT scanned. Because the T12-L4 specimens were not imaged, the neutral position was alternately defined as the position of the specimen at the start of the first motion test performed in the intact condition.

Based on the sum of the above dimensions, a threshold distance of 3.07 mm was used. The 3D coordinates of each specimen's L3-L4 facet joints were obtained from its anatomical model. [For the L2-L5 specimens, this was done by manually selecting the appropriate vertices on the STL models in Blender (Figure 4.9) and exporting their coordinates. For the T12-L4 specimens, the coordinates were pulled directly from the Polhemus data sets.] The coordinates were run through a custom MATLAB program that identified the articular surfaces based on the 3.07 mm distance criterion (Figure 4.10). The surfaces resulting from the automatic selection routine were visually inspected for plausibility based on general anatomical knowledge and then saved for later use.

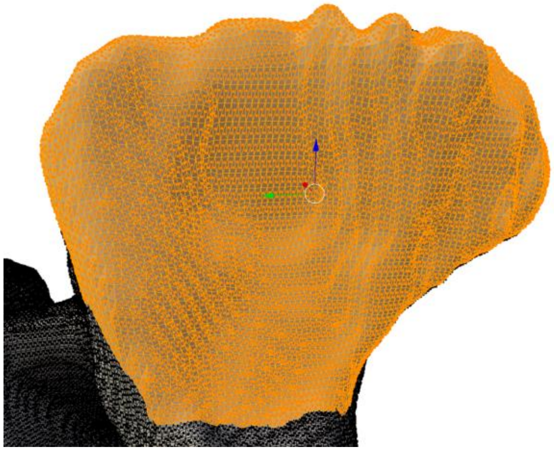

Figure 4.9: Selected vertices on the L4 right facet of an L2-L5 specimen's 3D anatomical model.

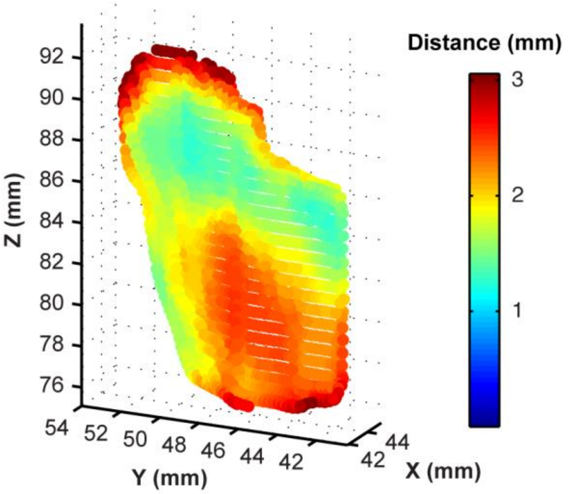

Figure 4.10: Articular surface of a specimen's L3 left facet identified by the automatic selection routine. Each point comprising the surface is colored according to the distance from its nearest neighbor on the opposing facet. The figure is angled as though the observer were viewing the specimen from its left side, looking directly at the surface.

After the articular surfaces had been isolated, a coordinate system was defined for each facet based on the shape of its articular surface. Previous researchers have approximated the lumbar facet surface as a plane, both for the purpose of defining facet-based coordinate systems [41] and quantifying the facets' orientation [42]. For the present study, a similar approach was adopted by mathematically fitting a plane to the set of vertices that formed the articular surface. This was done using a regression technique known as principal components analysis (PCA). When PCA is applied to a trivariate data set, it fits a plane to the data such that (1) the plane passes through the mean data point and (2) the perpendicular distance from each point to the plane is minimized. To illustrate this technique, an articular surface is shown below with its best-fit plane found through PCA (Figure 4.11). Across specimens, the root mean square (RMS) error of the fit was 0.62 ± 0.31 mm for the L3 facets and 0.96 ± 0.29 mm for the L4 facets. Compared to the average dimensions of lumbar facet surfaces [42], the RMS errors were relatively low. This further supported the decision to model each surface as a plane.

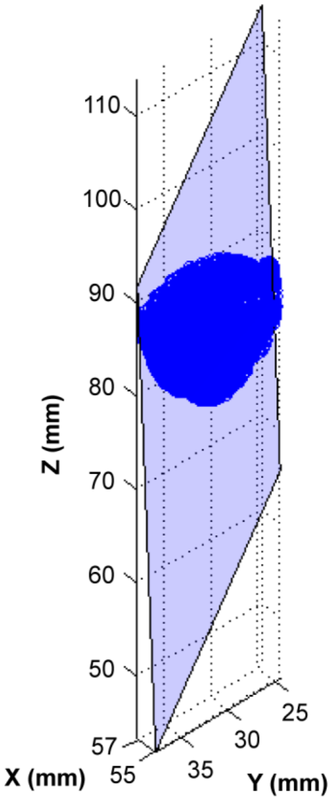

Figure 4.11: Articular surface of a specimen's L3 right facet with its best-fit plane generated through PCA. The surface and best-fit plane are shown as though the observer were standing on the right side of the specimen, looking directly at the surface.

The coordinate system of each facet was developed around the best-fit plane of its articular surface. The origin was placed on the plane, at the center of the surface. The axes of the coordinate system—designated U, V, and W—were formed as follows:

- U-axis: A vector was defined that passed between the centers of the inferior and superior vertebral endplates and pointed superiorly [75]. The vector was projected onto the best-fit plane to create the U-axis (Figure 4.12).
- W-axis: The normal to the best-fit plane was chosen as the W-axis. For the articular surfaces of the *left* facet joint, the W-axis was directed *toward* the L4 facet, whereas the opposite held true for the articular surfaces of the *right* facet joint.
- V-axis: The V-axis was defined as the vector cross-product of the W- and U-axes. It lay within the best-fit plane and was directed anteriorly and medially.

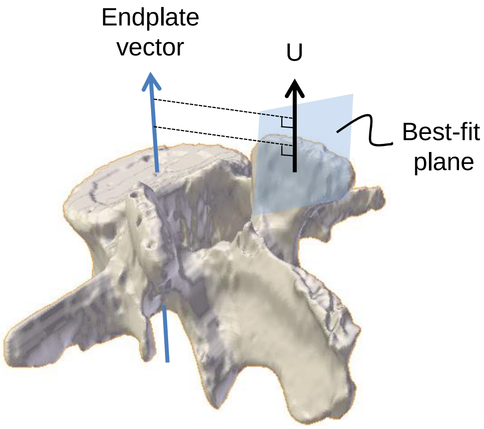

Figure 4.12: A vector was defined that passed through the centers of the vertebral endplates and was directed superiorly. The U-axis was formed by projecting the vector onto the best-fit plane of the facet's articular surface. The figure depicts the process for an L4 right facet.

Adherence to these conventions produced a coordinate system that was intimately linked to the geometry of each facet while still maintaining meaning in global anatomy (Figure 4.13).

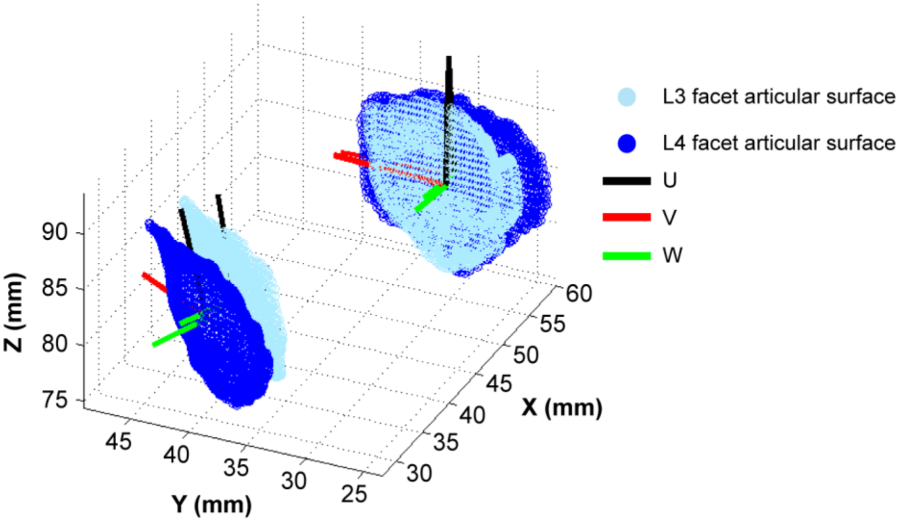

Figure 4.13: Articular surfaces of a specimen's L3-L4 facet joints. Each surface is depicted with the axes of its coordinate system. The figure is shown as though the observer were viewing the specimen from above, standing on its posterolateral left side.

4.3.2 Step #2: Fiducial Marker Motion

The second step in determining the facet kinematics was to compute the motion of the L3 and L4 fiducial markers. The digitization of the fiducial markers identified their locations relative to the reflective marker sets (${}^{MkrSet}FM$). The reflective marker sets were tracked by the Vicon system throughout testing. For each vertebra, a rotation transformation matrix was formed at each time point to describe the position and orientation of its reflective marker set relative to the global (Vicon) reference frame (${}^{Global}_{MkrSet}T_t$). These matrices were used to transform the fiducial marker positions into the global reference frame so that their locations were known throughout the motion tests. Equation 4.1 demonstrates the mathematics for a single fiducial marker at a specific point in time. In the equation, the subscript “t” denotes a variable that was computed at each time point, while a variable without it is a fixed, constant relationship.

$$ {}^{Global}FM_t = \left({}^{Global}_{MkrSet}T_t \right)\left({}^{MkrSet}FM \right) \tag{4.1} $$

4.3.3 Step #3: Facet Kinematics

The final step in computing the facet kinematics was to combine the facet coordinate system information with the motion of the fiducial markers. The equations that appear in this section illustrate the mathematical procedure for both the L3-L4 left and right facet joints. Similar to Equation 4.1 above, variables with the subscript “t” were calculated at each time point of the motion tests.

The process began by defining four rotation transformation matrices: one for each facet comprising the L3-L4 facet joints. Each matrix described the coordinate system of one of the facets (e.g. L3 left facet) relative to a coordinate system developed for the fiducial markers on the corresponding vertebra (e.g. L3) (Equations 4.2a-d). As the right-hand sides of the equations show, all the relevant data were derived from the 3D anatomical models. Because the fiducial marker and facet coordinate systems were developed from geometry acquired from the models, the description (position and orientation) of each coordinate system was a description *relative to* the model’s reference frame (CT or Polhemus).

$$ {}^{L3FM}_{L3Left}T = \left({}^{Model}_{L3FM}T \right)^{-1} \left({}^{Model}_{L3Left}T \right) \tag{4.2a} $$

$$ {}^{L3FM}_{L3Right}T = \left({}^{Model}_{L3FM}T \right)^{-1} \left({}^{Model}_{L3Right}T \right) \tag{4.2b} $$

$$ {}^{L4FM}_{L4Left}T = \left({}^{Model}_{L4FM}T \right)^{-1} \left({}^{Model}_{L4Left}T \right) \tag{4.2c} $$

$$ {}^{L4FM}_{L4Right}T = \left({}^{Model}_{L4FM}T \right)^{-1} \left({}^{Model}_{L4Right}T \right) \tag{4.2d} $$

Once the relationships between the fiducial marker and facet coordinate systems had been established, a motion test could be analyzed. Using the output from Step #2, two rotation transformation matrices were formed at each time point to describe the fiducial marker coordinate systems relative to the global reference frame (${}^{Global}_{L3FM}T_t$ and ${}^{Global}_{L4FM}T_t$). This permitted the four facet coordinate systems to be expressed in the same frame (Equations 4.3a-d).

$$ {}^{Global}_{L3Left}T_t = \left({}^{Global}_{L3FM}T_t \right) \left({}^{L3FM}_{L3Left}T \right) \tag{4.3a} $$

$$ {}^{Global}_{L3Right}T_t = \left({}^{Global}_{L3FM}T_t \right) \left({}^{L3FM}_{L3Right}T \right) \tag{4.3b} $$

$$ {}^{Global}_{L4Left}T_t = \left({}^{Global}_{L4FM}T_t \right) \left({}^{L4FM}_{L4Left}T \right) \tag{4.3c} $$

$$ {}^{Global}_{L4Right}T_t = \left({}^{Global}_{L4FM}T_t \right) \left({}^{L4FM}_{L4Right}T \right) \tag{4.3d} $$

The analysis concluded by synthesizing the results from Equations 4.3a-d. For each side (left and right), a rotation transformation matrix was defined at each time point that described the L3 facet coordinate system relative to the L4 facet coordinate system (Equations 4.4a-b).

$$ {}^{L4Left}_{L3Left}T_t = \left({}^{Global}_{L4Left}T_t \right)^{-1} \left({}^{Global}_{L3Left}T_t \right) \tag{4.4a} $$

$$ {}^{L4Right}_{L3Right}T_t = \left({}^{Global}_{L4Right}T_t \right)^{-1} \left({}^{Global}_{L3Right}T_t \right) \tag{4.4b} $$

From these matrices, the six degree of freedom (DOF) kinematics of the L3 facets were determined. The orientation was described as a set of three Cardan angles in the order U-V-W [76]. The facets' translational and rotational ranges of motion (ROMs) were computed from the kinematic data. The ROM was defined as the total amount of motion (linear or angular) between the loading extremes of a particular motion test.

4.3.4 Validation of Registration Procedure

The previous two subsections illustrate that a rigid-body, point-based registration technique formed the basis for determining the facet kinematics. This procedure involved the alignment of a set of points (fiducial markers) that were localized within two different reference frames. Namely, the locations of each specimen's fiducial markers were measured within the global (Vicon) reference frame during digitization; and they were also identified within the reference frame of the specimen's 3D anatomical model (i.e. CT or Polhemus). As one might expect, an error in either of these localization steps would tend to propagate through the registration process, resulting in inaccuracies in the final, determined kinematics. It was thus important to quantify this error, which was done via a geometrical measure of alignment known as the "fiducial registration error" (FRE) [77,78]. FRE is a common measure of registration accuracy and is defined as the RMS distance between homologous fiducial markers after alignment. For a perfect registration, the FRE would be zero. However, due to inaccuracies in localizing the fiducial markers in either (or both) reference frames, the FRE generally has some non-zero value. In this study, the mean FRE across specimens was 0.15 mm.

4.3.5 Hypothesis H_1 Testing

Hypothesis H_1 was addressed with a linear mixed-effects regression model (Appendix C) that tested for the association between the L3 facets' translational and rotational ROMs (the dependent variable) with testing condition and motion test (the independent fixed effects). Separate models were run for the left and right facets. Hypothesis testing was done with an omnibus test to assess whether the differences in mean motion varied across testing condition. If a significant difference was found, pair-wise comparisons among the three testing conditions were carried out. The significance level was set to $P < 0.05$.

4.4 Results

The following section summarizes the L3 facets' translational and rotational ROMs and their general motion patterns under each loading condition. It also presents the results from the statistical analysis which tested hypothesis H_1. To assist in interpreting the results, Figure 4.14 depicts a representative facet with the axes of its coordinate system. Table 4.1 describes each kinematic DOF in anatomical terms.

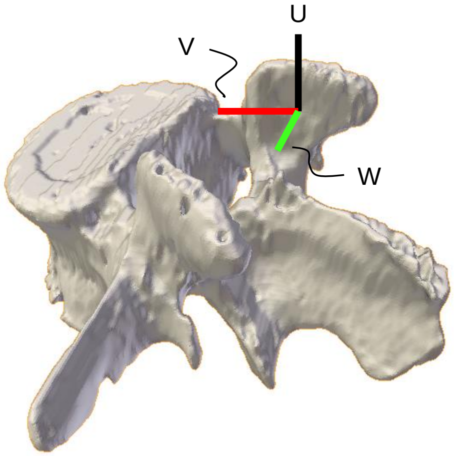

Figure 4.14: L4 right facet with the axes of its coordinate system. The origin was centered on the articular surface. The U- and V- axes lay within the best-fit plane of the articular surface. The U-axis pointed superiorly, and the V-axis was directed anteriorly and medially. The W-axis was the normal to the best-fit plane with an orientation that was consistent with a U-V-W right-handed Cartesian coordinate system.

Table 4.1: Anatomical meaning of the kinematic DOFs.

Type of motion	Direction	Anatomical meaning
Translation	U	L3 facet translates along the surface of the opposing L4 facet in the superoinferior direction
	V	L3 facet translates along the surface of the opposing L4 facet in the anteromedial or posterolateral direction
	W	L3 facet separates or moves toward the opposing L4 facet
Rotation	U	L3 facet "twists" about its long axis
	V	L3 facet "rocks" side-to-side
	W	L3 facet "rolls" across the surface of the opposing L4 facet

4.4.1 Range of Motion

The translational and rotational ROMs of the L3 facets are listed in Tables 4.2 and 4.3, ordered by motion test and testing condition. The data are presented graphically in Appendix B.

Table 4.2: Translational ROM of the L3 facets (n = 9) for the three testing conditions. Values are presented as mean (standard deviation) in millimeters.

	Translational ROM (mm)					
	Left facet			**Right facet**		
	U	*V*	*W*	*U*	*V*	*W*
FE						
Intact	4.7 (1.7)	0.6 (0.5)	0.3 (0.2)	4.9 (1.8)	0.7 (0.6)	0.2 (0.2)
PD	5.5 (2.2)	0.6 (0.5)	0.4 (0.4)	5.5 (2.1)	0.6 (0.8)	0.3 (0.2)
SD	6.1 (2.3)	0.6 (0.6)	0.6 (0.4)	6.1 (2.1)	0.8 (1.0)	0.4 (0.2)
LB						
Intact	2.7 (1.0)	0.6 (0.7)	0.5 (0.5)	2.1 (1.1)	0.7 (0.6)	0.6 (0.4)
PD	2.8 (1.1)	0.7 (0.8)	0.6 (0.8)	2.4 (1.1)	0.8 (0.8)	0.5 (0.4)
SD	2.6 (1.4)	0.8 (0.8)	0.6 (0.9)	3.3 (1.7)	0.9 (0.8)	0.7 (0.5)
AR						
Intact	0.5 (0.5)	0.7 (0.5)	1.6 (1.5)	0.4 (0.4)	0.7 (0.8)	1.3 (0.9)
PD	0.8 (0.6)	0.8 (0.5)	1.9 (1.9)	0.5 (0.4)	0.9 (1.0)	1.5 (0.9)
SD	0.8 (0.6)	0.8 (0.6)	1.9 (1.9)	0.7 (0.5)	1.0 (0.9)	1.7 (1.0)
FRLB						
Intact	5.2 (1.7)	0.7 (0.5)	0.4 (0.3)	1.7 (1.3)	0.7 (0.6)	0.5 (0.3)
PD	6.0 (2.3)	0.9 (0.5)	0.5 (0.3)	2.4 (1.8)	0.8 (0.7)	0.6 (0.4)
SD	6.3 (2.3)	0.8 (0.5)	0.6 (0.3)	2.5 (1.7)	0.7 (0.7)	0.6 (0.3)
FLLB						
Intact	1.2 (1.3)	0.5 (0.6)	0.4 (0.4)	5.0 (1.8)	0.6 (0.4)	0.4 (0.2)
PD	1.7 (1.6)	0.5 (0.5)	0.6 (0.4)	5.5 (2.1)	0.7 (0.5)	0.3 (0.2)
SD	2.3 (1.4)	0.6 (0.6)	0.7 (0.4)	6.6 (2.3)	0.6 (0.6)	0.4 (0.3)

Table 4.3: Rotational ROM of the L3 facets (n = 9) for the three testing conditions. Values are presented as mean (standard deviation) in degrees.

	Rotational ROM (deg)					
	Left facet			**Right facet**		
	U	*V*	*W*	*U*	*V*	*W*
FE						
Intact	0.9 (0.6)	4.6 (2.5)	6.2 (2.4)	0.8 (0.5)	4.6 (1.9)	6.3 (2.8)
PD	1.2 (0.9)	4.8 (2.3)	7.5 (3.3)	0.9 (0.6)	5.5 (2.1)	7.0 (3.5)
SD	1.4 (0.8)	5.6 (2.7)	8.6 (3.3)	0.9 (0.7)	6.4 (2.6)	8.0 (3.4)
LB						
Intact	1.0 (0.5)	7.7 (3.0)	5.6 (2.0)	0.7 (0.5)	7.4 (3.5)	5.4 (2.8)
PD	1.0 (0.5)	8.3 (3.5)	5.9 (2.2)	0.7 (0.4)	8.0 (4.1)	5.8 (2.9)
SD	1.0 (0.6)	9.5 (4.1)	6.4 (2.7)	0.7 (0.6)	8.9 (4.5)	6.8 (3.3)
AR						
Intact	4.6 (2.5)	1.5 (1.1)	1.3 (0.8)	4.7 (2.6)	1.2 (1.1)	1.0 (0.8)
PD	5.2 (2.7)	1.5 (1.1)	1.5 (0.9)	5.3 (2.8)	1.2 (1.2)	1.4 (0.7)
SD	5.7 (2.9)	1.7 (1.2)	1.7 (1.0)	5.9 (3.0)	1.3 (1.3)	1.5 (0.8)
FRLB						
Intact	1.0 (0.7)	2.5 (2.6)	8.4 (2.6)	0.8 (0.6)	8.7 (2.5)	2.6 (1.6)
PD	1.0 (0.8)	2.4 (2.6)	9.5 (3.2)	0.8 (0.8)	9.5 (2.9)	2.7 (2.5)
SD	1.1 (0.7)	3.0 (3.1)	10.7 (3.4)	1.1 (0.9)	10.8 (3.1)	2.6 (2.9)
FLLB						
Intact	1.0 (0.6)	8.8 (3.0)	1.9 (1.4)	0.7 (0.5)	3.0 (2.7)	8.4 (2.5)
PD	1.2 (0.9)	9.4 (3.4)	2.0 (2.2)	0.6 (0.4)	2.7 (2.7)	9.3 (2.9)
SD	1.4 (1.0)	10.8 (3.6)	1.9 (2.1)	0.6 (0.3)	3.4 (3.2)	10.5 (3.0)

4.4.2 General Patterns of Facet Motion

Though interspecimen variability resulted in a unique kinematic signature for each specimen, the observed variations were primarily in the *magnitude* of motion. For each motion test, the primary (and secondary) directions of motion were largely consistent across specimens. The general motion patterns under each loading condition are described below.

Flexion-Extension

In FE, the left and right facets exhibited symmetrical motion. The majority of translation occurred in the superoinferior direction, along the U-axis. Regardless of testing condition, the total amount of translation in the V-direction was always around 0.6-0.7 mm, whereas translation in the W-direction never exceeded that amount. The primary direction of rotation was about the W-axis (the normal to the articular surface). This motion corresponded to the L3 facet “rolling” across the surface of the opposing L4 facet.

Lateral Bending

Similar to FE, the facets mainly translated in the superoinferior direction during LB. However, unlike FE, the translation in this direction was asymmetric, and more motion occurred on the contralateral side. Translations in the V- and W-directions were consistently around 0.6-0.7 mm for every testing condition. The facets mainly rotated around the V-axis, consistent with a “tilting” motion that was directed side-to-side. The secondary direction of rotation was about the W-axis, representative of the physiological coupling between LB and AR.

Axial Rotation

The facets displayed limited motion in AR. It was the only test in which the dominant mode of translation was in the out-of-plane direction (along the W-axis). During counterclockwise AR, the left facet tended to shift posteriorly (in the –V direction) while the right facet shifted anteriorly (in the +V direction); and the opposite trend occurred during clockwise AR. Both facets experienced a slight superior translation regardless of the direction of applied rotation. The majority of rotation occurred about the U-axis, corresponding to the facets “spinning” about their long axis. Rotations about the V- and W-directions were minor (< 2 deg) and inconsistent between specimens.

Combined Loading

In the combined FE with LB tests, the left and right facets demonstrated asymmetrical motion. For the FRLB test, flexion was applied with right LB followed by extension with left LB. During this test, the left facet experienced much larger translations than the right facet. Its response was reminiscent of the motion patterns seen during pure FE, with the majority of translation occurring in the superoinferior direction. The right facet also translated along the U-axis, though it displayed less than half the amount of translation that the left facet did. With regard to angular motion, the primary direction of rotation was different between the two facets. Similar to the FE test, the left facet mainly rotated about the W-axis. In contrast, the right facet mainly rotated about the V-axis. The motion patterns observed during the FLLB test were the exact opposite to what was seen during the FRLB test. Taken together, these results suggest that during a combined FE with LB test, one facet is dominated by the FE movement while the other facet is dominated by the LB movement.

4.4.3 Hypothesis H_1

Omnibus hypothesis testing revealed differences in three ROMs by testing condition: translation along the U-axis (T_U) and rotations about the V- and W-axes (R_V and R_W) (Table 4.4). There was no significant association between testing condition and motion for the remaining three ROMs (translations along the V- and W-axes and rotation about the U-axis).

Table 4.4: Significant P-values ($P < 0.05$) from the omnibus tests. For each ROM, these tests assessed whether the differences in mean motion varied across testing conditions.

ROM	**P-value**	
	Left facet	*Right facet*
T_U	0.0033	< 0.0001
R_V	0.034	0.0090
R_W	0.0098	0.031

Pairwise comparisons among the three testing conditions were conducted for ROMs T_U, R_V, and R_W. The results are given in Tables 4.5-4.7.

Table 4.5: Pairwise comparisons among the three testing conditions for the L3 facets' translational ROM along the U-axis (T_U). Mean differences and standard errors are given in millimeters. P-values are listed only for statistically significant comparisons ($P < 0.05$).

Comparison		**Left facet**			**Right facet**		
I	*J*	*Mean difference (J-I)*	*Standard error*	*P-value*	*Mean difference (J-I)*	*Standard error*	*P-value*
Intact	PD	0.48	0.23		0.43	0.22	
Intact	SD	0.77	0.23	< 0.05	0.97	0.22	< 0.001
PD	SD	0.30	0.23		0.54	0.22	< 0.05

Table 4.6: Pairwise comparisons among the three testing conditions for the L3 facets' rotational ROM about the V-axis (R_V). Mean differences and standard errors are given in degrees. P-values are listed only for statistically significant comparisons ($P < 0.05$).

Comparison		**Left facet**			**Right facet**		
I	*J*	*Mean difference (J-I)*	*Standard error*	*P-value*	*Mean difference (J-I)*	*Standard error*	*P-value*
Intact	PD	0.28	0.44		0.41	0.40	
Intact	SD	1.11	0.44	< 0.05	1.24	0.40	< 0.05
PD	SD	0.83	0.44		0.83	0.40	

Table 4.7: Pairwise comparisons among the three testing conditions for the L3 facets' rotational ROM about the W-axis (R_W). Mean differences and standard errors are given in degrees. P-values are listed only for statistically significant comparisons ($P < 0.05$).

Comparison		**Left facet**			**Right facet**		
I	*J*	*Mean difference (J-I)*	*Standard error*	*P-value*	*Mean difference (J-I)*	*Standard error*	*P-value*
Intact	PD	0.61	0.39		0.49	0.42	
Intact	SD	1.20	0.39	< 0.05	1.13	0.42	< 0.05
PD	SD	0.60	0.39		0.63	0.42	

4.5 Discussion

This section summarizes the key findings and compares them with the results from previous investigations that have either looked at lumbar facet kinematics or the effects of disc removal on lumbar spinal motion. The section concludes with a discussion of the study's limitations.

4.5.1 Facet Kinematics

This study was designed to measure potential changes in lumbar facet motion concomitant with two surgical procedures performed at the disc; but at its most basic level, its purpose was to measure the relative 3D motion of two rigid bodies. To compute the 3D kinematics of an object, a 3D coordinate system must be assigned to it. The placement and orientation of the coordinate system are critical to our understanding of the object's motion. For example, in the first published study on human lumbar facet kinematics, Kozanek et al. [40] developed a facet coordinate system with axes that were aligned with the anatomical directions of the body. While it is easy to visualize such a reference frame, it does not lend itself to a straightforward interpretation of facet motion since the articular surfaces of the facets are not oriented with any of the anatomical planes. Furthermore, it makes comparisons difficult because the orientation of the facets changes along the length of the spine; and even at a specific level, there can be large differences in facet inclination between individuals. For these reasons, this study employed a coordinate system that was based on the geometry of the facet's articular surface [41]. By design, this coordinate system gives explicit information on facet articulation and separation and thus provides a more intuitive description of the joint's motion.

Kozanek et al. [40] and Jegapragasan et al. [41] are the only two groups that have quantitatively measured human lumbar facet kinematics. Both studies were done with intact, non-pathological spines. Similar to this investigation, the researchers found that the L3-L4 facets were most mobile under sagittal plane loading. This kinematic behavior may be partially explained by the orientation of the facets. Facet orientation changes along the length of the spine, but in general, the facets of the upper lumbar levels are oriented closer to the midsagittal plane than those of the lower levels [28]. This orientation favors sagittal plane movements, and the results of this study reflected this. Across testing conditions, the facets were most mobile during tests that incorporated FE (i.e. either pure FE or the combined FE with LB tests).

In terms of the measurements themselves, a direct comparison was made with the results of Jegapragasan et al. [41], who also utilized a facet-based coordinate system that was aligned with the articular surface. Their findings compared favorably with the data from this study taken in the intact condition. Similarities were noted in both the overall motion patterns and the translational ROMs. In FE and LB, the researchers noted that the facets moved almost entirely in the superoinferior direction along the surface of the opposing facet, while in AR, the largest translations occurred in the out-of-plane direction. Table 4.8 compares the measured translational ROMs between Jegapragasan et al. [41] and the current study (in the intact condition) for the primary direction of motion. Though Jegapragrasan et al. [41] tested multiple spinal levels, the table only includes their results from the L3 facets.

Table 4.8: Comparison of the L3 facets' translational ROMs from Jegapragasan et al. [41] and the present study (in the intact condition). Values are presented as mean (standard deviation) in millimeters.

Motion test	**Direction of motion**	**Translational ROM (mm)**			
		Jegapragasan et al. [41]*		**Current study**	
		Left facet	*Right facet*	*Left facet*	*Right facet*
FE	U	4.9 (0.5)	5.4 (0.6)	4.7 (1.7)	4.9 (1.8)
LB	U	3.1 (0.4)	2.5 (0.1)	2.7 (1.0)	2.1 (1.1)
AR	W	1.6 (0.2)	1.5 (0.1)	1.6 (1.5)	1.3 (0.9)

*Values were estimated from graphs using ImageJ (National Institutes of Health, Bethesda, MD, USA.

As shown in Table 4.8, the translational ROMs in the present study were similar in magnitude to those reported by Jegapragasan et al. [41] even though the two studies loaded their specimens to different maximum moments (±10 Nm versus ±7.5 Nm, respectively). This is likely due to the sigmoidal relationship between intervertebral joint angle and joint moment: at higher load levels, there is a minimal increase in motion with increasing load. Unfortunately, Jegapragasan et al. [41] did not report the facets' rotational ROMs, nor did they examine any forms of combined loading. Nevertheless, the similarities between their study and the present one were promising and helped validate the developed methodology.

4.5.2 Kinematic Response to Microdiscectomy

With regard to the kinematic response to microdiscectomy, there have been a few published studies examining the effects of disc removal on the kinematics of the lumbar spine. None have looked specifically at the response of the facets, instead focusing on the motion of the intervertebral joint as a whole. Panjabi et al. [20] undertook an *in vitro* investigation to see whether disturbances to the two components of the disc altered the 3D kinematics of lumbar motion segments under bending and shear. The authors found that disc injury increased both the main and coupled motions. In general, changes due to nucleus removal were greater than changes due to annular injury alone. Though the study showed a mechanical response to disc injury, it received some criticism for inducing injuries that may have been clinically unrealistic [79]. Disc herniations typically occur on the posterolateral side within the vertebral canal, and discectomies are performed at the lesion. However, Panjabi et al. [20] created annular injuries outside the vertebral canal, lateral to the neural foramen, leaving the question of whether their results were location-dependent. In a later study, Goel et al. [79] looked at the effects of PD when performed at the most common site of disc herniation (within the vertebral canal close to the midsagittal plane). The authors performed a statistical analysis on their data (Panjabi et al. [20] did not). PD was shown to produce significant increases in primary motion during flexion, LB, and AR. Unlike the study by Panjabi et al. [20], there was not an increase in coupled motions.

There were two main similarities between the findings of this research and those of the aforementioned studies. First, both Panjabi et al. [20] and Goel et al. [79] found a correlation between the extent of disc excision and intervertebral joint motion. While this investigation was exclusively concerned with the kinematics of the facets, a relationship between disc excision and motion was also observed. The second major similarity was that—like Goel et al. [79] noted—the largest increases in ROM occurred along the primary directions of motion. For every motion test aside from AR, the facets' kinematics were predominantly characterized by translations along the

U-axis and rotations about either the V- or W-axis (or both). Accordingly, these were the same ROMs that exhibited significant differences between testing conditions (Table 4.4).

For both the left and right facets, the pairwise comparisons (for T_U, R_V, and R_W) revealed significant differences between the intact and SD conditions. The results pertaining to the PD condition were less conclusive: with one exception, there was no evidence that the motion observed after PD differed from what was seen in the intact *or* SD conditions. This finding was contradictory to what was reported by Goel et al. [79] and may have been due to the limited sample size of this study—a point which is discussed further in Section 4.5.3. Alternatively, it could have been the result of methodological differences. For example, Goel et al. [79] did not conduct their statistical analysis on the raw data but on the percent increase in ROM from intact. Though normalization facilitates comparison between specimens, it also runs the risk of inflating results which might not be clinically significant—particularly in cases where the baseline ROM is small. Additionally, the authors measured the motion of the entire intervertebral joint which prevented them from identifying where the observed kinematic changes occurred. So while the *total* motion of the joint was significantly larger after PD, it is possible that the increase in motion was primarily localized at the disc.

Finally, though both facets demonstrated a kinematic response to disc injury, there was some evidence of an underlying asymmetry between them. After SD, the right facet's translational ROM in the U-direction was significantly greater than what was seen in both the intact *and* PD conditions ($P < 0.001$ and $P < 0.05$, respectively). This was the only significant difference measured between the PD and SD conditions in the pairwise comparisons (for T_U, R_V, and R_W); and notably, the comparison between the intact and SD conditions yielded the smallest P-value of the entire analysis. These results appeared to be driven by the motion tests involving LB. In pure LB, the left facet's total translation along the U-axis was relatively consistent between the intact and SD conditions (2.7 ± 1.0 mm versus 2.6 ± 1.4 mm, respectively), whereas the right facet exhibited a nearly 60% increase in motion (2.1 ± 1.1 mm versus 3.3 ± 1.7 mm, respectively). A similar side discrepancy was observed in the combined FE with LB tests. These findings suggest that SD may differentially alter the kinematics of the facets, leading to more pronounced aberrations in the movement of the contralateral facet. In the study by Panjabi et al. [20], disc excision was shown to produce asymmetries in the segmental motion response to mirror image loads. The authors hypothesized that it was due to asymmetric motion of the facets, and the results of this study may confirm this.

4.5.3 Limitations

As with any research study, this investigation had several limitations. First, it was an *in vitro* study and therefore did not account for the presence of body weight or muscle activation. *In vivo*, it is possible that the trunk muscles may adapt their activity to modulate the effects of increased or asymmetric motion of the facets. Second, the specimens were tested right after disc excision, so the observed behavior was only representative of the immediate postoperative period. Therefore, the results may not have reflected the true extent of kinematic alteration, since instabilities associated with disc injury could take months—if not years—to manifest [80]. And third, the destructive nature of the surgical procedures prevented the order of the testing conditions from being randomized for each specimen.

Outside of these issues—which were all inherent to the chosen experimental model and study design—perhaps the biggest limitation was the sample size (n = 9). It was similar to those of the other spinal biomechanics studies discussed in this chapter [20,40,41,79], and it did allow for some statistically significant differences to be identified. Nevertheless, the statistical analysis was unable to detect some of the subtler nuances in the data set, which was likely the result of the limited sample size combined with a high level of interspecimen variability. For example, among the ROMs that exhibited significant differences between testing conditions (T_U, R_V, and R_W), there was no evidence that the *pattern* of differences between testing conditions varied between motion tests. This was surprising given that there were some tests (e.g. AR) in which the facets displayed very little motion in these three directions regardless of testing condition. A larger sample size could be helpful with finding these differences. Additionally, it would have the potential to "strengthen" the differences between testing conditions. This could be useful for drawing firmer comparisons between PD and the other two testing conditions.

Lastly, it is worth addressing the accuracy of the reported measurements. This study used a rigid-body, point-based registration technique to determine the facet kinematics. The accuracy of the registration procedure was 0.15 mm, as measured by the FRE. As a whole, the specimens' mean translations were greater than this value for every motion test and testing condition under consideration. On an individual basis, however, there were a handful of cases in which a specimen exhibited less than 0.15 mm of translation in a specific direction. In these situations, it was questionable whether the observed translation was real or simply noise in the system. That being said, these cases represented a small percentage of the data set, and throughout the study, every specimen's *total* translation was always greater than the FRE. Furthermore, the accuracy of this system is comparable to that reported by other researchers [37,40]. Thus, the developed methods are likely accurate enough to describe the facets' kinematics.

4.6 Conclusion

Study #1 looked at the effects of two increasingly invasive microdiscectomy procedures on the 3D kinematics of the lumbar facets. The general motion patterns were comparable to the results from previous studies [40,41]. PD and SD produced increases in the left and right facets' translational and rotational ROMs. The largest increases were seen in the three primary directions of motion (T_U, R_V, and R_W). For these specific ROMs, a statistical analysis found significant differences between the intact and SD conditions on both sides. There was some evidence of an underlying asymmetry in the facets' kinematic response to SD, with the contralateral facet being affected more. The asymmetry was most evident in the motion tests that involved LB.

Chapter 5. Digital Image Correlation

5.1 Introduction

Digital image correlation (DIC) is an optical technique for measuring full-field surface deformation and strain. The method was developed in the early 1980s at the University of South Carolina [81] and extended to three-dimensional (3D) measurements during the following decade. Because of its non-contact nature and ease of scalability, the technique is well-suited to measuring the strains of biological tissues. Previous musculoskeletal biomechanics studies have used DIC to explore bone [82–87], cartilage [88–90], ligaments [70,91], tendons [92], and muscle [93]. This chapter is devoted to (1) introducing the fundamentals of DIC and (2) describing the design and validation of a custom 3D-DIC system for measuring the capsular ligament strains in Study #2.

5.2 Background

5.2.1 Calibration

3D-DIC relies on two cameras that are calibrated as a unit (stereo-rig) to take measurements in three dimensions. Calibration is performed via a bundle adjustment technique [94,95] in which the user collects a series of images of a translated and rotated planar grid pattern (Figure 5.1). The images are processed with a Levenberg-Marquardt routine that minimizes the difference between the measured and predicted image coordinates [95]. The output of the routine is a set of intrinsic and extrinsic calibration parameters (Table 5.1). These parameters provide a basis for converting the two-dimensional (2D) image coordinates of each camera into a common 3D position, in a process known as triangulation.

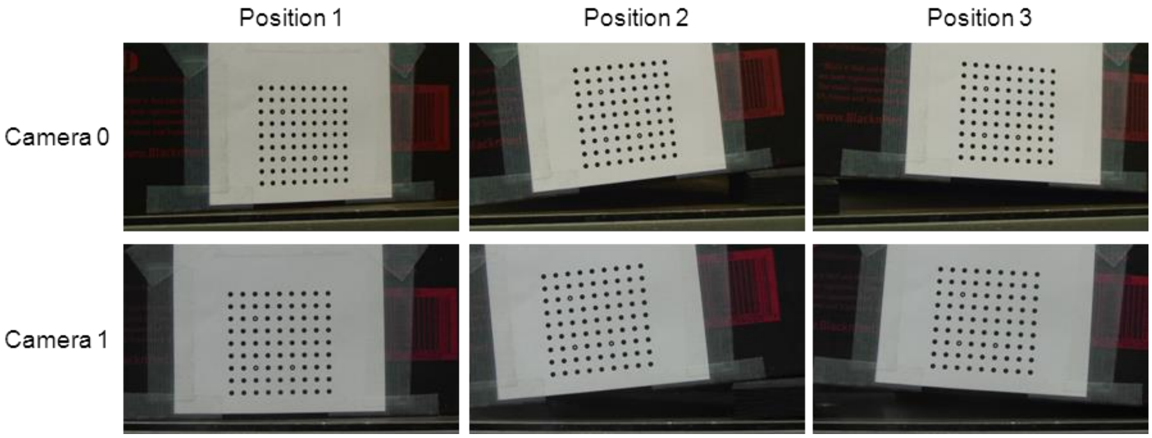

Figure 5.1: The calibration object consisted of a 9 x 9 grid of black circles on a white background. Three of the circles contained a white subcircle to differentiate them from the other circles in the grid. The circles were spaced 5 mm apart. The grid is shown in three different poses for each of the two cameras, which were referred to as Cameras 0 and 1.

Table 5.1: Intrinsic and extrinsic calibration parameters. The intrinsic parameters are determined for each camera. The extrinsic parameters are determined for the stereo-rig as a whole.

Intrinsic parameters	
f_x, f_y	Horizontal and vertical focal lengths
c_x, c_y	Location of image plane center
f_s	Image skew angle
κ_1, κ_2, κ_3	Coefficients of radial lens distortion
Extrinsic parameters	
T_x, T_y, T_z	Position of Camera 1's origin relative to Camera 0's origin
R_x, R_y, R_z	Orientation of Camera 1 relative to Camera 0

5.2.2 Data Collection and Analysis

To measure the deformation of an object with DIC, it is necessary for its surface to be randomly patterned. Though sometimes the object's natural surface texture is distinct enough for analysis, it is more common for a speckle pattern to be manually applied before testing. During deformation, images of the patterned specimen are acquired simultaneously by two cameras that have been calibrated as a stereo-rig. These images, as well as the predetermined calibration parameters, are the inputs to the DIC software.

Image matching lies at the core of the DIC method. To initiate the process, one of the two cameras is arbitrarily selected to be the “master” camera (Camera 0). The master camera’s first collected image of the specimen (in its undeformed shape) then becomes the “reference” image. All subsequent matching routines are performed against this image. Matching is done between (1) the reference image and deformed images from Camera 0 as well as (2) the reference image and all images collected with the other camera (Camera 1). In each case, the matching process begins by breaking the reference image into a series of square subsets of user-defined size. Each subset is then located in the opposing image by minimizing a function that includes the pixel intensity information from both images. There are a number of correlation functions which can be used, each one differing in its robustness and computational efficiency. The function chosen for this study was the zero-mean normalized sum of squared difference (ZNSSD) criterion, which is able to account for localized differences in brightness and contrast between images. This is important because even under ideal experimental conditions, images differ in their intensity because of changes in lighting, specimen orientation, and specimen reflectivity due to strain. It is thus essential to use a matching algorithm that can accurately measure the correspondence between subsets even if there are significant differences in their intensity values [95].

With regard to subset matching, there are two other notable points. First, for specimens undergoing complex deformations, the square subsets originally defined in the reference image will not be square in the corresponding image. The matching algorithm therefore incorporates a shape function to account for both the change in position and configuration of the subset. The standard approach is to use polynomial shape functions. This family includes zero-order (pure translation) and first-order (translation, rotation, normal strains, and shear) polynomials but can be extended to higher orders at the expense of computational time. Studies have shown that for a given subset size, second-order shape functions are better than first-order ones at representing a generic displacement field [95,96]. Thus, a quadratic shape function was selected for this study.

The second important point concerns interpolation. Image matching is generally performed using square subsets in the reference image. But in the opposing image, the subsets may be located at non-integer pixel locations. To accurately estimate the locations of these subsets, the matching algorithm interpolates the intensity pattern of the deformed or cross-camera image. Interpolation is what gives DIC its real power, as it allows the software to provide results that are sub-pixel. The ability to resolve displacements as small as 1/100th of a pixel permits high-resolution displacement measurements, even when the field of view is large. For example, assuming a displacement resolution of 1/30th of a pixel, a 5 megapixel camera looking at a 100 mm specimen would have a displacement resolution of approximately 1.5 µm [97].

Though interpolation has many advantages, it does come at a price, since all interpolants introduce bias to the results. The bias manifests in two forms. The first, called interpolation bias, is seen at the sub-pixel level as a sinusoidal-shaped error in the solution, with the smallest errors occurring at the integer and half-integer pixel locations. The second, called noise bias, is a linear error that results from pixel-level image noise. Both bias sources can be suppressed with higher-order interpolants, but these functions are more computationally expensive. The cubic B-spline is often cited as providing the best balance between quality and efficiency [95] and was thus the chosen interpolant for this study.

Figure 5.2 presents a schematic view of the 3D-DIC process, which is summarized in the steps below. The two cameras are referred to as Cameras 0 and 1, with Camera 0 functioning as the master camera.

1. A subset (x_0, y_0) is chosen in the reference image of Camera 0. Cross-camera correlation is performed with the undeformed image of Camera 1, resulting in a displacement vector (q, r) and matching subset position (x_0+q, y_0+r). This process is repeated for all the remaining subsets in the reference image of Camera 0. The set of corresponding points is reconstructed into the 3D coordinates (X, Y, Z) of the initial specimen shape using the predetermined calibration parameters.
2. The same set of subsets in the reference image of Camera 0 is used in a correlation routine with the deformed image of Camera 0 to locate their matching positions (x_0+u_0, y_0+v_0).
3. The same set of subsets in the reference image of Camera 0 is used in a cross-camera correlation routine with the deformed image of Camera 1 to locate their matching positions (x_0+u_1, y_0+v_1).
4. The set of corresponding points from steps 2 and 3 is reconstructed into the 3D coordinates (X', Y', Z') of the deformed specimen shape using the predetermined calibration parameters.
5. The 3D displacement field (U, V, W) for the specific loading step is computed by subtracting (X', Y', Z') from (X, Y, Z).

The DIC analysis then proceeds by repeating steps 2-5 for each subsequent set of deformed images.

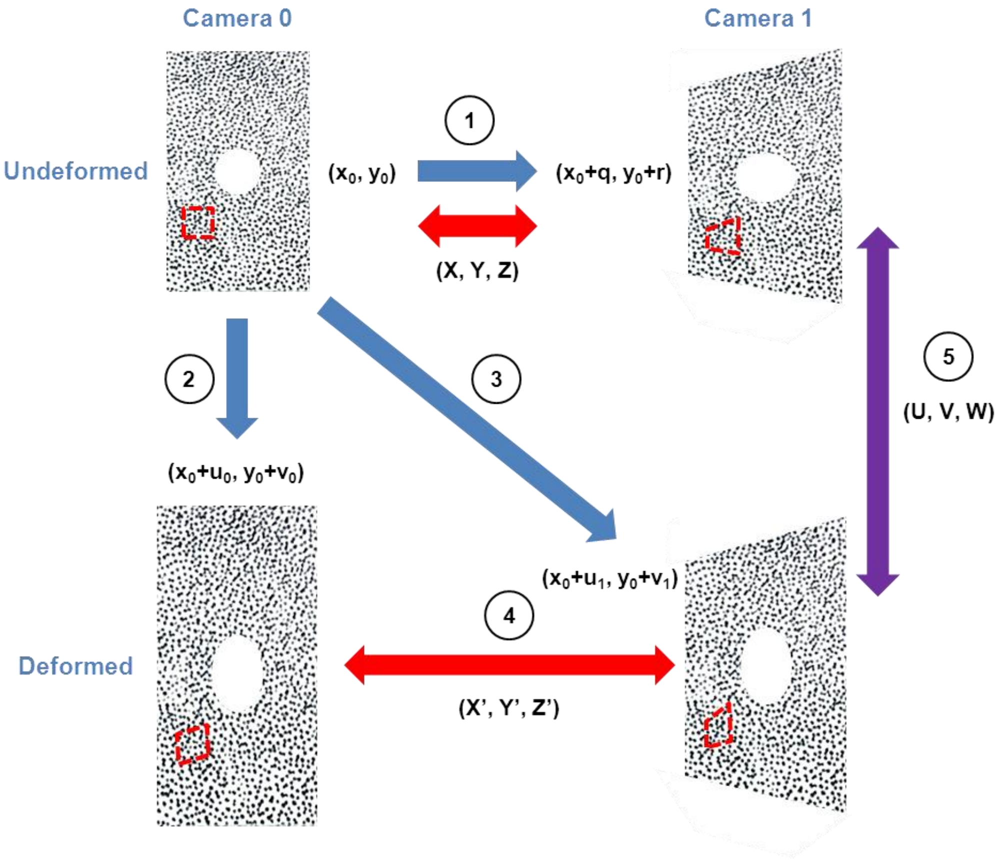

Figure 5.2: 3D-DIC process. The step numbers are circled, and the colors of the arrows correspond to the component of the analysis (blue = image matching, red = triangulation, and purple = post-processing). The sample subset is demarcated with a red dashed line. (Adapted from Lava et al. [98].)

5.2.3 Post-Processing

The 3D displacement fields output by the DIC software contain all the necessary information to compute the in-plane normal and shear strain components (ε_{xx}, ε_{yy}, and ε_{xy}). This involves the determination of the deformation gradient tensor **F**. This second-order tensor is the fundamental measure of deformation in continuum mechanics and maps infinitesimal line elements from the initial (undeformed) configuration into the current (deformed) configuration. It can be expressed in terms of the three displacement fields (u, v, and w) (Equation 5.1).

$$\mathbf{F} = \begin{bmatrix} 1+\frac{\partial u}{\partial x} & \frac{\partial u}{\partial y} & \frac{\partial u}{\partial z} \\ \frac{\partial v}{\partial x} & 1+\frac{\partial v}{\partial y} & \frac{\partial v}{\partial z} \\ \frac{\partial w}{\partial x} & \frac{\partial w}{\partial y} & 1+\frac{\partial w}{\partial z} \end{bmatrix} \tag{5.1}$$

Computation of the Euler-Almansi strain tensor follows naturally (Equation 5.2).

$$\varepsilon^{\ln EA} = \ln\left(\sqrt{\mathbf{F}\mathbf{F}^{\mathbf{T}}}\right) \tag{5.2}$$

5.3 Validation Testing

To measure capsular ligament strains, a 3D-DIC system was built using (1) two off-the-shelf high definition (HD) camcorders and (2) image correlation software (MatchID) developed at The Catholic University College Ghent (Ghent, Belgium). Though the software has been previously validated against commercial systems and finite element models [99], the background presented above suggests that there are many factors (both independent and interrelated) that affect the accuracy of a given DIC system. These include: the camera and lens selection, the configuration of the stereo-rig, the quality of the applied speckle pattern, and the software settings (e.g. correlation function, shape function, interpolation order, and subset size). Thus, a series of validation tests was performed to determine the optimal set-up with the chosen system components.

The validation studies had the following objectives:

- Validation Study #1: Test the ability of the system to recreate the geometry of a specimen.
- Validation Study #2: Examine the system’s capability for measuring rigid body displacements.
- Validation Study #3: Determine how well the system can measure deformation and strain.
- Validation Study #4: Assess the system’s dimensional accuracy under dynamic testing conditions.

5.3.1 Testing Equipment

Camcorders

Two digital HD camcorders were selected for the validation studies. The first was a Sony HDR-SR7 camera (Sony Electronics Inc., San Diego, CA, USA), and the second was a Panasonic HDC-SDT750PP camera (Panasonic Co., Secaucus, NJ, USA). During the tests, the cameras were mounted on individual tripods and operated via remote control to ensure that their relative positions remained unchanged during calibration and testing. The cameras were separated by a mean pan angle of 23 deg to maximize in-plane sensitivity and reduce the matching bias associated with larger pan angles [95]. The specimen of interest was then placed approximately 0.3 m from each camera lens and oriented such that its surface normal nominally bisected the pan angle (Figure 5.3). Finally, each camera's focal length was adjusted via the optical zoom controls so the specimen would remain in focus throughout the test.

Both cameras recorded HD video with a resolution of 1920 pixels x 1080 pixels (w x l). The size of the cameras' field of view varied slightly between tests, but generally, it measured around 160 mm x 90 mm (w x l). This corresponded to a *base* camera resolution of 0.083 mm/pixel. However, as noted in Section 5.2.2, due to interpolation, DIC has the ability to supply results that are sub-pixel. For a typical stereo-rig, one can reasonably expect a displacement resolution between 1/100th and 1/20th of a pixel [100]. If one were to assume a value on the lower end of this range (1/20th of a pixel), that would translate to an *actual* camera resolution of 0.004 mm/pixel.

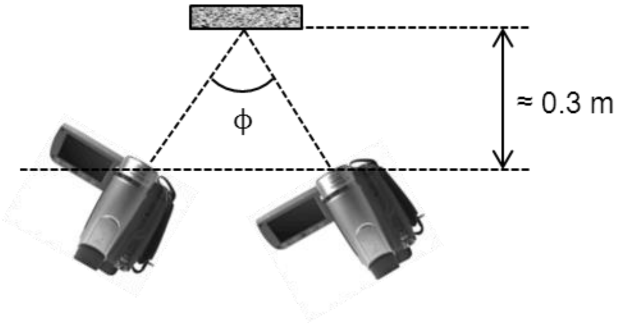

Figure 5.3: Basic set-up of a 3D-DIC test. The cameras were separated by a mean pan angle (φ) of 23 deg, and the specimen was positioned approximately 0.3 m from each camera lens.

Linear Translation Stage

Validation Studies #2 and 3 involved the use of a custom-made linear translation stage (Figure 5.4). The stage consisted of a platform that moved along two rails attached to an L-shaped base. The platform was manually driven along the rails with a screw. During testing, the base was bolted to a plate that lay parallel to the floor. As a result, turning the screw produced a vertical movement of the platform. The position of the platform was measured with a linear variable differential transducer (LVDT) (Model 500 DC-D, Measurement Specialties, Hampton, VA, USA). The hollow tube in the LVDT assemblage was secured to the platform with its long axis aligned with the direction of motion. The LVDT's sliding core was fixed to the base.

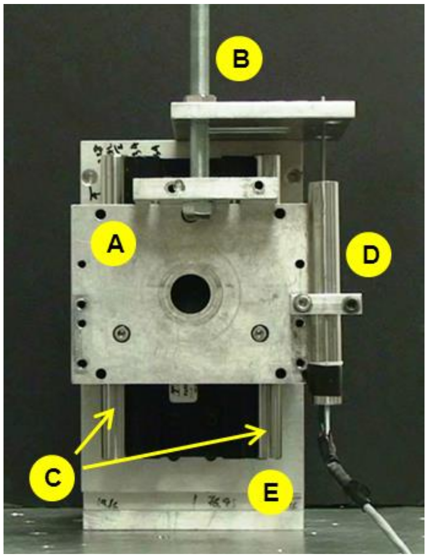

Figure 5.4: Custom-made linear translation stage. The highlighted components are: (A) the platform, (B) the driving screw, (C) the rails along which the platform moved, (D) the LVDT, and (E) the base.

Specimens

Each validation study used a different specimen that was conducive to meeting the specific goals of the test. Though the specimens differed in their materials and geometries, they all shared a common speckle pattern. The patterning was created with a black, ultra-fine point Sharpie marker (Newell Rubbermaid Office Products, Oak Brook, IL, USA). The mean speckle density was measured with ImageJ (National Institutes of Health, Bethesda, MD, USA) and found to be approximately 75 speckles/100 mm^2.

5.3.2 Validation Study #1: Static Dimensional Accuracy

Methods

The purpose of the first validation study was to determine whether the 3D-DIC system could accurately recreate the geometry of a non-planar specimen. This ability was tested by using the system to determine the static profile of a cylinder. The chosen cylinder was a dark color which precluded directly applying a pattern to its outer surface. Therefore, a strip of patterned white paper was tightly wrapped around it and secured at both ends with tape (Figure 5.5). The cylinder was placed within the cameras' field of view, and images of the specimen were captured in four distinct positions. The DIC analysis was run with a subset size of 35 pixels x 35 pixels. The ZNSSD criterion was chosen as the matching algorithm, with a quadratic shape function and cubic B-spline interpolation.

Figure 5.5: The specimen was a solid cylinder wrapped with a patterned piece of white paper.

The resulting 3D point clouds represented the portion of the cylindrical surface that fell within the system's depth of field. The diameter of the cylinder was calculated at twenty equally-spaced intervals along the length of the surface [101] and averaged to obtain the value for that collection. The results were compared with measurements of the cylinder's diameter taken with a handheld digital caliper (Model CD-8 BS, Mitutoya America Corp., Aurora, IL, USA).

Results

Figure 5.6 shows a representative point cloud of the cylindrical surface from one of the image collections. The mean diameter over the four trials was 51.19 ± 0.24 mm. The diameter measured with the handheld digital caliper was 51.12 ± 0.10 mm, representing the average of four measurements taken by the same observer. Compared with this value, the DIC analysis produced a percent error of 0.14%.

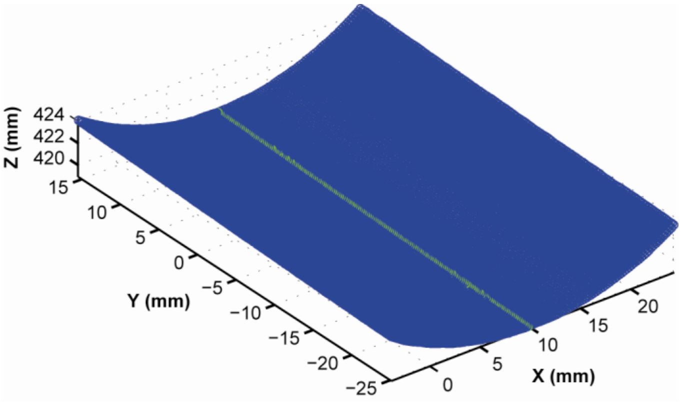

Figure 5.6: Portion of the cylindrical surface that was recreated by the DIC analysis. The green line extends in the direction of the surface's length.

5.3.3 Validation Study #2: Rigid Body Motion

Methods

The second validation study was done to see if the 3D-DIC system could accurately measure rigid body displacements. The specimen for the study was a flat rectangle of cardboard that was rigidly attached to the platform of the translation stage. Before testing began, the platform was put in its starting position (Position 1) with the specimen in the approximate center of each camera's field of view. Images of the specimen were then collected with both cameras. The Sony camera was arbitrarily chosen to be the master camera, and its first image of the specimen served as the reference image in the subsequent DIC analysis. Testing proceeded by incrementally moving the platform upwards (0.75 ± 0.59 mm) and capturing images of the specimen at each stopped location (Positions 2-25) (Figure 5.7). When testing ended, the platform had been displaced a total of 17.81 mm from its starting position and twenty-four sets of images had been collected over this range.

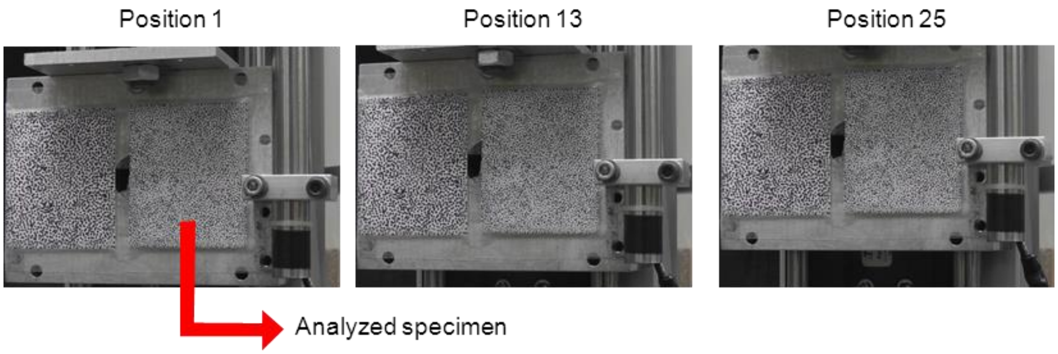

Figure 5.7: Starting, intermediate, and final positions of the specimen. In Positions 13 and 25, the platform had been displaced 7.20 mm and 17.81 mm, respectively, from the starting position, as measured by the LVDT.

The entire specimen was analyzed with DIC, resulting in a rectangular region of interest (ROI) approximately 60 mm x 50 mm (l x w) in size. The correlation was performed with a subset size of 35 pixels x 35 pixels. The matching algorithm, shape function, and interpolation order were chosen according to what was used in the first validation study. The 3D displacement fields were post-processed to find the total displacement of every point within the ROI relative to its starting location. For each of the twenty-four displaced positions, the total displacements were averaged over the ROI and compared with the displacements calculated with the LVDT positional data.

Results

Compared with the LVDT displacements, the root mean square (RMS) error of the DIC displacements was 0.05 mm. Figure 5.8 shows the DIC displacements plotted against the LVDT displacements. A least-squares regression line was fit to the data to determine the association between the two data sets. The slope of the line was 1.00, and the R^2 value was 1.00.

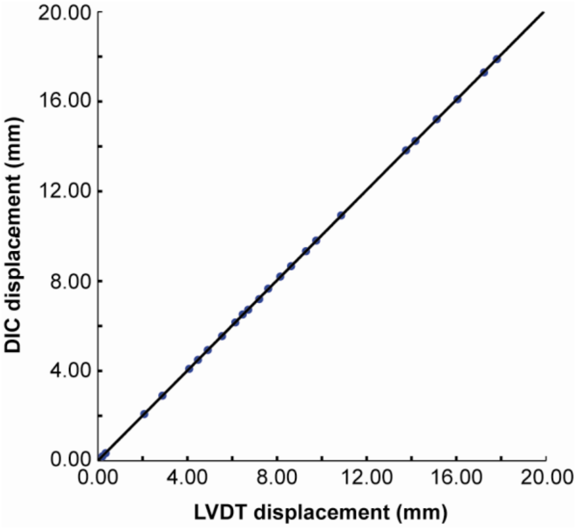

Figure 5.8: DIC displacements versus the LVDT displacements for the twenty-four displaced positions. The data were fit with a least-squares regression line ($R^2 = 1.00$).

5.3.4 Validation Study #3: Deformation and Strain Measurement

Methods

The goal of the third validation study was to test whether the 3D-DIC system could accurately measure both deformation and strain. The chosen specimen was a square of fabric cut from a microfiber polyester shirt (Nike Inc., Beaverton, OR, USA). As shown in Figure 5.4, the driving screw on the translation stage passed through two parallel plates—one attached to the fixed base and the other attached to the moving platform. The square of fabric was draped over the front edge of each plate and secured on both ends with a rubber-lined metal block and two c-clamps (Figure 5.9). The front edges of the two plates were level with one another. This ensured that the amount of pull applied to the bottom edge of the fabric could be directly measured with the LVDT.

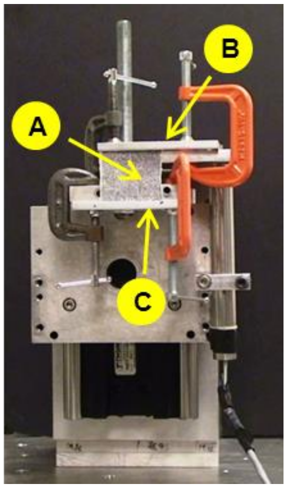

Figure 5.9: Specimen (A) mounted in the translation stage. The fixed grip (B) was attached to the base of the stage, and the moving grip (C) was attached to the platform.

Once the specimen was mounted in the translation stage, the position of the moving grip was adjusted until there was no visible slack in the fabric. At this point, the initial length of the specimen (39.67 mm) was measured with a handheld digital caliper and images of the specimen were captured with the two cameras (Position 1). The image from the Sony camera (again designated as the master camera) was used as the reference image in the DIC analysis. During testing, the platform was advanced downward to produce tension in the specimen. Similar to the second validation study, the platform was not displaced continuously; rather, it was moved by a discrete amount each time (1.04 ± 0.20 mm), and images were taken at every position (Positions 2-25) (Figure 5.10). In total, images of twenty-four, distinct deformed states were captured. The initial length of the specimen was 39.67 mm, and at the conclusion of testing, the fabric had been stretched to a final length of 64.22 mm.

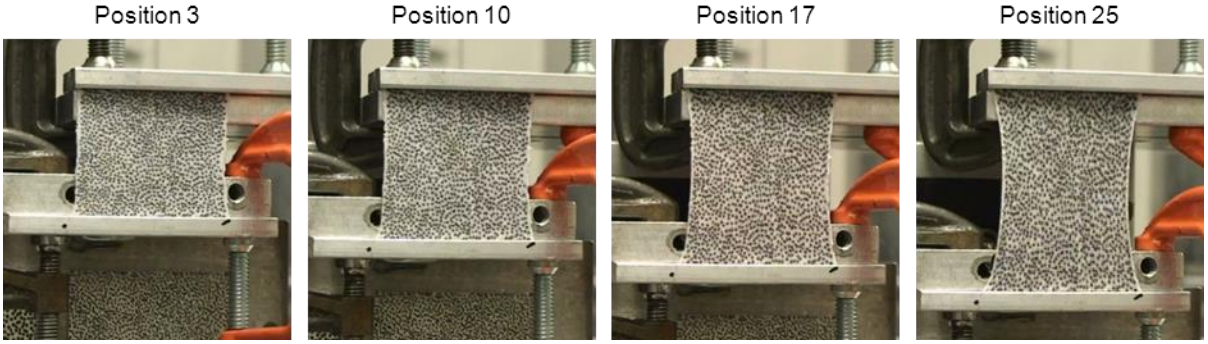

Figure 5.10: Specimen in four of its deformed states.

For the DIC analysis, an approximately square (10 mm x 10 mm) region in the center of the specimen was chosen for study. A right-handed Cartesian coordinate system was created with its origin in the upper left-hand corner of the specimen. The x-axis was aligned with the top edge of the specimen and pointed to the right; the y-axis was directed downwards in the direction of pull. The correlation was run with a subset size of 10 pixels x 10 pixels; and the same matching algorithm, shape function, and interpolation order used in the previous two studies. The resultant 3D displacement fields were post-processed to obtain the full-field first principal strains and principal directions in the ROI. For each deformed state, the principal strains and directions were averaged over the ROI.

The mean principal strains were compared with the true strain values computed with the LVDT positional data. The true strain was calculated using Equation 5.3, where *l* and *L* were the current and original lengths of the specimen, respectively.

$$\varepsilon = \ln\left(\frac{l}{L}\right) \tag{5.3}$$

Results

Figure 5.11 shows the full-field first principal strains for the four deformed states presented in Figure 5.10.

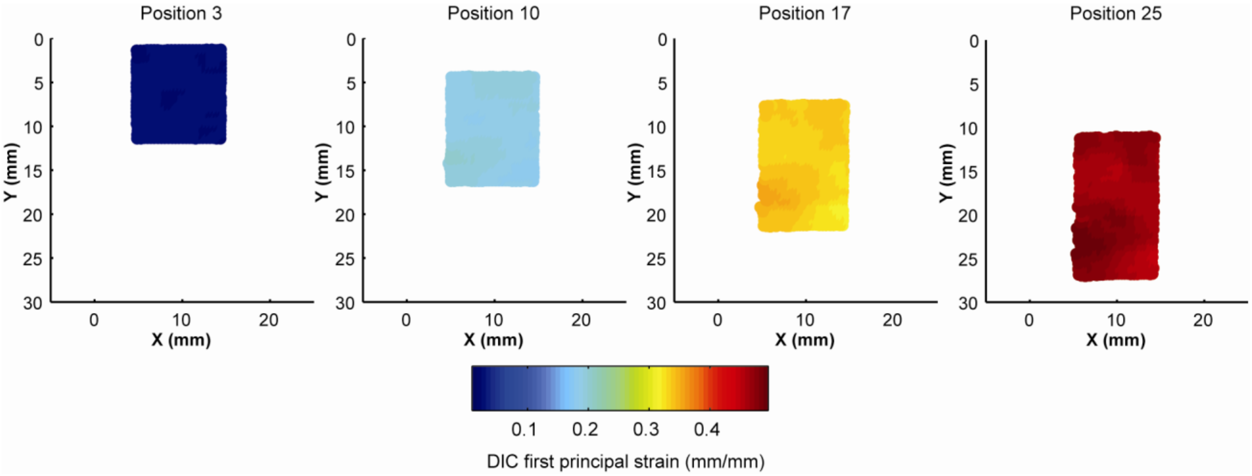

Figure 5.11: DIC first principal strains for the four deformed states shown in Figure 5.10. Over the ROI, the mean principal strains were 0.03, 0.19, 0.34, and 0.47 for Positions 3, 10, 17, and 25, respectively.

The DIC principal strains were plotted against the true strains for the twenty-four deformed states (Figure 5.12). The least-squares regression line had a slope of 0.97 with an R^2 value of 1.00.

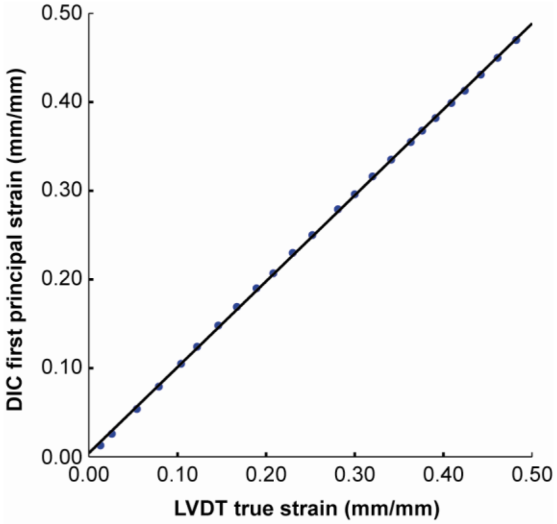

Figure 5.12: DIC first principal strains versus the true strains for the twenty-four deformed states. The data were fit with a least-squares regression line ($R^2 = 1.00$).

Similarly, Figure 5.13 shows the full-field principal directions for the four deformed states of Figure 5.10. Compared with the theoretical principal direction of 90 deg, the RMS error of the DIC principal directions was 1.3 deg.

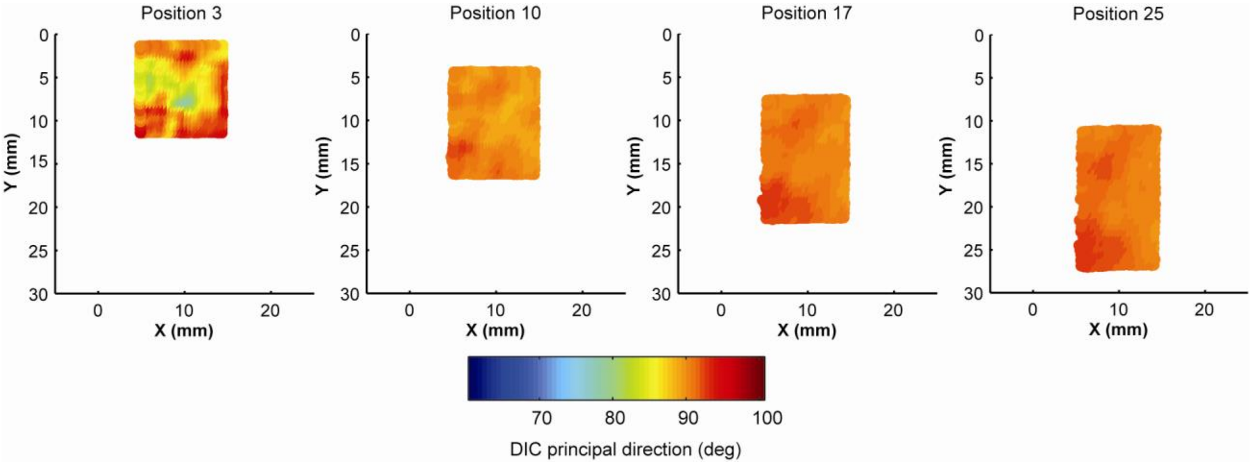

Figure 5.13: DIC principal directions for the four deformed states shown in Figure 5.10. Over the ROI, the mean principal directions were 89.1 deg, 90.7 deg, 91.6 deg, and 91.8 deg for Positions 3, 10, 17, and 25, respectively.

5.3.5 Validation Study #4: Dynamic Dimensional Accuracy

Methods

The purpose of the final validation study was to determine whether the 3D-DIC system could accurately recreate the geometry of a non-planar specimen while the specimen underwent rigid body motion. In essence, it was designed as an extension to Validation Study #1 (Section 5.3.2). It thus used the same specimen as that study: a solid cylinder whose surface was wrapped with a patterned strip of white paper. The cylinder was placed on a flat surface and held on a spindle that passed through its center (Figure 5.14). Two trials were performed in which the cylinder was hand rotated about the spindle axis while the cameras recorded at 30 fps. The cameras were operated via remote control, and a sync light was activated at the start of each trial to allow for later synchronization of the videos.

Figure 5.14: The specimen was placed on a flat surface and rotated about a spindle that passed through its center.

Following testing, the videos were post-processed in Adobe Premiere Pro (Adobe Systems Inc., San Jose, CA, USA). The videos from each trial were aligned with the sync light and five single-frame images were extracted from each video such that the angular displacement between successive images was approximately 2 deg (exact: 2.02 ± 0.51 deg). The DIC analysis was run with a subset size of 35 pixels x 35 pixels and the same matching algorithm, shape function, and interpolation order used in the previous validation studies. For each trial, the software output five 3D point clouds that represented the portion of the cylindrical surface that fell within the system's depth of field at each instant. From the point clouds, the diameter of the cylinder was determined at each time point using the same computational methods applied in the first validation study. The results were then compared to the measurements taken with a handheld digital caliper (Model CD-8 BS, Mitutoya America Corp., Aurora, IL, USA). The accuracy of the DIC measurements was assessed along with their stability throughout each trial.

Results

The mean diameter measured in each trial (representing the average of the five time points) was 51.02 ± 0.34 mm and 50.82 ± 0.32 mm. As previously mentioned, the diameter recorded with the handheld digital caliper was 51.12 ± 0.10 mm, representing the average of four measurements taken by the same observer. Compared with this value, the percent errors of the mean diameters were 0.20% and 0.59% for the first and second trials, respectively.

5.4 Discussion

While 3D-DIC is relatively straightforward to implement, its inner workings are complex. The most basic components of any analysis are image matching and triangulation. The latter refers to the system's ability to locate a point in 3D space given its projection onto two camera images. Every study involving DIC is an inherent test of whether the system can triangulate, but this ability was explicitly assessed in the first validation study. Because the facet capsular ligament has a distinct spherical curvature [46,102], the study was performed with a non-planar (cylindrical) specimen. The results showed that the system is capable of reconstructing both the shape and dimensions of a curved specimen with high fidelity. Furthermore, all four image collections yielded similar measurements of the cylinder's diameter (standard deviation = 0.24 mm) even though the cylinder was placed in a different location each time. This suggests that—provided the pattern remains in focus—the specimen can be shifted within the cameras' field of view while maintaining accuracy and precision during the triangulation.

The system's ability to perform image matching was examined in the second and third validation studies. They were designed to replicate two distinct types of pattern change: (1) one in which the pattern's speckles rigidly moved together (Validation Study #2) and (2) another in which the speckles displaced relative to one another (Validation Study #3). The third validation study was of particular interest since it more closely modeled the expected behavior of a soft tissue under load and the dimensions of the chosen ROI (10 mm x 10 mm) were similar to those of the lumbar capsular ligament [35,36,70]. The study thus reinforced that the system could reliably analyze a region on the required scale.

The DIC strains exactly matched the true strains up to 36% strain. Past this point, the DIC strains underpredicted the true strains by 1% strain, and this difference was present to the end of the test. The discrepancy in results could be due to errors in the DIC strains. For example, the fabric had regular rows of stitches, and as the specimen was stretched, the individual stitches separated, creating a sort of "secondary" pattern that was most distinct at the highest levels of strain. This could have confounded the correlation procedure, resulting in inaccurate DIC strains. Alternatively, 36% strain could represent an accuracy threshold of the DIC system. Though both these scenarios are possible, in general, DIC is considered to be a very robust method for measuring large deformations;

with appropriate image processing, it can measure strains in excess of 50% [103]. Additionally, the software output a "correlation score" for each subset evaluated within the ROI. The score was an indicator of the quality of the match between (1) the undeformed subset in the reference image and (2) the corresponding subset in the deformed image, with a score of 1.00 indicating a perfect match. For the final, deformed state of the test (Position 25), the mean correlation score was 0.99, indicating near-perfect matches for every subset under consideration. Given these results, the more probable cause of the discrepancy was an error in the calculation of the true strain. The most likely possibility is that in the later stages of the test, the specimen slipped at one (or both) of the grips. Though no slippage was visibly apparent during the test—and precautions were taken to prevent it—even small amounts would have led to a slight overprediction of the true strain, which would be consistent with the observed data sets.

Nevertheless, given the expected strain levels in the capsular ligament, the results of the study were promising. Both Panjabi et al. [45] and Ianuzzi et al. [47] have measured capsular ligament strains in human cadaveric lumbar specimens subjected to physiological loads (Section 3.1.2). The upper test limit of the validation study (48%) was two and a half times larger than the maximum strain observed by either group (19.3%). Furthermore, since the DIC and true strains were equivalent up to 36% strain, the system seems to have an appropriate resolution for determining physiological strains in non-pathological specimens. The question that arises naturally is whether the system is capable of measuring non-physiological, *pain-producing* strains. As discussed in Section 3.2.2, allodynia studies done with a rat model suggest that any strain above 21.5% can be considered a potential source of pain [23], and this threshold is well within the measurement range of the system.

With regard to directionality, the RMS error of the DIC principal directions was 1.3 deg. As shown in Figure 5.13, the full-field principal directions became progressively more homogeneous as the tension on the specimen increased. Accordingly, the largest spread in values occurred for the first deformed state (Position 2), where the mean principal direction was 85.2 ± 8.4 deg. The variation at low strain levels could be indicative of inadequate pretensioning at the start of the test. Though there was no obvious slack when the test began, there may have been small fiber misalignments or wrinkles that were visually imperceptible to the naked eye. This would have resulted in a non-uniform principal direction field in the early stages of the test, as was observed. The RMS error of the DIC principal strains was based on a theoretical principal direction of 90 deg. Because this may have been a poor assumption at low strain levels, a second RMS error was computed excluding the data point from the first deformed state (Position 2). When this was done, the error decreased to 0.8 deg. However, regardless of whether the data point from Position 2 is taken into consideration or not, the RMS error was deemed acceptable for measuring the directionality of capsular ligament strains relative to the gross anatomy of the joint.

The first three validation studies were all completed under static conditions. Though the specimens were displaced (or deformed) during testing, the images were collected *after* the displacement (or deformation) had already occurred. Consequently, the tests did not provide explicit information on the system's performance when tracking a moving specimen. To address this deficit, a final validation study was done to assess the system's accuracy under dynamic testing conditions. The study used the same cylindrical specimen as the first validation study, and images were collected continuously while the specimen rotated within the cameras' field of view. Though the system was able to reconstruct the specimen's shape throughout the trials, there was a slight decrease in the accuracy of its diameter measurement. (The percent error was 0.14% for Validation Study #1; and 0.20% and 0.59% for the two trials of Validation Study #4.) The drop in accuracy may have been caused by a small temporal misalignment between the videos since they were manually synchronized after testing. Alternatively, it may have been indicative of the software "losing" portions of the original ROI as it gradually rotated out of the system's field of view over the course of the trial. This latter issue underscores the importance of carefully configuring the stereo-rig to minimize potential data loss when the specimen undergoes rigid body motion.

5.5 Conclusion

DIC is an optical technique for taking full-field deformation and strain measurements, and it has been widely used in the field of biomechanics. 3D measurements are acquired with two cameras that have been calibrated as a unit and configured to simultaneously capture images of a specimen as it deforms. After testing, each deformed image is numerically correlated with the undeformed "reference" image using a matching algorithm that incorporates the pixel intensity information from both images. The resultant 3D displacement fields can be post-processed to obtain the in-plane normal and shear strain components.

Biological soft tissues present a number of challenges when characterizing their mechanical behavior. For this reason, DIC is a particularly attractive measurement technique because of its non-contact nature and ability to directly quantify large deformations and strains over a wide range of specimen sizes. To measure facet capsular ligament strains, a custom 3D-DIC system was built using two off-the-shelf camcorders and academic correlation software. The set-up was validated through a series of studies that determined the system's ability to accurately recreate a specimen's shape (under both static and dynamic testing conditions) and measure rigid body displacements, deformation, and strain. Overall, the results of the studies showed that the system has the desired resolution and accuracy for capturing the expected geometry and mechanical behavior of the lumbar capsular ligament.

Chapter 6. Study #2: Capsular Ligament Strains

6.1 Overview

The purpose of Study #2 was to use digital image correlation (DIC) to measure the full-field surface strains of the lumbar capsular ligament when the disc is intact and after the disc has undergone partial (PD) and subtotal (SD) microdiscectomies. Similar to Study #1, it was designed as a controlled laboratory study using cadaveric spinal specimens and a repeated measures approach. The collected data were used to test the following hypotheses:

- H_2: After PD and SD, the capsular ligament experiences significantly greater strains in response to physiological loads. The increases after SD are significantly greater than the increases after PD.
- H_3: After SD, physiological loading produces strains in the capsular ligament that exceed the threshold for pain (21.5%) [23]. The strain threshold is not surpassed after PD.

This chapter describes the experimental work, data processing, and analysis that were done for this study (Sections 6.2 and 6.3). The results are presented (Section 6.4), discussed, and compared to the findings from previous investigations that have measured capsular ligament strains in the lumbar spine (Section 6.5). Additional discussion of the research is included in Chapter 7, where the clinical implications of the work are highlighted.

6.2 Methods

6.2.1 Specimen Preparation

Eight lumbar motion segments (three L2-L3, three L3-L4, and two L4-L5) were obtained from three unembalmed human cadaveric specimens (T12-L5). The donors were three males, whose ages ranged from 52 to 63 years with a mean age of 58 years. Visual and radiographic screening were performed to preclude the existence of any pathology that could affect the mechanics of the individual motion segments. Special consideration was given to the overall health of the facet joints, including the absence of osteophytes and gross hypertrophies; and intact capsules free of perforations and tears.

Each specimen was dissected free of all non-ligamentous soft tissue. Metal screws were inserted into the terminal end of T12, and the end was embedded in polymethylmethacrylate with the screws providing additional fixation with the potting material. The vertebra that was potted on the specimen’s caudal end depended on the motion segment under consideration (L5 for L4-L5; and L4 for L2-L3 and L3-L4).

The L2-L3, L3-L4, and L4-L5 facet capsules were exposed with fine tissue dissection according to the morphological descriptions given by Yamashita et al. [36]. Each capsule was then randomly patterned with a black, ultra-fine point Sharpie marker (Newell Rubbermaid Office Products, Oak Brook, IL, USA) (Figure 6.1).

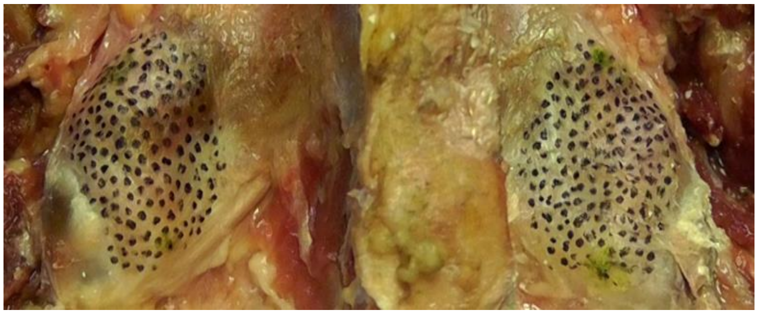

Figure 6.1: Patterned facet capsules of an L3-L4 motion segment.

6.2.2 Testing Equipment

Testing was performed with the custom-designed spine simulator described in Section 4.2.2. The forces and moments transmitted through the specimen were measured with a six-axis load cell (Model Omega 160, ATI Industrial Automation, Apex, NC, USA) beneath the inferior-most vertebra. The load cell was connected to a data acquisition board (Model PCI 6034E, National Instruments Inc., Austin, TX, USA) that sampled at a rate of 100 Hz. Segmental kinematics were collected by affixing a retro-reflective marker set to each vertebra comprising the motion segment under consideration. The marker sets were tracked with a four-camera Vicon MX13 system (Vicon Motion Systems, Lake Forest, CA, USA) sampling at a rate of 60 Hz.

The capsular ligament strains were measured with the custom three-dimensional (3D) DIC system presented in Chapter 5. The cameras were positioned on a stereo-rig approximately 0.3 m from the frontal plane of the facets. The cameras' focal lengths and the stereo-rig height were adjusted such that (1) the facets were centered in each camera's field of view and (2) the capsule patterning was in focus. A light source was placed behind the stereo-rig to illuminate the capsules and ensure the collection of high-quality images (Figure 6.2). The cameras' frame rates were set to 30 fps, and video recording was triggered via remote control at the beginning and end of each motion test.

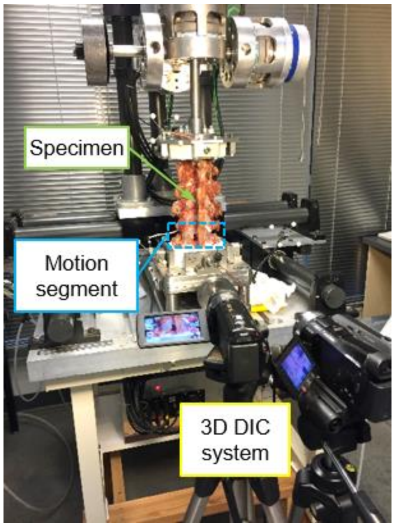

Figure 6.2: Experimental set-up showing a prepared specimen mounted in the spine simulator. The motion segment of interest is at the caudal end of the specimen and highlighted with a blue box. The DIC cameras were positioned posterior to the specimen to capture the deformation of the motion segment's facet capsules.

6.2.3 Testing Protocol

Each motion segment was tested in: (1) its intact condition and post- (2) PD and (3) SD. The surgical procedures were performed by an orthopaedic surgeon and entailed a left posterolateral approach with partial resection of the lamina.

The general testing protocol was similar to that used during Study #1. Under each condition, the motion segment was tested to maximum moments of ±15 Nm in flexion-extension (FE), lateral bending (LB), and axial rotation (AR) [49,71]. Two multi-axis tests were also performed (FRLB and FLLB) in which FE and LB moments were applied concurrently to the same limit (10.5 Nm) to create an off-axis bending moment with a vector-summed limit of approximately 15 Nm ($[(10.5\text{ Nm FE})^2 + (10.5\text{ Nm LB})^2]^{1/2} \approx 15$ Nm). In the FRLB test, flexion and right LB were applied together followed by extension with left LB. The FLLB test explored the reverse scheme (flexion with left LB followed by extension with right LB). The tests were conducted under continuous angular displacement control (2 deg/sec). Each test had three complete motion cycles, and the third cycle was used for analysis. A sync light was triggered at the start of each test to enable synchronization of the kinetic and kinematic data with the videos collected by the DIC cameras. Figure 6.3 illustrates the full testing protocol for a single motion segment, which was completed over the course of several hours on the same day.

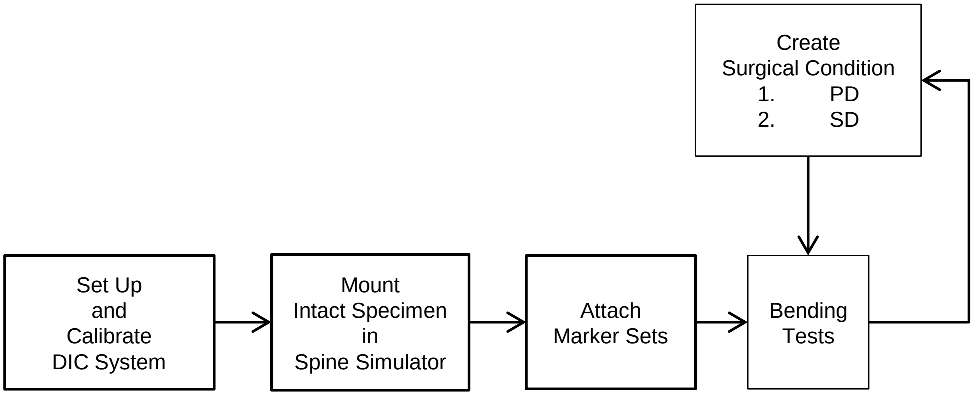

Figure 6.3: Flowchart of the testing protocol for an individual motion segment.

6.3 Data Processing and Analysis

6.3.1 Digital Image Correlation

The videos were post-processed in Adobe Premiere Pro (Adobe Systems Inc., San Jose, CA, USA). The two videos from each motion test were aligned with the sync light. The third cycle was isolated, and single-frame images were exported at the recorded frame rate (30 fps). The image sets were then decimated to minimize the computational time for the DIC analysis. This was done by only retaining the images that corresponded to every 1 Nm increment from the loading portions of the test. Each test had two different loading “conditions” (e.g. flexion and extension for the FE test), and the motion segment was loaded to a maximum moment of 15 Nm under each condition. Therefore, the decimation resulted in thirty “deformed” positions per test. Images were also extracted from the frame immediately preceding the appearance of the sync light, which served as the undeformed “reference” position for the subsequent DIC analysis.

Each motion test was analyzed by importing its image sets and the predetermined calibration parameters into the DIC software. A correlation was run on each facet capsule using a subset size of 33 pixels x 33 pixels; and the same matching algorithm, shape function, and interpolation order used in the DIC validation studies (Section 5.3). The resultant 3D displacement fields were post-processed to obtain the full-field first (E1) and second (E2) principal strains and principal directions in the capsules (Figure 6.4). The largest E1 and E2 strains were obtained from their respective full-field distributions and saved for later use. (Here, the term "largest" refers to the value with the greatest magnitude.)

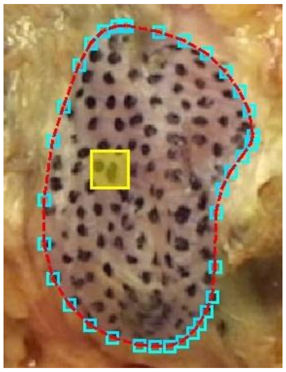

Figure 6.4: Right L2-L3 facet capsule with the region of interest outlined in blue and a sample subset shown in yellow.

6.3.2 Hypothesis H_2 Testing

A statistical analysis was performed to address hypothesis H_2. As described above, the full data set for Study #2 was fairly sizable, consisting of the largest E1 and E2 strains at every 1 Nm load increment for each testing condition, loading condition, and side. To reduce the complexity of the analysis, only a subset of the data set was considered. The subset consisted of the largest E1 and E2 strains at the endpoint of each loading condition (i.e. where the applied load was 15 Nm). (As will be shown in the subsequent section, for a given principal strain and loading condition, the difference between testing conditions was relatively consistent along the length of the loading curve. This observation helped justify the decision to only focus on the endpoint.)

The statistical analysis was done with a linear mixed-effects regression model (Appendix D) that tested for the association between the facet capsules' largest endpoint principal strains (the dependent variable) with testing condition and loading condition (the independent fixed effects).

Separate models were run for the left and right capsules. Hypothesis testing was performed with an omnibus test to determine whether the differences in mean strain varied across testing condition. If a significant difference was found, pair-wise comparisons among the three testing conditions were conducted. The significance level was set to $P < 0.05$.

6.4 Results

This section presents the capsular ligament strains that were measured under each loading condition. It also addresses the results from the testing of hypotheses H_2 and H_3.

In response to physiological loads, the facet capsule was shown to simultaneously experience both in-plane tensile and compressive strains—a phenomenon that has been documented by previous researchers in the cervical [46] and lumbar spines [47]. Therefore, for every loading condition considered in this study, the two principal strains (E1 and E2) were opposite in sign. To interpret the strains, it is useful to categorize each loading condition as either "tensile" or "compressive." As its name implies, during a tensile condition (e.g. flexion), the capsule was put in tension to passively constrain the motion of the intervertebral joint. The E1 strains represented a lengthening of the ligament, whereas the E2 strains signified a consequent narrowing in the perpendicular direction. In contrast, during a compressive condition (e.g. extension), the capsule compressed and did little to restrict the motion of the intervertebral joint. When this occurred, the presence of the E2 strains indicated that the ligament was relaxing, while the E1 strains represented a resultant "bulging" in the orthogonal direction. Tables 6.1 and 6.2 summarize these distinctions.

Table 6.1: Tensile and compressive loading conditions.

Tensile conditions	Compressive conditions
Flexion	Extension
Contralateral LB	Ipsilateral LB
Ipsilateral AR	Contralateral AR
Flexion + right LB	Extension + left LB
Flexion + left LB	Extension + right LB

Table 6.2: Meanings of the E1 and E2 strains during tensile and compressive loading conditions.

Loading condition	**Principal strain**	**Meaning**
Tensile	E1	Lengthening
	E2	Narrowing
Compressive	E1	Bulging
	E2	Relaxing

6.4.1 First and Second Principal Strains

The subsequent two figures depict sample full-field principal strain distributions in the facet capsules of an L3-L4 motion segment during the intact condition. Figure 6.5 is for a tensile condition (flexion), and Figure 6.6 is for a compressive condition (extension). The strains were measured at every 1 Nm load increment, but only three increments (5 Nm, 10 Nm, and 15 Nm) are shown for conciseness. The positions are given in the coordinate system of one of the DIC cameras, whose X-Y plane was approximately aligned with the frontal plane of the facets. Though the capsule is spherically curved [46,102], frontal plane projections are shown for ease of visualization. In this representation, the top of the image is superior, and the left and right sides of the image are lateral for the left and right capsules, respectively. Separate color bars are provided for the E1 and E2 strains to emphasize the heterogeneity of the strain fields.

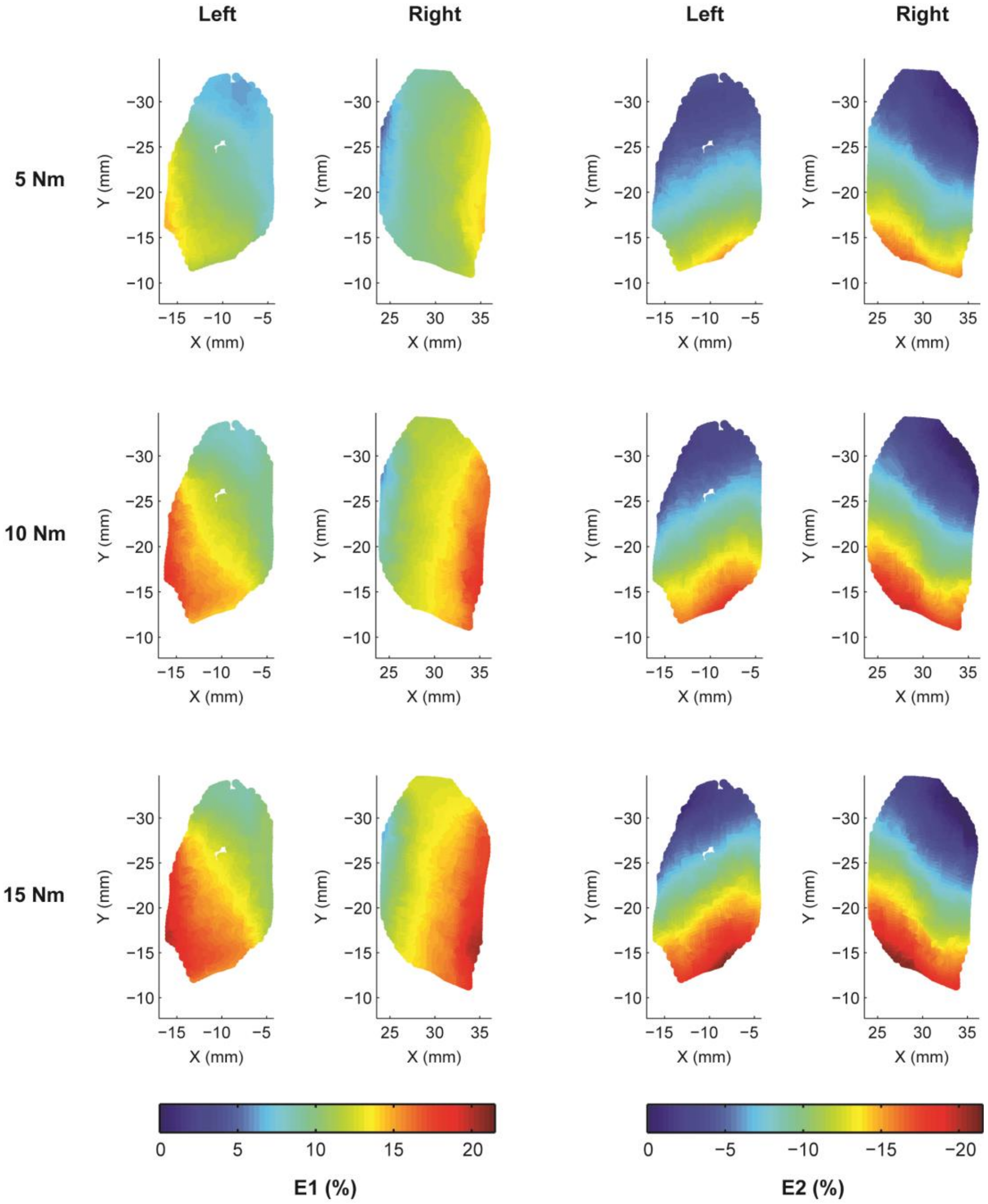

Figure 6.5: Exemplar full-field principal strain distributions in the facet capsules of an L3-L4 motion segment. The data are from a tensile loading condition (flexion). Each row is for a different load increment.

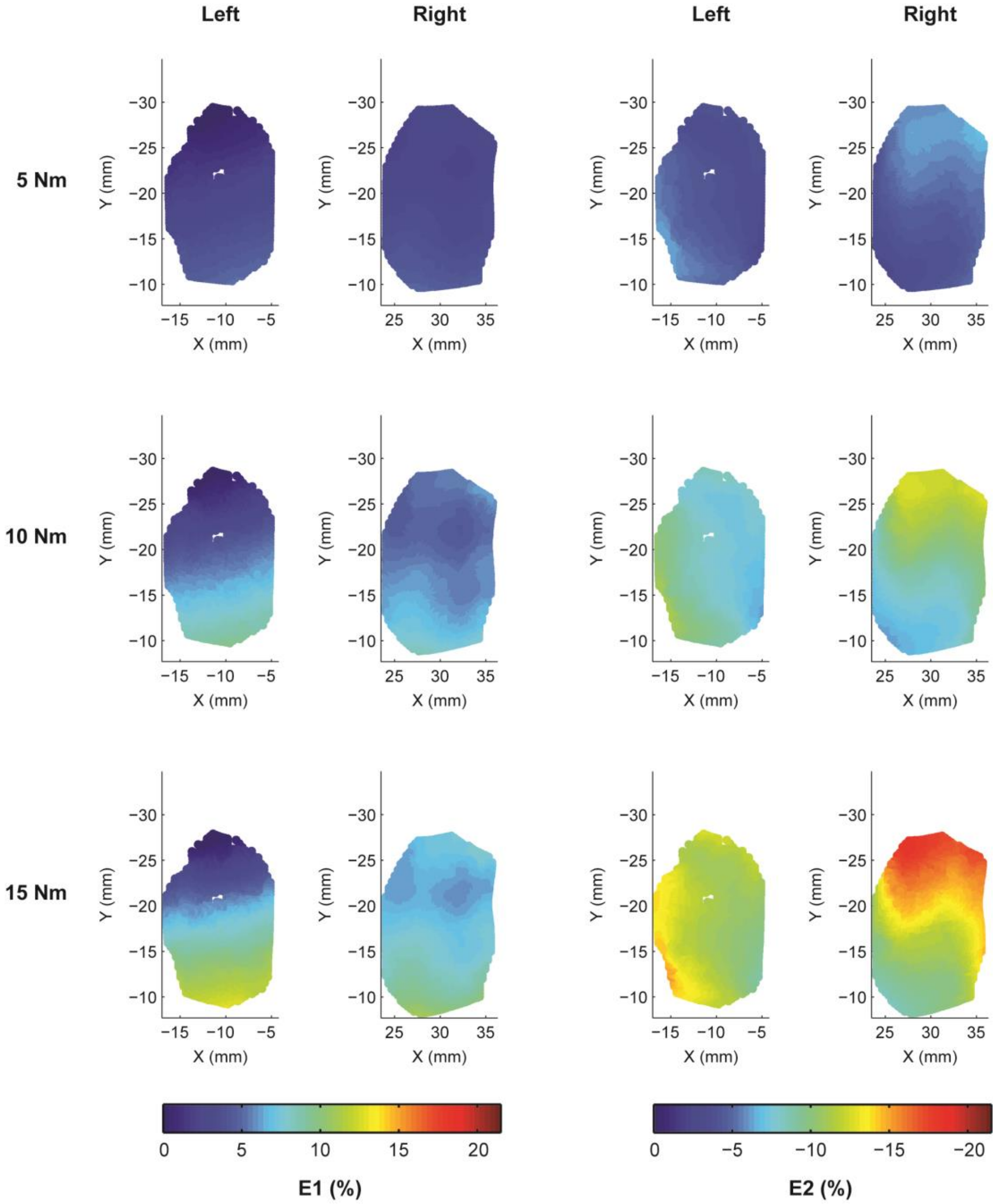

Figure 6.6: Exemplar full-field principal strain distributions in the facet capsules of an L3-L4 motion segment. The data are from a compressive loading condition (extension). Each row is for a different load increment.

Figures 6.7-6.11 present the largest E1 and E2 strains observed in the capsules. For each side, the data are averaged across the eight motion segments and separated by testing and loading conditions. The error bars represent one standard deviation from the mean. The hypothesized strain threshold for pain (21.5%) [23] is represented by solid and dashed red lines for the tensile and compressive conditions, respectively. Comparison of the strains with the threshold is discussed in Section 6.4.4.

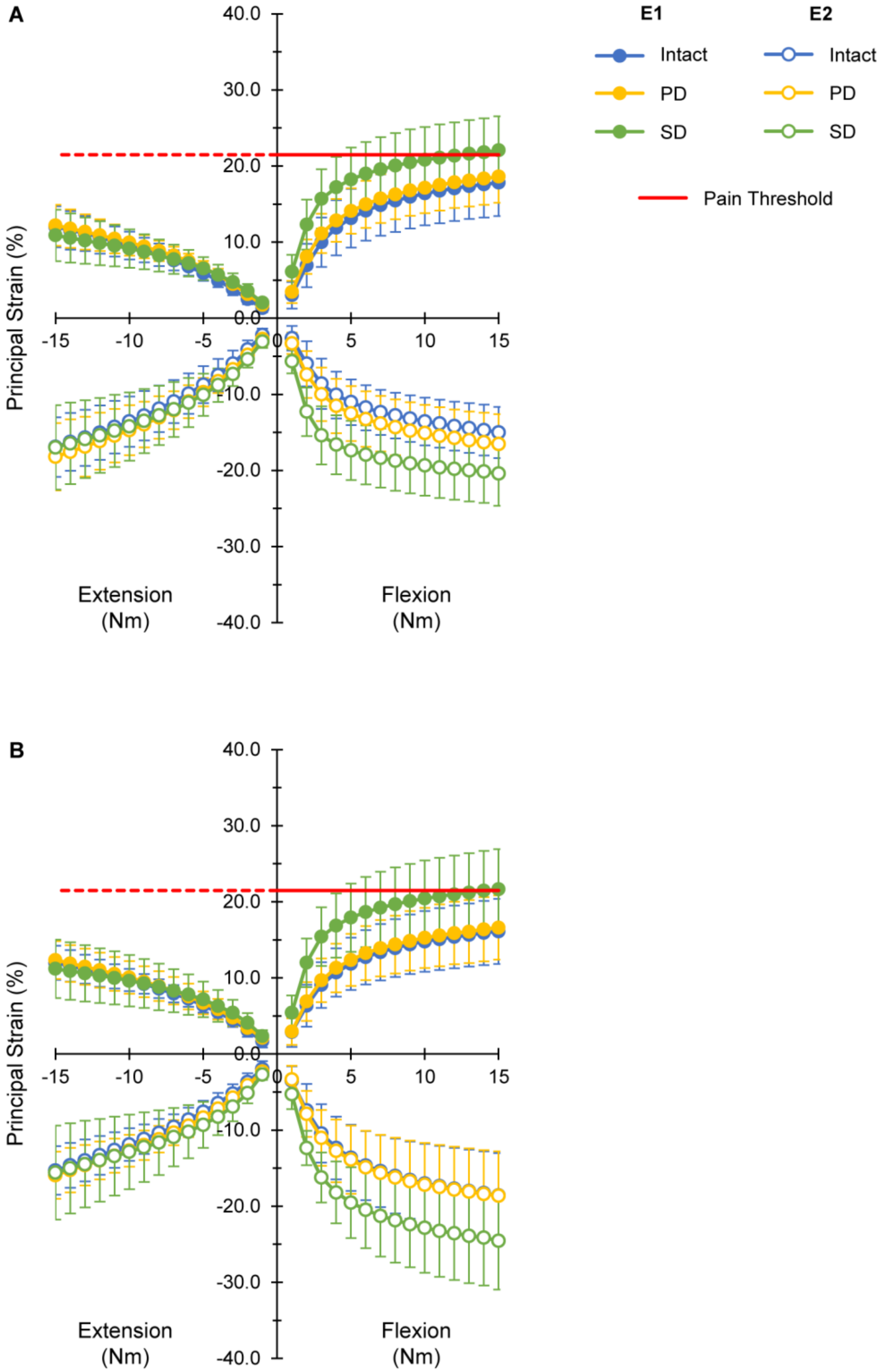

Figure 6.7: Largest E1 and E2 strains in the (A) left and (B) right facet capsules (n = 8) during flexion and extension.

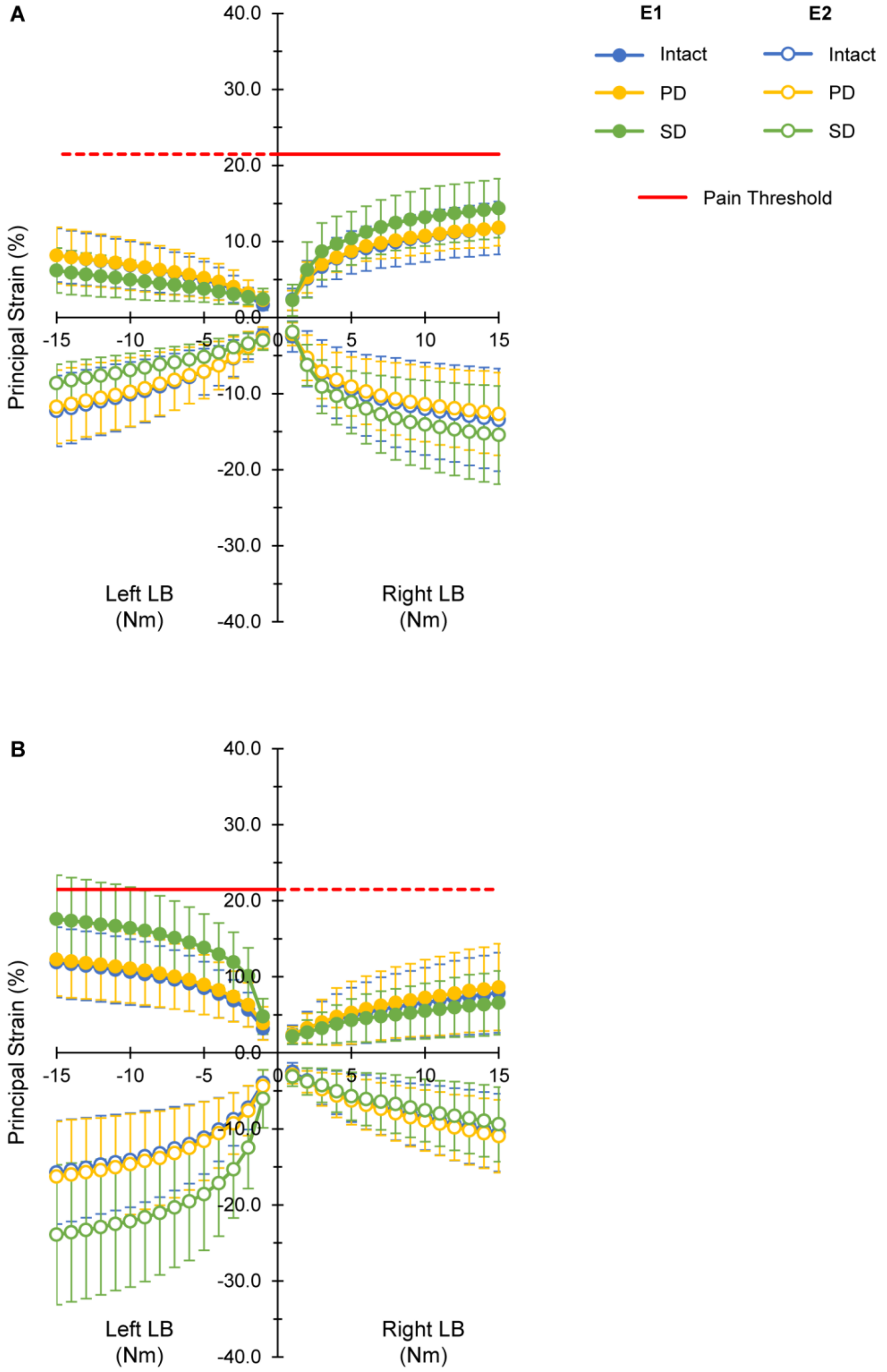

Figure 6.8: Largest E1 and E2 strains in the left (A) and right (B) facet capsules (n = 8) during right and left LB.

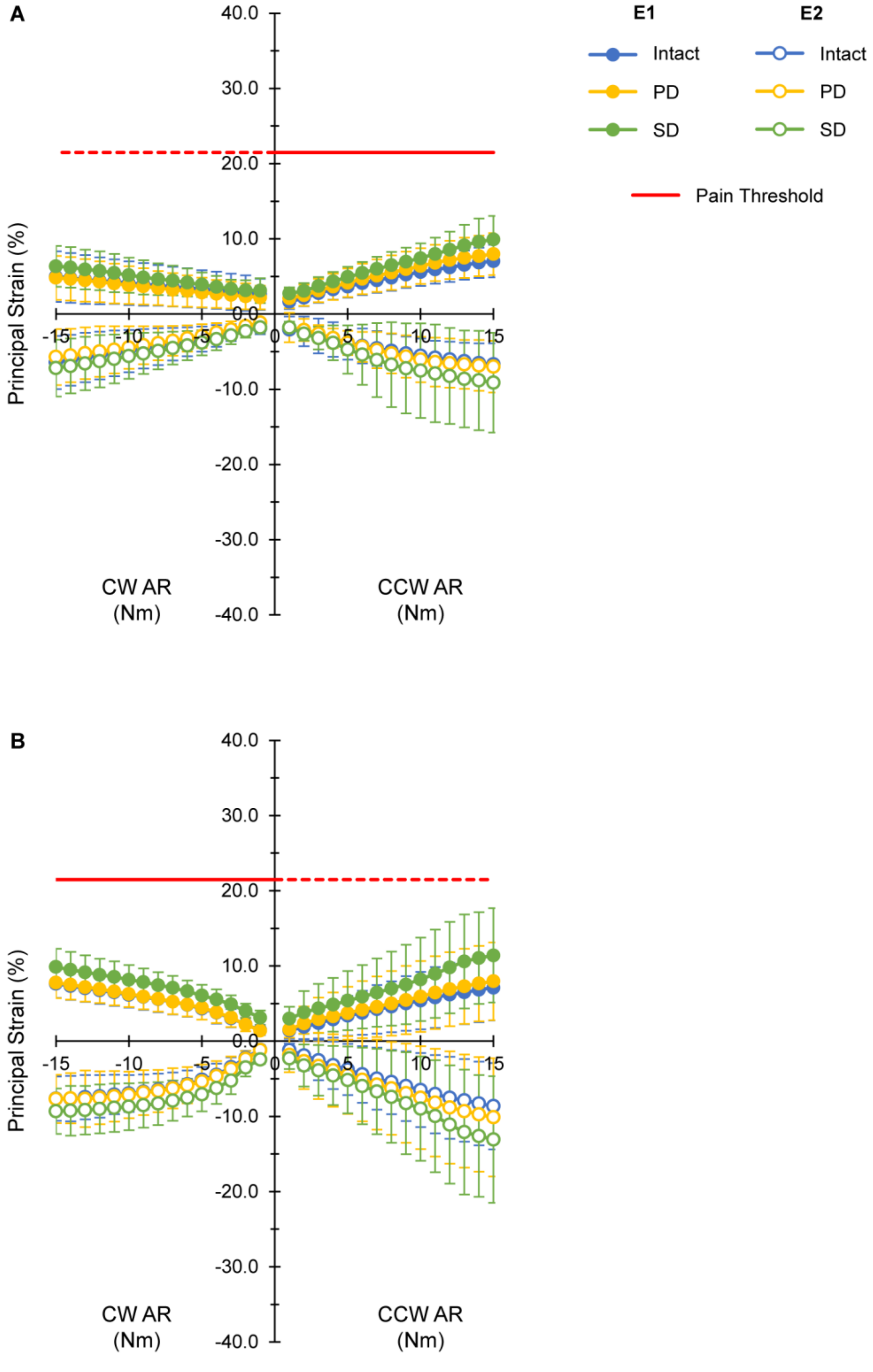

Figure 6.9: Largest E1 and E2 strains in the left (A) and right (B) facet capsules (n = 8) during counterclockwise (CCW) and clockwise (CW) AR.

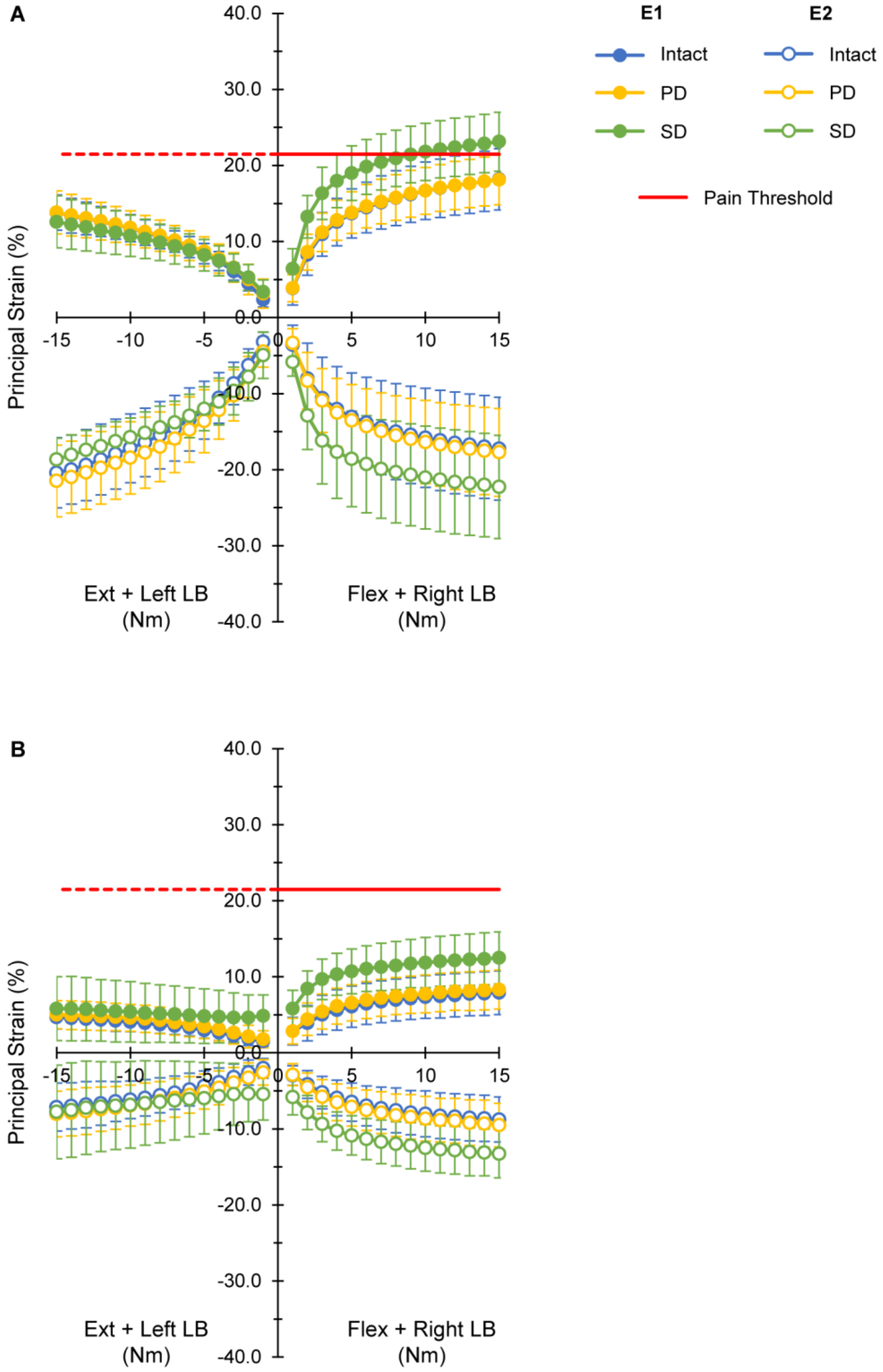

Figure 6.10: Largest E1 and E2 strains in the left (A) and right (B) facet capsules (n = 8) during flexion (flex) with right LB and extension (ext) with left LB.

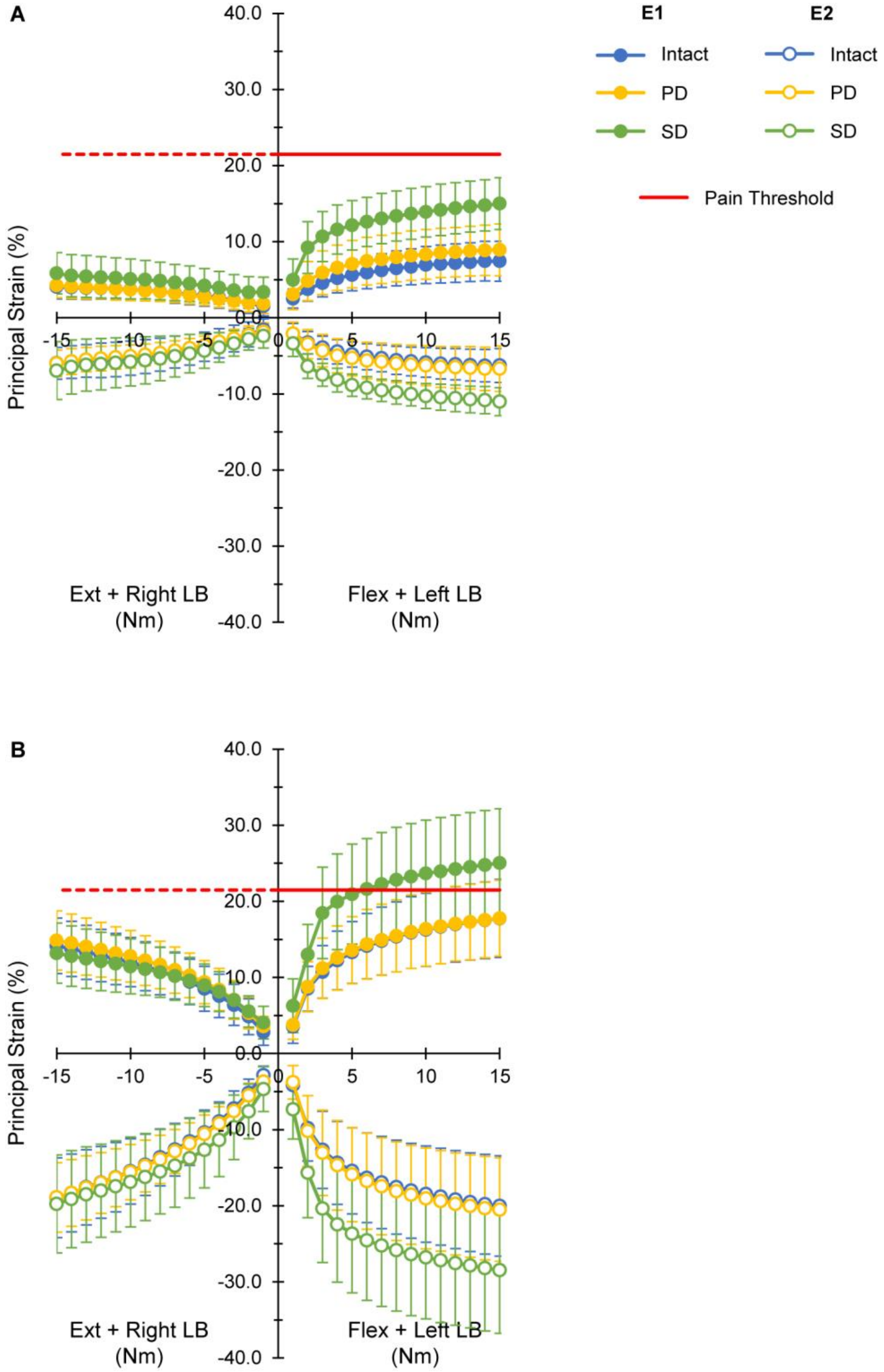

Figure 6.11: Largest E1 and E2 strains in the left (A) and right (B) facet capsules (n = 8) during flexion with left LB and extension with right LB.

6.4.2 Principal Directions

The orientations of the principal strains depended on whether the loading condition was tensile or compressive. Table 6.3 summarizes the general patterns that were observed.

Table 6.3: Orientations of the E1 and E2 strains during tensile and compressive loading conditions.

Loading condition	Principal strain	Orientation
Tensile	E1	Superomedial to inferolateral
	E2	Superolateral to inferomedial
Compressive	E1	Superolateral to inferomedial
	E2	Superomedial to inferolateral

Figures 6.12 and 6.13 depict the orientation of the E1 strains in the facet capsules of an L3-L4 motion segment. The figures are representative of the principal directions observed across the various loading conditions considered in this study. Figure 6.12 is for a tensile condition (flexion), and Figure 6.13 is for a compressive condition (extension). Similar to previous plots, only frontal plane projections are shown. The top of the figure is superior and the middle (between the plots for the left and right capsules) is medial. To assist with their interpretation, the figures are followed by a series of images that show the capsules when the motion segment was in maximal flexion and extension.

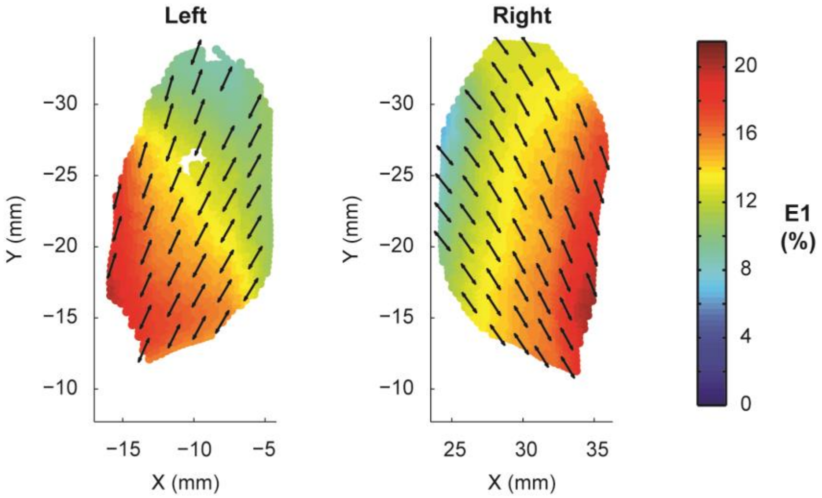

Figure 6.12: Typical orientation of the E1 strains during a tensile loading condition. The E1 strains were generally directed in the superomedial to inferolateral direction.

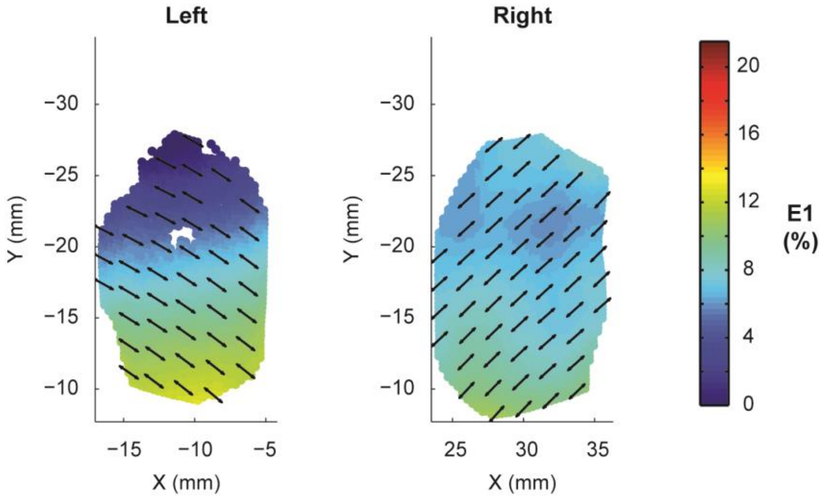

Figure 6.13: Typical orientation of the E1 strains during a compressive loading condition. The E1 strains were generally directed in the superolateral to inferomedial direction.

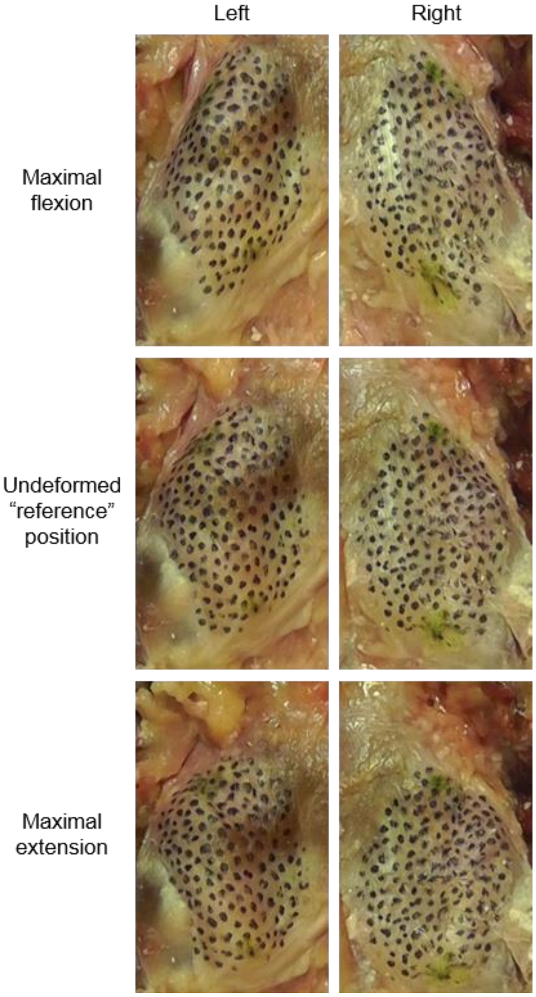

Figure 6.14: Images of the facet capsules when the L3-L4 motion segment (featured in Figures 6.12 and 6.13) was in maximal flexion, maximal extension, and the undeformed "reference" position.

6.4.3 Hypothesis H_2

Omnibus hypothesis testing showed differences in each of the largest endpoint principal strains (E1 and E2) by testing condition (Table 6.4). Pairwise comparisons were thus carried out among the three conditions. The results are given in Tables 6.5 and 6.6.

Table 6.4: Significant P-values ($P < 0.05$) from the omnibus tests. For each of the largest endpoint principal strains, these tests assessed whether the differences in mean strain varied across testing conditions.

Largest endpoint principal strain	**P-value**	
	Left facet	*Right facet*
E1	< 0.0001	< 0.0001
E2	0.030	< 0.0001

Table 6.5: Pairwise comparisons among the three testing conditions for the facet capsules' largest endpoint E1 strain. Mean differences and standard errors are given as percentages. P-values are listed only for statistically significant comparisons ($P < 0.05$).

Comparison		**Left capsule**			**Right capsule**		
I	*J*	*Mean difference (J-I)*	*Standard error*	*P-value*	*Mean difference (J-I)*	*Standard error*	*P-value*
Intact	PD	0.3	0.5		0.4	0.6	
Intact	SD	2.1	0.5	< 0.001	2.8	0.6	< 0.001
PD	SD	1.8	0.5	< 0.05	2.3	0.6	< 0.001

Table 6.6: Pairwise comparisons among the three testing conditions for the facet capsules' largest endpoint E2 strain. Mean differences and standard errors are given as percentages. P-values are listed only for statistically significant comparisons ($P < 0.05$).

Comparison		**Left capsule**			**Right capsule**		
I	*J*	*Mean difference (J-I)*	*Standard error*	*P-value*	*Mean difference (J-I)*	*Standard error*	*P-value*
Intact	PD	-0.3	0.6		-0.5	0.7	
Intact	SD	-1.6	0.6	< 0.05	-3.4	0.7	< 0.05
PD	SD	-1.3	0.6		-2.9	0.7	< 0.05

6.4.4 Hypothesis H_3

Of particular interest in this study was whether the capsular ligament experienced strains that were greater than the hypothesized threshold for pain (21.5%) [23] (hypothesis H_3). To address this hypothesis, one standard deviation above the mean maximum E1 strains was compared to the pain threshold for each of the testing and loading conditions. This is shown in Figures 6.7-6.11 where the pain threshold is depicted by solid and dashed red lines for the tensile and compressive conditions, respectively. As the figures illustrate, the pain threshold was only exceeded during the tensile conditions. Tables 6.7-6.9 give the results from the hypothesis testing. The color of each cell indicates whether the pain threshold was surpassed for that particular tensile condition (red = yes; green = no). For a positive result, the cell lists the loading range where it occurred.

Table 6.7: Hypothesis H_3 testing for the intact condition.

Capsule	**Loading condition**				
	Flexion	*Contralateral LB*	*Ipsilateral AR*	*Flexion + right LB*	*Flexion + left LB*
Left	≥ 13 Nm	🟩	🟩	≥ 13 Nm	🟩
Right	🟩	🟩	🟩	🟩	≥ 11 Nm

Table 6.8: Hypothesis H_3 testing for the PD condition.

Capsule	**Loading condition**				
	Flexion	*Contralateral LB*	*Ipsilateral AR*	*Flexion + right LB*	*Flexion + left LB*
Left	≥ 13 Nm	🟩	🟩	🟩	🟩
Right	🟩	🟩	🟩	🟩	≥ 11 Nm

Table 6.9: Hypothesis H_3 testing for the SD condition.

Capsule	**Loading condition**				
	Flexion	*Contralateral LB*	*Ipsilateral AR*	*Flexion + right LB*	*Flexion + left LB*
Left	≥ 5 Nm	🟩	🟩	≥ 4 Nm	🟩
Right	≥ 5 Nm	≥ 10 Nm	🟩	🟩	≥ 3 Nm

6.5 Discussion

The following section summarizes the major findings of this study, including (1) the overall strain patterns, magnitudes, and orientations and (2) a description of how these measures were affected by microdiscectomy. Whenever possible, comparisons are made with previous investigations. The section finishes with a discussion of the study's challenges and limitations.

6.5.1 Capsular Ligament Strains

There were several patterns of strain that were evident in all three testing conditions. Across the capsule, the principal strain distributions were non-uniform, similar to what has been observed in both the cervical [46] and lumbar [47] spines. However, for any given point on the capsule, the strains increased monotonically with increasing applied load [47]. Additionally, the magnitudes of the largest E1 and E2 strains were relatively consistent between specimens, but their locations on the capsule varied greatly [46].

Panjabi et al. [45] and Ianuzzi et al. [47] are the only two groups that have measured capsular ligament strains in human cadaveric lumbar specimens. Both studies focused on intact, non-pathological spines. Ianuzzi et al. [47] tested seven specimens (T12-S1) with a custom-built displacement-controlled loading apparatus. FE and LB were induced in the specimens by horizontally displacing T12; and capsular strains were measured by optically tracking the displacement of an array of markers that were glued to the capsule's surface. Ianuzzi et al.'s [47] loading technique produced intervertebral joint moments that were relatively minor from a physiological standpoint. But compared to Panjabi et al. [45], their methods for measuring strain and the measurements they reported (largest E1 and E2 strains) were more closely aligned with the present investigation. These similarities facilitated a comparison with their study, the results of which are shown in Table 6.10. In the table, the moments and strains given for Ianuzzi et al. [47] are the average values observed at levels L2-L3, L3-L4, and L4-L5. The strains listed for the current study are for the intact condition and were extracted from the lower end of the applied loading range to better compare with Ianuzzi et al.'s [47] results.

Table 6.10: Comparison of the lumbar capsular ligament strains measured by Ianuzzi et al. [45] with those of the current study (in the intact condition).

Study	**Loading**		**Largest E1 strain (%)**		**Largest E2 strain (%)**	
	Direction	*Magnitude (Nm)*				
Ianuzzi et al. [47]*			Left	Right	Left	Right
	Flexion	2.0	8.6	7.1	-7.0	-4.4
	Extension	3.4	6.8	5.0	-6.5	-5.9
	Right LB	2.8	6.1	4.4	-6.4	-1.9
	Left LB	3.6	3.2	6.3	-3.0	-5.9
Current study			Left	Right	Left	Right
	Flexion	2	6.9	6.3	-6.0	-7.4
	Extension	3	3.8	4.4	-6.0	-5.2
	Right LB	3	6.6	3.9	-7.3	-4.5
	Left LB	4	4.5	7.8	-6.3	-10.1

*Moments and strains are at 40 mm of horizontal displacement of T12.
Moment and strain values were estimated from graphs using ImageJ (National Institutes of Health, Bethesda, MD, USA).

As can be seen in Table 6.10, under equivalent loading, the strains measured in this study were commensurate with those reported by Ianuzzi et al. [47]. Additionally, there were several consistent trends between the investigations. Like this study, Ianuzzi et al. [47] found that the two principal strains—though opposite in sign—were of similar magnitude for a given loading condition and side. The largest E1 strains occurred during flexion; and in LB, the principal strains in the contralateral capsule were of greater magnitude than those in the ipsilateral capsule. Finally, though not explicitly shown in the table, both studies demonstrated a nonlinear relationship between strain and moment. Unlike this investigation, Ianuzzi et al.'s [47] applied loads were too small to produce an eventual plateau in the strains (Figures 6.7-6.11). Nevertheless, given the aforementioned similarities, it is reasonable to assume that if the researchers had increased their applied loads, they would have also observed a sigmoidal relationship between these two variables.

Unfortunately, Ianuzzi et al. [47] did not explicitly map out the distributions or orientations of their measured strains. However, the authors' description of the strains' directionality was consistent with what was seen in this investigation. Namely, in all three testing conditions, the orientations of the principal strains depended on whether the loading condition was tensile or compressive in nature. In the tensile conditions, the E1 strains were primarily oriented in the superomedial to inferolateral direction, while the E2 strains were approximately perpendicular to that direction. The opposite held true for the compressive conditions. Similar trends have also been noted in two other studies that looked at tensile loading of cervical facet capsules in humans [46] and goats [65].

Overall, under analogous loading conditions, the strain patterns, magnitudes, and orientations were comparable to what has been previously reported for the facet capsules of the cervical [46,65] and lumbar [45,47] spines. These similarities helped validate the use of DIC to measure the capsular ligament strains.

6.5.2 Strain Response to Microdiscectomy

This investigation examined the effects of microdiscectomy on the strains in the capsular ligament. While there have been two other studies that have measured capsular strains in the lumbar spine [45,47], both focused exclusively on intact, non-pathological spines. Furthermore, every study on non-physiological strains was done with an animal model, and the strains were artificially induced by manually distracting the facet joint [21–23,65,68,69]. Because of these methodological differences, it is difficult to draw firm comparisons with these investigations. Nevertheless, as discussed in Chapter 4, several groups *have* reported a correlation between disc excision and the motion of the intervertebral joint [20,79]. It is reasonable to assume that when the intervertebral joint exhibits increased motion, at least some of it can be attributed to increased motion of the facets. Furthermore, if one assumes that facet motion is proportional to the strain in the capsule, then—collectively—the existing body of research suggests that disc excision should result in larger capsular strains.

Overall, the results of this study confirmed this prediction. Microdiscectomy was shown to alter the strains in the capsule, but in general, the effects were only seen after the more invasive of the two procedures (SD). As previously mentioned, across motion segments (and even between capsules of the *same* motion segment), there was widespread variation in the strain distributions and the exact locations of the largest strains. However, for a given capsule and loading condition, these two qualities were relatively consistent between testing conditions. The main difference after SD was in the magnitude of the strains—both in terms of the average strain across the capsule and the largest strains that occurred. Figure 6.15 illustrates these patterns by presenting the full-field E1 strain distributions in every testing condition for the right capsule of an L3-L4 motion segment. Like previous plots, the images are frontal planar projections, where the top of the image is superior and the right side is lateral.

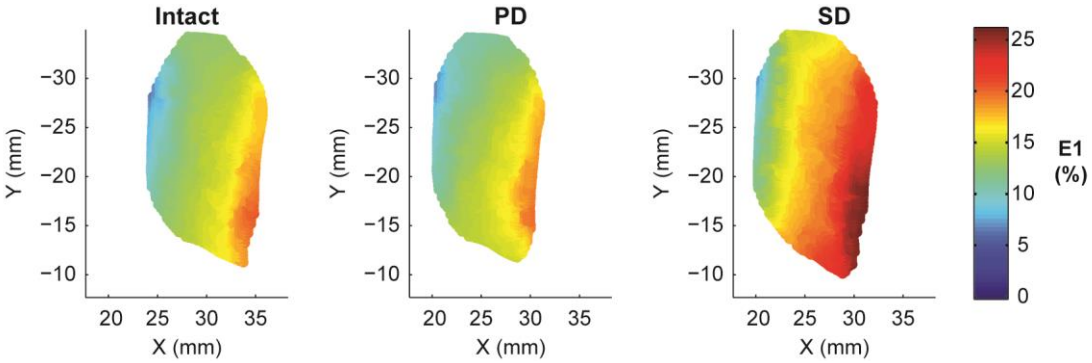

Figure 6.15: Comparison of the full-field E1 strain distributions between testing conditions for the right facet capsule of an L3-L4 motion segment. For each condition, the data were taken when the motion segment was in maximal flexion. Across the capsule, the mean (and maximum) E1 strains were 14.1% (20.4%), 13.9% (19.8%), and 18.1% (26.2%) for the intact, PD, and SD conditions, respectively.

Aside from these observations, one of the most prominent trends seen in this study was that the increased strains after SD only occurred under tensile loading conditions. Ipsilateral AR was the one tensile condition that did not fully demonstrate this trend; though the *average* strain across the capsule was greatest after SD, the largest E1 and E2 strains were similar in every testing condition. This finding was not surprising given the importance of the facet joints in protecting the disc from excessive AR. Adams and Hutton [104] reported that torsion of the lumbar spine is primarily resisted by compression of the contralateral facet joint's articular surfaces. Thus, large increases in facet motion (and resultant increases in capsular strain) would be unlikely barring a local collapse in the subchondral bone or cartilage of the articulating surfaces. Excluding ipsilateral AR, in every other tensile condition, SD produced increases in the average and largest values of the principal strains. Intuitively, it made sense that the E1 and E2 strains rose in tandem. The loading conditions considered in this study simultaneously subjected the capsules to both in-plane tensile and compressive strains. Because the two principal strains were intimately related, an increase in one naturally led to an increase in the other.

The statistical analysis of hypothesis H_2 confirmed the general observation that SD (but not PD) resulted in increased capsular strains. For both sides, the largest endpoint principal strains were significantly greater after SD compared to the other two conditions. The one exception was for the left capsule's largest endpoint E2 strains. In this case, the pairwise comparisons only revealed a significant difference between the intact and SD conditions ($P < 0.05$).

Like Study #1, there was some indication of an underlying asymmetry in the capsules' strain response to microdiscectomy. In the intact condition, the respective magnitudes of the largest E1 and E2 strains were comparable between sides. Though larger strains developed in both capsules after SD, the procedure seemed to have a more pronounced effect on the contralateral capsule. The difference was most apparent in LB. For example, when the motion segments were in maximal right LB, the largest E1 strain measured in the left capsule was 14.4 ± 3.9%, which represented a 22% increase from the intact condition (11.8 ± 3.5%). In contrast, during maximal left LB, the largest E1 strain observed in the right capsule was 17.6 ± 5.7%. This was a 48% increase from what was seen in the intact condition (11.9 ± 4.6%). Flexion with contralateral LB seemed to also affect the right capsule more, but the discrepancy between sides was less extreme.

With regard to hypothesis H_3, the hypothesized strain threshold for pain (21.5%) [23] was only surpassed during tensile loading conditions. In the intact and PD conditions, the mean maximum E1 strains were never larger than 21.5%; however, when the comparisons were made with one standard deviation above the mean, there were a handful of cases when they were. This implies that even in non-pathological spines, loads at the upper end of the physiological range can occasionally produce strains that may be high enough to elicit pain. After SD, the strains in each capsule exceeded 21.5% in flexion and flexion with contralateral LB. The required loads were lowest in the combined loading cases. Unlike the other two testing conditions, even the mean maximum E1 strains were large enough to surpass the pain threshold in these loading conditions. Finally, of particular note was that in contralateral LB, only the right capsule was identified as a potential source of pain. While the required loads were higher than what was needed in the aforementioned loading conditions, this observation further supported the notion of an underlying side asymmetry. The clinical implications of these findings are discussed in depth in Chapter 7.

6.5.3 Limitations

Like any study, this investigation was not without its limitations. As an *in vitro* cadaveric study, it was subject to the same limitations previously mentioned for Study #1 (Section 4.5.3). Specifically, it did not account for the presence of body weight or muscle activation; the results were only representative of the initial postoperative period; and the order of the testing conditions could not be randomized for each motion segment. Additionally, each motion segment underwent several freeze-thaw cycles during preparation and testing. In part, the multiple freeze-thaw cycles were a consequence of the study design. Three T12-L5 specimens were obtained for this study, and two or three motion segments were tested per specimen. Rather than preparing the motion segments as individual functional spinal units, however, the specimens were kept intact and the motion segments were tested sequentially in the order: L4-L5, L2-L3, and L3-L4. This was done intentionally to maximize the distance between the upper and lower potting fixtures. This prevented the upper fixture from occluding the capsules of interest when the specimen rotated during testing. While this set-up enhanced the cameras' visibility, it resulted in one or two additional freeze-thaw cycles for several of the motion segments.

The sample size (n = 8) was another limitation of this study. The linear mixed-effects regression model revealed differences in the largest endpoint principal strains between testing conditions. Similar to Study #1, however, there was no evidence that the *pattern* of differences between testing conditions varied between loading conditions. As discussed above, one of the most prominent trends that emerged from the data was that the principal strains were only affected by disc excision when the applied load was tensile in nature. Unfortunately, the statistical model was unable to verify this observation because of the limitations imposed by the small sample size.

Aside from these issues, there were several other challenges encountered over the course of the study. One of the biggest challenges involved the hydration of the tissue. Previous biomechanical studies have shown that changes in water content affect the viscoelastic properties of soft tissues [105–108]. For *in vitro* testing without an environmental chamber, tissue hydration is normally maintained by spraying the tissue with water at regular intervals. Unfortunately, standing moisture on the capsules produced specular reflections that obscured the underlying pattern. In an attempt to overcome this problem, a two-step hydration process was adopted. After spraying the capsules, the tissue was allowed to soak up the water for several minutes. At that point, each capsule was lightly dabbed with a paper towel to remove any water droplets that remained on its surface. This prevented the tissue from becoming desiccated while still promoting the collection of high-quality images. Despite best efforts, however, there were still some cases in which there was enough moisture in a particular location to create problems during the DIC analysis. When this happened, the correlation would typically fail in that area, creating a “gap” in the full-field strain distributions. (In Figures 6.12 and 6.13, a gap of this nature is visible in the middle region of the left capsule’s full-field strain distributions.) Often times, these gaps were not close to the positions of the largest E1 and E2 strains, so their presence was a non-issue. But when they were, it was possible that the recorded strains were underestimating their actual values.

A second challenge that arose concerned the cameras’ visibility. In an idealized situation, each capsule’s entire pattern would remain visible—and in focus—throughout testing. In reality, this was never the case. One stereo-rig was used to collect images of both capsules. Thus, when the cameras’ positions were adjusted at the start of testing, it was *always* a compromise between enhancing the visibility of one capsule while reducing the visibility of the other. Furthermore, at times (generally at the loading extremes of a motion test), the motion segment would rotate in such a way that portions of the capsules' peripheral areas would pass out of the cameras' field of view. With a single stereo-rig, these situations were unavoidable; though even with additional cameras, it would still be difficult to capture the entire posterior aspect of both capsules simultaneously. The loss of visibility meant that there were parts of each capsule that were not accounted for in the DIC analysis. Again, this could have resulted in an underestimation of the largest E1 and E2 strains.

6.6 Conclusion

Study #2 examined the effects of two microdiscectomy procedures on the full-field surface strains of the lumbar capsular ligament. Of the two procedures, only SD significantly increased the strains in the capsule. With the exception of ipsilateral AR, the increases were exclusively seen under tensile loading conditions. In: (1) flexion, (2) flexion with LB (right and left), and (3) left LB, the strains were large enough to surpass the pain threshold in one (or both) capsules. The general observations were confirmed by a statistical analysis that tested for an association between the capsules' largest endpoint principal strains with testing condition. Similar to Study #1, there was some evidence of a (left versus right) side effect, with SD disproportionately affecting the strains in the contralateral capsule. The side asymmetry was most pronounced for the loading conditions that involved LB.

Chapter 7. Conclusions

This research was motivated by the desire to understand how partial (PD) and subtotal (SD) microdiscectomies alter the biomechanics of the lumbar facet joints. The response of the facet joints was described by (1) the three-dimensional kinematics of the facets and (2) the strains in the capsular ligament that surrounds the joint. These metrics were explored in two separate *in vitro* studies using human cadaveric spinal specimens and a repeated measures approach.

The subsequent sections of this chapter summarize the major findings from each study, which include brief explanations of whether the hypotheses that motivated the research were ultimately accepted or rejected (Sections 7.1 and 7.2). The connections between the two studies are discussed along with the clinical implications of the results (Section 7.3). The chapter concludes by making recommendations for potential future research efforts (Section 7.4).

7.1 Facet Kinematics

The major findings from Study #1 are listed below:

1. A coordinate system based on the geometry of the facet's articular surface allows the motion of the facets to be described in anatomically-relevant terms (Figure 7.1).
2. The facets' primary directions of motion were translations along the U-axis and rotations about the V- and W-axes. The largest motions in these directions occurred during flexion-extension (FE), lateral bending (LB), and the two combined FE with LB tests.
3. The facets' secondary directions of motion were translations along the W-axis and rotations about the U-axis. The largest motions in these directions occurred during axial rotation (AR).
4. Compared to the intact condition, SD significantly increased the motion of the facets along the primary directions of motion.

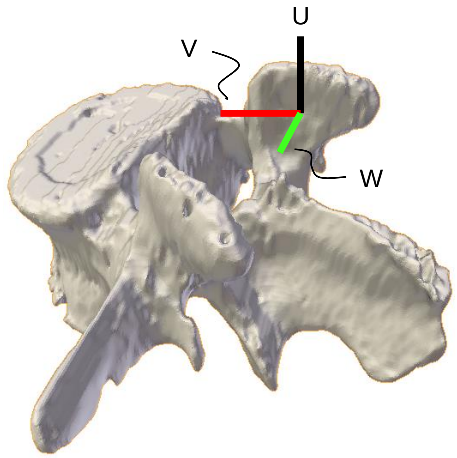

Figure 7.1: Representative facet with the axes of its coordinate system. The origin was centered on the articular surface. The U- and V- axes lay within the best-fit plane of the articular surface. The U-axis pointed superiorly, and the V-axis was directed anteriorly and medially. The W-axis was the normal to the best-fit plane. Its orientation was consistent with a U-V-W right-handed Cartesian coordinate system.

Hypothesis H_1 was only partially supported. After SD, the facets exhibited significantly more motion than they did in the intact condition, with the increases occurring along the primary directions of motion. Unfortunately, the results pertaining to the PD condition were largely inconclusive. With one exception, there was no evidence that the motion seen after PD differed from what was measured in the intact or SD conditions.

7.2 Capsular Ligament Strains

The major findings from Study #2 include the following:

1. In response to physiological loads, the capsule experienced both in-plane tensile and compressive strains.
2. The orientations of the principal strains depended on whether the loading condition was tensile or compressive in nature.
3. For a given capsule and loading condition, the strain distributions and locations of the largest strains were relatively consistent between testing conditions.
4. After PD, there was no evidence that the capsules' largest endpoint principal strains were significantly different from what was measured in the intact condition.
5. After SD, the capsules' largest endpoint principal strains were significantly greater than what was measured in the intact and PD conditions.

6. The increased strains after SD only occurred under tensile loading conditions.
7. After SD, the capsules experienced strains that surpassed the hypothesized strain threshold for pain (21.5%) [23] in: (1) flexion, (2) flexion with right and left LB, and (3) LB ipsilateral to the site of surgery.
8. Digital image correlation is a reliable and accurate technique for measuring the full-field surface deformation and strain in the capsular ligament.

Hypothesis H_2 was partially supported. After SD, the strains in the capsule were significantly larger than what was observed in both the intact and PD conditions. But contrary to what was predicted, there was no evidence that the strains after PD differed from what was seen in the intact condition. With a small caveat, hypothesis H_3 was fully confirmed. After SD, the hypothesized strain threshold for pain was surpassed in one (or both) capsules in four separate loading conditions. The pain threshold was *also* exceeded in both the intact and PD conditions. However, this only occurred at the upper end of the study's applied loading range when the comparisons were made with one standard deviation above the mean maximum E1 strains.

7.3 Clinical Implications

Even though the previous two sections separately summarized the findings from each investigation, it is important to remember that the strains in the capsular ligament are intrinsically linked to the kinematics of the facets. Thus, it can easily be seen that the results from Study #1 readily translate to those from Study #2. For a particular degree of freedom (DOF), the mobility of the facets depends on a number of factors, including: the congruence of the articular surfaces; the amount of articular surface available; and the orientation and stiffness of the capsule. Based on these factors and the anatomy of the facet joint, the motion patterns observed in the first study were unsurprising. The facets' kinematics were primarily characterized by translations along the U-axis and rotations about the V- and W-axes because these are the DOFs that afford the facets the most mobility. Consequently, they are also the DOFs that have the potential to induce the largest strains in the capsules. Therefore, one would expect that the motion tests where the facets exhibited the largest ranges of motion (ROMs) (in Study #1) would predict the loading conditions where the capsular strains had their greatest magnitudes (in Study #2). And, in fact, this is exactly what happened (Table 7.1).

Table 7.1: The motion tests where the facets had the largest ROMs (in Study #1) translated to the loading conditions where the capsular strains had their greatest magnitudes (in Study #2). Refer to Appendix A for the meanings of the abbreviations.

Side	**Motion tests with largest ROMs**	**Loading conditions with largest strains**
Left	FE FRLB	Flexion Flexion + right LB
Right	FE FLLB	Flexion Flexion + left LB

Interestingly, both studies also hinted at a possible side asymmetry after SD, with the procedure having a more pronounced effect on the joint that was opposite to the side of surgery. The asymmetry seemed to stem from the loading conditions that involved LB.

From a clinical standpoint, the results of this research have implications for both (1) osteoarthritis of the facets and (2) pain that originates from the capsular ligament. The first implication (osteoarthritis of the facets) is primarily derived from the findings of Study #1. Abnormal or increased motion of a joint may lead to subtle shifts in the load distribution on the articular surfaces. When this occurs, certain regions of the articular surface may be exposed to loading patterns to which they are unaccustomed and thus unable to accommodate. This initiates a cascade of degenerative changes in the cartilage which can ultimately lead to osteoarthritis and pain [16–18]. Several researchers have hypothesized that kinematic changes at the facet joint could give rise to osteoarthritis along this pathway [19,20]. However, at the present time, it is unknown exactly how large of a kinematic change would be required to do so. Nevertheless, the results from Study #1 did show that of the two microdiscectomy procedures, SD was the only one that significantly increased the motion of the facets along the primary directions of motion. Consequently, SD patients may be at a higher risk of developing osteoarthritis in their facet joints (particularly in the joint that is contralateral to the site of surgery). For a clinician, this knowledge could be useful for diagnostic purposes if an SD patient presents with low back pain in the years following their surgery.

Before discussing the second implication (pain that originates from the capsular ligament), there are two important points that should be made with respect to the strain threshold for pain. To begin with, throughout this document, the threshold has been portrayed rather simplistically. Twenty-one and a half percent strain has been presented as a clear demarcation between innocuous and painful strains that applies to every person in the population. In reality, the studies that have looked at non-physiological strains have shown that—at least in animals—there is significant variation in the strain threshold required to either activate potential nociceptors [21,65] or induce a pain response [22,23,68,69] (Section 3.2.2). Based on these studies, it is reasonable to assume that there would be a similar level of variation among humans. Therefore, it is perhaps more accurate to portray the threshold as a band as a reminder that the *actual* strain value is unique to each individual.

The second point that should be made is that even for a given person, the strain threshold for pain can change depending on the specific circumstances at hand. Inflammation illustrates this point well and is an especially pertinent example given the focus of this study. As previously mentioned, under normal conditions, nociceptors have a high mechanical threshold, firing only when they are strained to a noxious level. However, it has been demonstrated that under pathological conditions like inflammation, they may become sensitized and fire at lower thresholds. The altered pain sensation that ensues is thought to be produced by a litany of inflammatory mediators that elicit an excitatory effect from the sensory nerves. Substance P is an example of a naturally occurring inflammatory agent, and it has been identified in the lumbar facet capsules of the rat [109], rabbit [110], and human [111]. Furthermore, it has been shown to increase the discharge rate and lower the mechanical threshold of mechanosensitive afferent units in a rabbit model [66]. This suggests that surgically-related increases in strain that would not cause pain in a healthy individual may actually do so because of postoperative inflammation.

When interpreting the results from Study #2, the aforementioned points add an extra layer of complexity to the picture. However, despite the uncertainty in knowing an individual's exact strain threshold for pain, it can still be said that of the two microdiscectomy procedures, SD was the only one that significantly increased the capsular strains from their baseline values. And for at least a certain percentage of patients who undergo an SD, the observed increases are likely large enough to cause pain.

As discussed in Chapter 6, with the exception of ipsilateral AR, the increases in capsular strain only occurred under tensile loading conditions. The increases were especially acute in: (1) flexion, (2) flexion with right and left LB, and (3) LB ipsilateral to the site of surgery. This demonstrated that after SD, there are certain load combinations that increase the likelihood of surpassing the strain threshold for pain and putting the patient at risk for low back pain. Practically, there are several ways in which these findings could be translated to a clinical setting. For example, it would be prudent to advise SD patients to avoid or limit these types of motions, particularly in the early stages of recovery when inflammation is at its highest. SD patients may also benefit from physical therapy that specifically targets the antagonistic muscle groups for these motions. (These include: the erector spinae and latissimus dorsi for both flexion and LB; and the quadratus lumborum and external and internal obliques for LB [112].) This is important because while flexion and LB can be produced by voluntary muscle activity, they can also be initiated by gravity or some other acceleration that acts on the mass of the trunk. If the muscles responsible for countering an impulsive bending moment are too slow or weak to function effectively, then the moment will be transmitted to the intervertebral joint. This could potentially have painful repercussions for the patient, stemming from overstrained capsules.

7.4 Recommendations

There are several improvements that could be made if given the opportunity to further explore these hypotheses. First and foremost, this research would benefit greatly from increasing the sample size. The statistical analyses of hypotheses H_1 and H_2 were severely limited by their respective sample sizes. The linear mixed-effects regression models were able to identify significant differences between testing conditions in the pairwise comparisons; however, the comparisons were done with "lumped" variables that combined the data across motion tests (Study #1) or loading conditions (Study #2). Unfortunately, the models lacked sufficient data to identify *which* individual motion tests (or loading conditions) drove the significant differences. Though descriptive statistics helped fill the gaps in information, it would be ideal to back those conjectures with formal, statistical tests.

That being said, by approaching the statistical analyses in a different way, it may be possible to glean the desired information from the current data sets. Both of the completed analyses were essentially done with endpoint data. (The statistical models for Study #1 incorporated the facets' translational and rotational ROMs; and the models for Study #2 used the capsules' largest principal strains at the endpoint of each loading condition.) Rather than condensing the data sets in this way, one could also employ a curve-fitting technique. For example, the data from Study #2 consisted of sets of moment-strain curves for the various loading conditions considered in each testing condition. If a mathematical function was fit to each curve, the statistical analysis could be performed on the functions' parameters. A similar approach could be applied to the data from Study #1. This would be a way to pare down the data sets while still preserving the information from the entire length of the loading curves. Potentially, this could be a way to enhance the power of the statistical analyses.

Finally, future studies on facet kinematics and capsular ligament strains should explore additional types of loading, including: shear, tension and compression, FE combined with AR, and LB combined with AR. This study demonstrated that even when the total applied moment was the same, the facets exhibited more motion and larger capsular strains under combined FE with LB than they did when loaded in pure FE or LB. This was true in all three testing conditions. These findings confirmed the importance of considering combined loading in spinal biomechanics research, particularly when looking at non-pathological specimens.

7.5 Summary

This study looked at the effects of two increasingly invasive microdiscectomy procedures on the biomechanics of the lumbar facet joints. The more invasive of the two procedures resulted in increased motion of the facets and larger strains in the capsular ligament. Consequently, SD patients may have a higher risk of experiencing degenerative changes at the joint and pain that originates from the capsular ligament. These potential outcomes should be weighed by clinicians when settling on the course of treatment for their patients. Certainly there are cases where the patient's symptoms and medical history warrant the decision to perform an SD. But in situations where the choice is not as clear, the results of this study suggest that PD should be the preferred technique to preserve the biomechanics of the facet joints.

Appendix A. List of Abbreviations

AR	Axial rotation
CCW	Counterclockwise
CW	Clockwise
DIC	Digital image correlation
DOF	Degree of freedom
E1	First principal strain
E2	Second principal strain
Ext	Extension
FE	Flexion-extension
Flex	Flexion
FLLB	A multi-axis bending test in which flexion is applied with left lateral bending followed by extension with right lateral bending
FRE	Fiducial registration error
FRLB	A multi-axis bending test in which flexion is applied with right lateral bending followed by extension with left lateral bending
FSU	Functional spinal unit
HD	High definition
LB	Lateral bending
LBP	Low back pain
LVDT	Linear variable differential transducer
PCA	Principal components analysis
PD	Partial microdiscectomy
RMS	Root mean square
ROI	Region of interest
ROM	Range of motion
R_V	Rotational range of motion about the V-axis
R_W	Rotational range of motion about the W-axis
SD	Subtotal microdiscectomy
STL	Stereolithography

T_U	Translational range of motion along the U-axis
ZNSSD	Zero-mean normalized sum of squared difference
2D	Two-dimensional
3D	Three-dimensional

Appendix B. Translational and Rotational Ranges of Motion

The following figures present the translational and rotational ranges of motion (ROMs) of the L3 facets measured in Study #1. The data are ordered by motion test and testing condition. The bars are colored by axis, and the error bars represent one standard deviation from the mean.

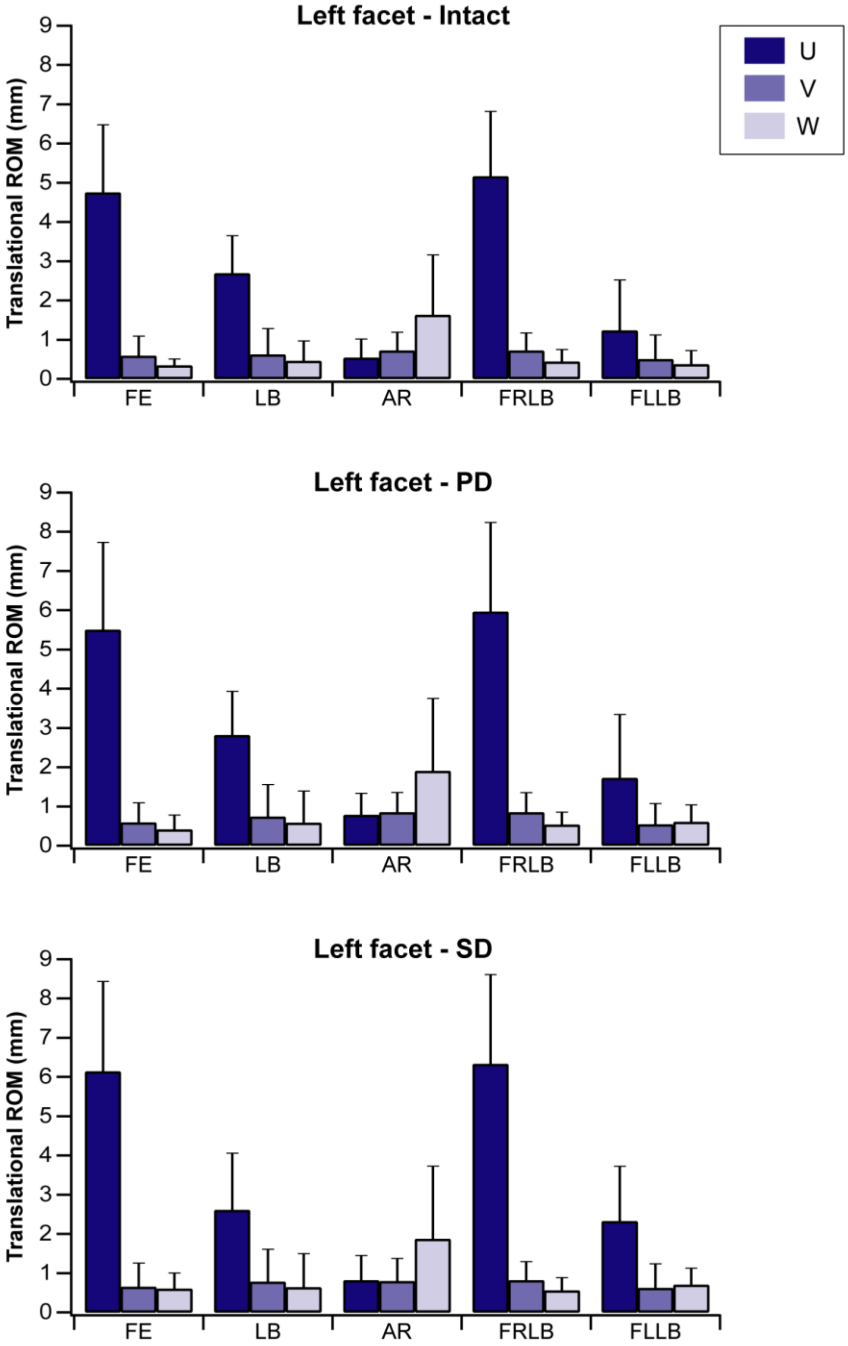

Figure B.1: Translational ROM of the L3 left facets (n = 9).

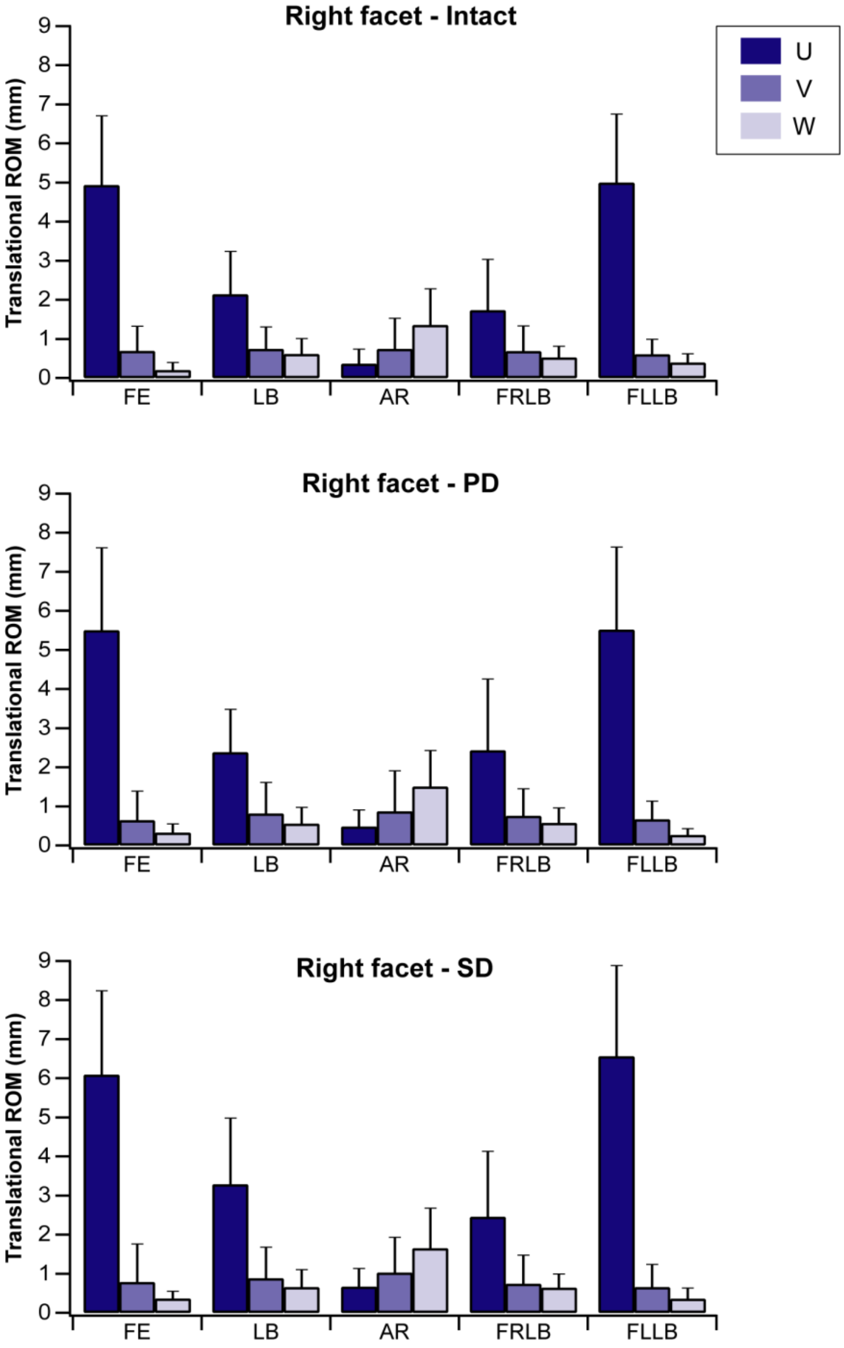

Figure B.2: Translational ROM of the L3 right facets (n = 9).

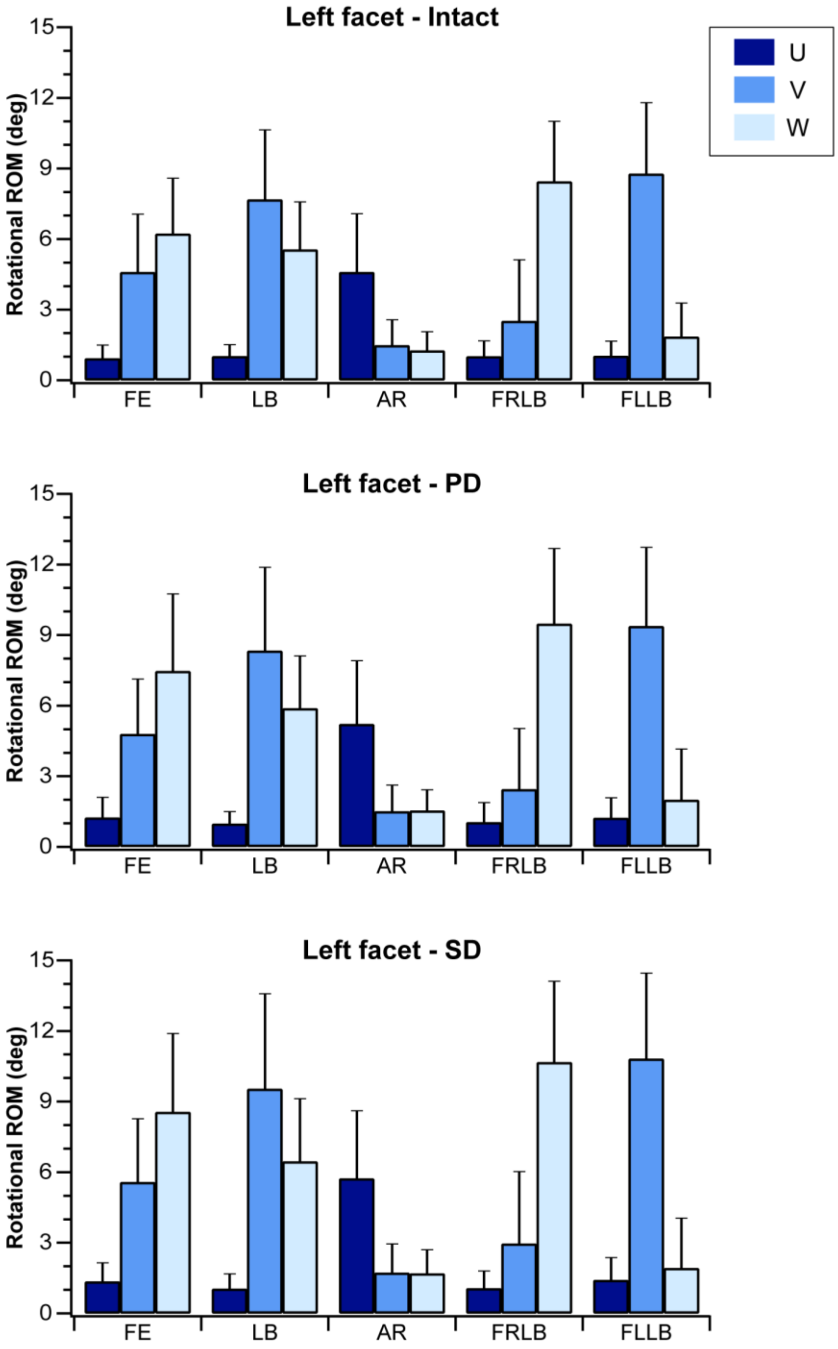

Figure B.3: Rotational ROM of the L3 left facets (n = 9).

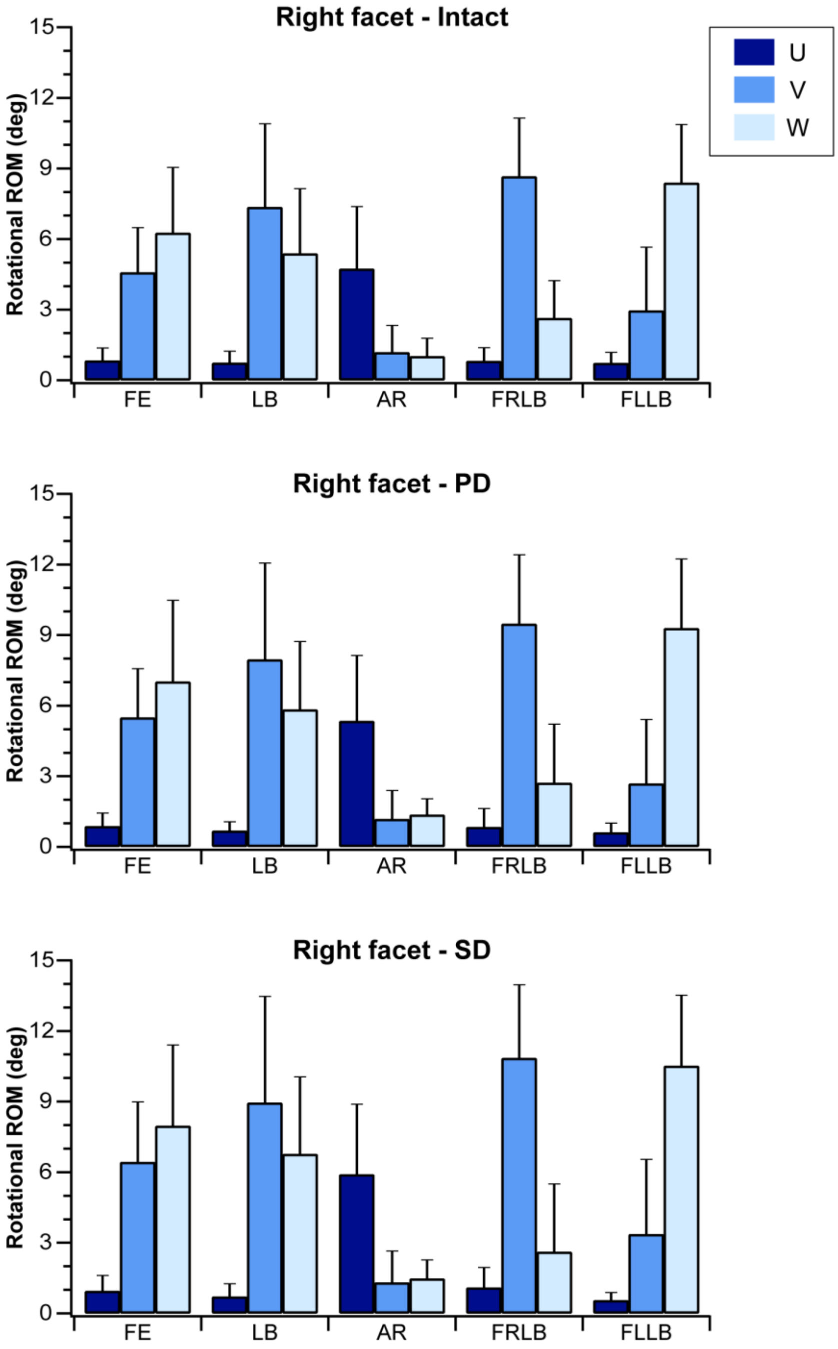

Figure B.4: Rotational ROM of the L3 right facets (n = 9).

Appendix C. Statistical Analysis for Study #1

Hypothesis H_1 was addressed with a linear mixed-effects regression model (Equation C.1).

$$Y = \beta_0 + \beta_1 X1 + \beta_2 X2 + \beta_3 Z1 + \beta_4 Z2 + \beta_5 Z3 + \beta_6 Z4 + b_i \tag{C.1}$$

where:

- Y = translational or rotational ROM.
- $X1$ and $X2$ = PD and SD conditions, respectively.
- $Z1 – Z4$ = motion tests LB, AR, FRLB, and FLLB, respectively.
- β_0 = mean Y for the intact condition and FE motion test.
- $\beta_{1\text{-}2}$ = mean difference in Y between the intact condition and the PD and SD conditions, respectively, combining the results from all motion tests.
- $\beta_{3\text{-}6}$ = mean difference in Y between the FE motion test and motion tests LB, AR, FRLB, and FLLB, respectively, combining the results from all testing conditions.
- b_i = estimated difference from β_0 for specimen i.

The assignment of which category was the reference category was arbitrary. Refer to Appendix A for the meanings of the abbreviations.

Appendix D. Statistical Analysis for Study #2

Hypothesis H_2 was addressed with a linear mixed-effects regression model (Equation D.1).

$$\begin{aligned} Y = \beta_0 + \beta_1 X1 + \beta_2 X2 + \beta_3 Z1 + \beta_4 Z2 + \beta_5 Z3 + \\ \beta_6 Z4 + \beta_7 Z5 + \beta_8 Z6 + \beta_9 Z7 + \beta_{10} Z8 + \beta_{11} Z9 + b_i \end{aligned} \tag{D.1}$$

where:

- Y = largest endpoint principal strain (E1 or E2).
- $X1$ and $X2$ = PD and SD conditions, respectively.
- $Z1 - Z9$ = loading conditions extension, right LB, left LB, CCW AR, CW AR, flexion with right LB, extension with left LB, flexion with left LB, and extension with right LB, respectively.
- β_0 = mean Y for the intact condition and flexion loading condition.
- $\beta_{1\text{-}2}$ = mean difference in Y between the intact condition and the PD and SD conditions, respectively, combining the results from all loading conditions.
- $\beta_{3\text{-}11}$ = mean difference in Y between the flexion loading condition and loading conditions extension, right LB, left LB, CCW AR, CW AR, flexion with right LB, extension with left LB, flexion with left LB, and extension with right LB, respectively, combining the results from all testing conditions.
- b_i = estimated difference from β_0 for specimen i.

The assignment of which category was the reference category was arbitrary. Refer to Appendix A for the meanings of the abbreviations.

References

[1] Moore, K. L., and Agur A. M. R., 2007, Essential clinical anatomy, Lippincott Williams and Wilkins, Philadelphia.

[2] Awad, J. N., and Moskovich, R., 2006, “Lumbar disc herniations: surgical versus nonsurgical treatment,” Clinical Orthopaedics and Related Research, 443, pp. 183–197.

[3] Hansen, J. T., and Netter, F. H., eds., 2010, Netter’s clinical anatomy, Saunders/Elsevier, Philadelphia.

[4] McCulloch, J. A., 1996, “Focus issue on lumbar disc herniation: macro- and microdiscectomy,” Spine, 21(24 Suppl), pp. 45S–56S.

[5] Blamoutier, A., 2013, “Surgical discectomy for lumbar disc herniation: surgical techniques,” Orthopaedics and Traumatology: Surgery and Research, 99(1), pp. S187–S196.

[6] Sherman, J., Cauthen, J., Schoenberg, D., Burns, M., Reaven, N. L., and Griffith, S. L., 2010, “Economic impact of improving outcomes of lumbar discectomy,” The Spine Journal, 10(2), pp. 108–116.

[7] O’Connell, J. E. A., 1951, “Protrusions of the lumbar intervertebral discs. A clinical review based on five hundred cases treated by excision of the protrusion,” The Journal of Bone and Joint Surgery British, 33(1), pp. 8–30.

[8] Williams, R. W., 1978, “Microlumbar discectomy: a conservative surgical approach to the virgin herniated lumbar disc,” Spine, 3(2), pp. 175–182.

[9] Spengler, D. M., Ouellette, E. A., Battié, M., and Zeh, J., 1990, “Elective discectomy for herniation of a lumbar disc. Additional experience with an objective method,” The Journal of Bone and Joint Surgery American, 72(2), pp. 230–237.

[10] McGirt, M. J., Ambrossi, G. L. G., Datoo, G., Sciubba, D. M., Witham, T. F., Wolinsky, J. P., Gokaslan, Z. L., and Bydon, A., 2009, “Recurrent disc herniation and long-term back pain after primary lumbar discectomy: review of outcomes reported for limited versus aggressive disc removal,” Neurosurgery, 64(2), pp. 338–344; discussion 344–345.

[11] Watters, W. C., 3rd, and McGirt, M. J., 2009, “An evidence-based review of the literature on the consequences of conservative versus aggressive discectomy for the treatment of primary disc herniation with radiculopathy,” The Spine Journal, 9(3), pp. 240–257.

[12] Lohmander, L. S., and Roos, H., 1994, “Knee ligament injury, surgery and osteoarthrosis. Truth or consequences?,” Acta Orthopaedica Scandinavica, 65(6), pp. 605–609.

[13] Roos, H., Adalberth, T., Dahlberg, L., and Lohmander, L. S., 1995, “Osteoarthritis of the knee after injury to the anterior cruciate ligament or meniscus: the influence of time and age,” Osteoarthritis and Cartilage, 3(4), pp. 261–267.

[14] Snyder-Mackler, L., 1995, “Fate of the ACL-injured patient: a prospective outcome study,” The American Journal of Sports Medicine, 23(3), pp. 372–373.

[15] Buckland-Wright, J. C., Lynch, J. A., and Dave, B., 2000, “Early radiographic features in patients with anterior cruciate ligament rupture,” Annals of the Rheumatic Diseases, 59(8), pp. 641–646.

[16] Andriacchi, T. P., Mündermann, A., Smith, R. L., Alexander, E. J., Dyrby, C. O., and Koo, S., 2004, “A framework for the in vivo pathomechanics of osteoarthritis at the knee,” Annals of Biomedical Engineering, 32(3), pp. 447–457.

[17] Andriacchi, T. P., Briant, P. L., Bevill, S. L., and Koo, S., 2006, “Rotational changes at the knee after ACL injury cause cartilage thinning,” Clinical and Orthopaedic Related Research, 442, pp. 39–44.

[18] Vincent, K. R., Conrad, B. P., Fregly, B. J., and Vincent, H. K., 2012, “The pathophysiology of osteoarthritis: a mechanical perspective on the knee joint,” Physical Medicine and Rehabilitation, 4(5), pp. S3–S9.

[19] Dunlop, R. B., Adams, M. A., and Hutton, W. C., 1984, “Disc space narrowing and the lumbar facet joints,” The Journal of Bone and Joint Surgery British, 66(5), pp. 706–710.

[20] Panjabi, M. M., Krag, M. H., and Chung, T. Q., 1984, “Effects of disc injury on mechanical behavior of the human spine,” Spine, 9(7), pp. 707–713.

[21] Lu, Y., Chen, C., Kallakuri, S., Patwardhan, A., and Cavanaugh, J. M., 2005, “Neurophysiological and biomechanical characterization of goat cervical facet joint capsules,” Journal of Orthopaedic Research, 23(4), pp. 779–787.

[22] Lee, K. E., Thinnes, J. H., Gokhin, D. S., and Winkelstein, B. A., 2004, “A novel rodent neck pain model of facet-mediated behavioral hypersensitivity: implications for persistent pain and whiplash injury,” Journal of Neuroscience Methods, 137(2), pp. 151–159.

[23] Dong, L., Odeleye, A. O., Jordan-Sciutto, K. L., and Winkelstein, B. A., 2008, “Painful facet joint injury induces neuronal stress activation in the DRG: implications for cellular mechanisms of pain,” Neuroscience Letters, 443(2), pp. 90–94.

[24] Bogduk, N., 1997, Clinical anatomy of the lumbar spine and sacrum, Churchill Livingstone, New York.

[25] Hickey, D. S., and Hukins, D. W., 1980, “Relation between the structure of the annulus fibrosus and the function and failure of the intervertebral disc,” Spine, 5(2), pp. 106–116.

[26] Raj, P. P., 2008, “Intervertebral disc: anatomy-physiology-pathophysiology-treatment,” Pain Practice, 8(1), pp. 18–44.

[27] Thompson, J. C., and Netter, F. H., 2010, Netter’s concise orthopaedic anatomy, Saunders Elsevier, Philadelphia, PA.

[28] Masharawi, Y., Rothschild, B., Dar, G., Peleg, S., Robinson, D., Been, E., and Hershkovitz, I., 2004, “Facet orientation in the thoracolumbar spine: three-dimensional anatomic and biomechanical analysis,” Spine, 29(16), pp. 1755–1763.

[29] Yoganandan, N., Knowles, S. A., Maiman, D. J., and Pintar, F. A., 2003, “Anatomic study of the morphology of human cervical facet joint,” Spine, 28(20), pp. 2317–2323.

[30] Womack, W., Woldtvedt, D., and Puttlitz, C. M., 2008, “Lower cervical spine facet cartilage thickness mapping,” Osteoarthritis and Cartilage, 16(9), pp. 1018–1023.

[31] Woldtvedt, D. J., Womack, W., Gadomski, B. C., Schuldt, D., and Puttlitz, C. M., 2011, “Finite element lumbar spine facet contact parameter predictions are affected by the cartilage thickness distribution and initial joint gap size,” Journal of Biomechanical Engineering, 133(6), pp. 0610091-0610097.

[32] Pierce, D. M., Trobin, W., Trattnig, S., Bischof, H., and Holzapfel, G. A., 2009, “A phenomenological approach toward patient-specific computational modeling of articular cartilage including collagen fiber tracking,” Journal of Biomechanical Engineering, 131(9), pp. 0910061-09100612.

[33] Browne, J. E., and Branch, T. P., 2000, “Surgical alternatives for treatment of articular cartilage lesions,” Journal of the American Academy of Orthopaedic Surgeons, 8(3), pp. 180–189.

[34] Engel, R., and Bogduk, N., 1982, “The menisci of the lumbar zygapophysial joints,” Journal of Anatomy, 135(Pt 4), pp. 795–809.

[35] Sato, S., Oguma, H., Murakami, G., and Noriyasu, S., 2002, “Morphometrical study of the joint surface and capsule of the lumbar zygapophysial joint with special reference to their laterality,” Okajimas Folia Anatomica Japonica, 79(1), pp. 43–53.

[36] Yamashita, T., Minaki, Y., Özaktay, A. C., Cavanaugh, J. M., and King, A. I., 1996, “A morphological study of the fibrous capsule of the human lumbar facet joint,” Spine, 21(5), pp. 538–543.

[37] Wood, K. B., Schendel, M. J., Pashman, R. S., Buttermann, G. R., Lewis, J. L., Ogilvie, J. W., and Bradford, D. S., 1992, “In vivo analysis of canine intervertebral and facet motion,” Spine, 17(10), pp. 1180–1186.

[38] McLain, R. F., Yerby, S. A., and Moseley, T. A., 2002, “Comparative morphometry of L4 vertebrae: comparison of large animal models for the human lumbar spine,” Spine, 27(8), pp. E200–E206.

[39] Ledet, E. H., Sanders, G. P., Jackson, J. L. M., Wagner, C., and Tymeson, M. P., 2010, “A comprehensive interspecies comparison of commonly used animal models for study of the human lumbar spine,” The Spine Journal, 10(9), p. S59.

[40] Kozanek, M., Wang, S., Passias, P. G., Xia, Q., Li, G., Bono, C. M., Wood, K. B., and Li, G., 2009, “Range of motion and orientation of the lumbar facet joints in vivo,” Spine, 34(19), pp. E689–E696.

[41] Jegapragasan, M., Cook, D. J., Gladowski, D. A., Kanter, A. S., and Cheng, B. C., 2011, “Characterization of articulation of the lumbar facets in the human cadaveric spine using a facet-based coordinate system,” The Spine Journal, 11(4), pp. 340–346.

[42] Panjabi, M. M., Oxland, T., Takata, K., Goel, V., Duranceau, J., and Krag, M., 1993, “Articular facets of the human spine. Quantitative three-dimensional anatomy,” Spine, 18(10), pp. 1298–1310.

[43] Winkelstein, B. A., McLendon, R. E., Barbir, A., and Myers, B. S., 2001, “An anatomical investigation of the human cervical facet capsule, quantifying muscle insertion area,” Journal of Anatomy, 198(4), pp. 455-461.

[44] Chen, C., Lu, Y., Kallakuri, S., Patwardhan, A., and Cavanaugh, J. M., 2006, “Distribution of A-delta and C-fiber receptors in the cervical facet joint capsule and their response to stretch,” The Journal of Bone and Joint Surgery American, 88(8), pp. 1807-1816.

[45] Panjabi, M. M., Goel, V. K., and Takata, K., 1982, “Physiologic strains in the lumbar spinal ligaments. An in vitro biomechanical study,” Spine, 7(3), pp. 192–203.

[46] Winkelstein, B. A., Nightingale, R. W., Richardson, W. J., and Myers, B. S., 2000, “The cervical facet capsule and its role in whiplash injury: a biomechanical investigation,” Spine, 25(10), pp. 1238–1246.

[47] Ianuzzi, A., Little, J. S., Chiu, J. B., Baitner, A., Kawchuk, G., and Khalsa, P. S., 2004, “Human lumbar facet joint capsule strains: I. During physiological motions,” The Spine Journal, 4(2), pp. 141–152.

[48] Hoffman, A. H., and Grigg, P., 1984, “A method for measuring strains in soft tissue,” Journal of Biomechanics, 17(10), pp. 795–800.

[49] Adams, M. A., and Dolan, P., 1991, “A technique for quantifying the bending moment acting on the lumbar spine in vivo,” Journal of Biomechanics, 24(2), pp. 117–126.

[50] Jaumard, N. V., Bauman, J. A., Welch, W. C., and Winkelstein, B. A., 2011, “Pressure measurement in the cervical spinal facet joint: considerations for maintaining joint anatomy and an intact capsule,” Spine, 36(15), pp. 1197-1203.

[51] Wong, M., and Carter, D., 2003, “Articular cartilage functional histomorphology and mechanobiology: a research perspective,” Bone, 33(1), pp. 1-13.

[52] Lee, J. H., Kisiday, J., and Grodzinsky, A. J., 2003, “Tissue-engineered versus native cartilage: linkage between cellular mechano-transduction and biomechanical properties,” Novartis Foundation Symposium, 249, pp. 52-64; discussion 64-69, 170-174, 239-241.

[53] Papachristou, D. J., Papachroni, K. K., Basdra, E. K., and Papavassiliou, A. G., 2009, “Signaling networks and transcription factors regulating mechanotransduction in bone,” BioEssays, 31(7), pp. 794-804.

[54] Ramage, L., Nuki, G., and Salter, D. M., 2009, “Signalling cascades in mechanotransduction: cell-matrix interactions and mechanical loading,” Scandinavian Journal of Medicine and Science in Sports, 19(4), pp. 457-469.

[55] Cavanaugh, J. M., Özaktay, A. C., Yamashita, H. T., and King, A. I., 1996, “Lumbar facet pain: biomechanics, neuroanatomy and neurophysiology,” Journal of Biomechanics, 29(9), pp. 1117-1129.

[56] Elder, B. D., Kim, D. H., and Athanasiou, K. A., 2010, “Developing an articular cartilage decellularization process toward facet joint cartilage replacement,” Neurosurgery, 66(4), pp. 722-727; discussion 727.

[57] Guyton, A. C., and Hall, J. E., 2000, Textbook of medical physiology, Saunders, Philadelphia.

[58] Ashton, I. K., Ashton, B. A., Gibson, S. J., Polak, J. M., Jaffray, D. C., and Eisenstein, S. M., 1992, “Morphological basis for back pain: the demonstration of nerve fibers and neuropeptides in the lumbar facet joint capsule but not in ligamentum flavum,” Journal of Orthopaedic Research, 10(1), pp. 72–78.

[59] McLain, R. F., and Pickar, J. G., 1998, “Mechanoreceptor endings in human thoracic and lumbar facet joints,” Spine, 23(2), pp. 168–173.

[60] Mann, F. A., Constantinescu, G. M., and Yoon, H.-Y., 2011, Fundamentals of small animal surgery, John Wiley and Sons, Hoboken.

[61] Cavanaugh, J. M., el-Bohy, A., Hardy, W. N., Getchell, T. V., Getchell, M. L., and King, A. I., 1989, “Sensory innervation of soft tissues of the lumbar spine in the rat,” Journal of Orthopaedic Research, 7(3), pp. 378–388.

[62] Yamashita, T., Cavanaugh, J. M., el-Bohy, A. A., Getchell, T. V., and King, A. I., 1990, “Mechanosensitive afferent units in the lumbar facet joint,” The Journal of Bone and Joint Surgery American, 72(6), pp. 865–870.

[63] Avramov, A. I., Cavanaugh, J. M., Özaktay, A. C., Getchell, T. V., and King, A. I., 1992, “The effects of controlled mechanical loading on group-II, III, and IV afferent units from the lumbar facet joint and surrounding tissue. An in vitro study,” The Journal of Bone and Joint Surgery American, 74(10), pp. 1464–1471.

[64] Pickar, J. G., and McLain, R. F., 1995, “Responses of mechanosensitive afferents to manipulation of the lumbar facet in the cat,” Spine, 20(22), pp. 2379–2385.

[65] Lu, Y., Chen, C., Kallakuri, S., Patwardhan, A., and Cavanaugh, J. M., 2005, “Neural response of cervical facet joint capsule to stretch: a study of whiplash pain mechanism,” Stapp Car Crash Journal, 49, pp. 49–65.

[66] Yamashita, T., Cavanaugh, J. M., Özaktay, A. C., Avramov, A. I., Getchell, T. V., and King, A. I., 1993, “Effect of substance P on mechanosensitive units of tissues around and in the lumbar facet joint,” Journal of Orthopaedic Research, 11(2), pp. 205–214.

[67] Özaktay, A. C., Cavanaugh, J. M., Blagoev, D. C., Getchell, T. V., and King, A. I., 1994, “Effects of a carrageenan-induced inflammation in rabbit lumbar facet joint capsule and adjacent tissues,” Neuroscience Research, 20(4), pp. 355–364.

[68] Lee, K. E., Davis, M. B., Mejilla, R. M., and Winkelstein, B. A., 2004, “In vivo cervical facet capsule distraction: mechanical implications for whiplash and neck pain,” Stapp Car Crash Journal, 48, pp. 1–23.

[69] Winkelstein, B. A., and Santos, D. G., 2008, “An intact facet capsular ligament modulates behavioral sensitivity and spinal glial activation produced by cervical facet joint tension,” Spine, 33(8), pp. 856–862.

[70] Little, J. S., and Khalsa, P. S., 2005, “Material properties of the human lumbar facet joint capsule,” Journal of Biomechanical Engineering, 127(1), pp. 15-24.

[71] Adams, M. A., Bogduk, N., Burton, K., and Dolan, P., 2012, The biomechanics of back pain, Elsevier, Edinburgh.

[72] Lee, M. J., Bransford, R. J., Bellabarba, C., Chapman, J. R., Cohen, A. M., Harrington, R. M., and Ching, R. P., 2010, “The effect of bilateral laminotomy versus laminectomy on the motion and stiffness of the human lumbar spine: a biomechanical comparison,” Spine, 35(19), pp. 1789–1793.

[73] Cook, D. J., and Cheng, B. C., 2010, “Development of a model based method for investigating facet articulation,” Journal of Biomechanical Engineering, 132(6), p. 0645041-0645046.

[74] Rohlmann, A., Mann, A., Zander, T., and Bergmann, G., 2009, “Effect of an artificial disc on lumbar spine biomechanics: a probabilistic finite element study,” European Spine Journal, 18(1), pp. 89–97.

[75] Baker, R., 2003, “ISB recommendation on definition of joint coordinate systems for the reporting of human joint motion-part I: ankle, hip and spine,” Journal of Biomechanics, 36(2), pp. 300–302; author reply 303–304.

[76] Craig, J. J., 1989, Introduction to robotics: mechanics and control, Addison-Wesley, Reading, Mass.

[77] Fitzpatrick, J. M., West, J. B., and Maurer, C. R., 1998, “Predicting error in rigid-body point-based registration,” IEEE Transactions on Medical Imaging, 17(5), pp. 694–702.

[78] Hajnal, J. V., Hill, D. L. G., and Hawkes, D. J., 2001, Medical image registration, CRC Press, Boca Raton.

[79] Goel, V. K., Goyal, S., Clark, C., Nishiyama, K., and Nye, T., 1985, “Kinematics of the whole lumbar spine. Effect of discectomy,” Spine, 10(6), pp. 543–554.

[80] Kuroki, H., Goel, V. K., Holekamp, S. A., Ebraheim, N. A., Kubo, S., and Tajima, N., 2004, “Contributions of flexion-extension cyclic loads to the lumbar spinal segment stability following different discectomy procedures,” Spine, 29(3), pp. E39–46.

[81] Sutton, M., Wolters, W., Peters, W., Ranson, W., and McNeill, S., 1983, “Determination of displacements using an improved digital correlation method,” Image and Vision Computing, 1(3), pp. 133–139.

[82] Sztefek, P., Vanleene, M., Olsson, R., Collinson, R., Pitsillides, A. A., and Shefelbine, S., 2010, “Using digital image correlation to determine bone surface strains during loading and after adaptation of the mouse tibia,” Journal of Biomechanics, 43(4), pp. 599–605.

[83] An, B., Liu, Y., Arola, D., and Zhang, D., 2011, “Fracture toughening mechanism of cortical bone: An experimental and numerical approach,” Journal of the Mechanical Behavior of Biomedical Materials, 4(7), pp. 983–992.

[84] Dickinson, A. S., Taylor, A. C., Ozturk, H., and Browne, M., 2011, “Experimental Validation of a Finite Element Model of the Proximal Femur Using Digital Image Correlation and a Composite Bone Model,” Journal of Biomechanical Engineering, 133(1), p. 0145041-0145046.

[85] Szabó, M. E., Zekonyte, J., Katsamenis, O. L., Taylor, M., and Thurner, P. J., 2011, “Similar damage initiation but different failure behavior in trabecular and cortical bone tissue,” Journal of the Mechanical Behavior of Biomedical Materials, 4(8), pp. 1787–1796.

[86] Amin Yavari, S., van der Stok, J., Weinans, H., and Zadpoor, A. A., 2013, “Full-field strain measurement and fracture analysis of rat femora in compression test,” Journal of Biomechanics, 46(7), pp. 1282–1292.

[87] Väänänen, S. P., Amin Yavari, S., Weinans, H., Zadpoor, A. A., Jurvelin, J. S., and Isaksson, H., 2013, “Repeatability of digital image correlation for measurement of surface strains in composite long bones,” Journal of Biomechanics, 46(11), pp. 1928–1932.

[88] Wang, C. C.-B., Deng, J.-M., Ateshian, G. A., and Hung, C. T., 2002, “An automated approach for direct measurement of two-dimensional strain distributions within articular cartilage under unconfined compression,” Journal of Biomechanical Engineering, 124(5), pp. 557-567.

[89] Lai, J. H., and Levenston, M. E., 2010, “Meniscus and cartilage exhibit distinct intra-tissue strain distributions under unconfined compression,” Osteoarthritis and Cartilage, 18(10), pp. 1291–1299.

[90] Gao, L.L., Zhang, C.Q., Yang, Y.B., Shi, J.P., and Jia, Y.W., 2013, “Depth-dependent strain fields of articular cartilage under rolling load by the optimized digital image correlation technique,” Materials Science and Engineering: C, 33(4), pp. 2317–2322.

[91] Kelleher, J. E., Zhang, K., Siegmund, T., and Chan, R. W., 2010, “Spatially varying properties of the vocal ligament contribute to its eigenfrequency response,” Journal of the Mechanical Behavior of Biomedical Materials, 3(8), pp. 600–609.

[92] Cheng, T., and Gan, R. Z., 2008, “Experimental measurement and modeling analysis on mechanical properties of tensor tympani tendon,” Medical Engineering and Physics, 30(3), pp. 358–366.

[93] Abraham, A. C., Kaufman, K. R., and Haut Donahue, T. L., 2013, “Phenomenological consequences of sectioning and bathing on passive muscle mechanics of the New Zealand white rabbit tibialis anterior,” Journal of the Mechanical Behavior of Biomedical Materials, 17, pp. 290–295.

[94] International Workshop on Vision Algorithms, 2000, Vision algorithms: theory and practice: International Workshop on Vision Algorithms, Corfu, Greece, September 21-22, 1999: proceedings, Springer, Berlin; New York.

[95] Sutton, M. A., 2009, Image correlation for shape, motion and deformation measurements: basic concepts, theory and applications, Springer, New York.

[96] Schreier, H. W., and Sutton, M. A., 2002, “Systematic errors in digital image correlation due to undermatched subset shape functions,” Experimental Mechanics, 42(3), pp. 303–310.

[97] Reu, P., 2012, “Hidden Components of 3D-DIC: Interpolation and Matching - Part 2,” Experimental Techniques, 36(3), pp. 3–4.

[98] Lava, P., Coppieters, S., Wang, Y., Van Houtte, P., and Debruyne, D., 2011, “Error estimation in measuring strain fields with DIC on planar sheet metal specimens with a non-perpendicular camera alignment,” Optics and Lasers in Engineering, 49(1), pp. 57–65.

[99] Lava, P., Cooreman, S., Coppieters, S., De Strycker, M., and Debruyne, D., 2009, “Assessment of measuring errors in DIC using deformation fields generated by plastic FEA,” Optics and Lasers in Engineering, 47(7-8), pp. 747–753.

[100] Reu, P., 2012, “Stereo-rig design: creating the stereo-rig layout - Part 1,” Experimental Techniques, 36(5), pp. 3–4.

[101] Taubin, G., 1991, “Estimation of planar curves, surfaces, and nonplanar space curves defined by implicit equations with applications to edge and range image segmentation,” IEEE Transactions on Pattern Analysis and Machine Intelligence, 13(11), pp. 1115-1138.

[102] Siegmund, G. P., Myers, B. S., Davis, M. B., Bohnet, H. F., and Winkelstein, B. A., 2001, “Mechanical evidence of cervical facet capsule injury during whiplash: a cadaveric study using combined shear, compression, and extension loading,” Spine, 26(19), pp. 2095–2101.

[103] Zhang, D., and Arola, D. D., 2004, “Applications of digital image correlation to biological tissues,” Journal of Biomedical Optics, 9(4), pp. 691–699.

[104] Adams, M. A., and Hutton, W. C., 1981, “The relevance of torsion to the mechanical derangement of the lumbar spine,” Spine, 6(3), pp. 241-248.

[105] Chimich, D., Shrive, N., Frank, C., Marchuk, L., and Bray, R., 1992, “Water content alters viscoelastic behaviour of the normal adolescent rabbit medial collateral ligament,” Journal of Biomechanics, 25(8), pp. 831–837.

[106] Haut, T. L., and Haut, R. C., 1997, “The state of tissue hydration determines the strain-rate-sensitive stiffness of human patellar tendon,” Journal of Biomechanics, 30(1), pp. 79–81.

[107] Atkinson, T. S., Ewers, B. J., and Haut, R. C., 1999, “The tensile and stress relaxation responses of human patellar tendon varies with specimen cross-sectional area,” Journal of Biomechanics, 32(9), pp. 907–914.

[108] Thornton, G. M., Shrive, N. G., and Frank, C. B., 2001, “Altering ligament water content affects ligament pre-stress and creep behaviour,” Journal of Orthopaedic Research, 19(5), pp. 845–851.

[109] Ohtori, S., Takahashi, K., Chiba, T., Yamagata, M., Sameda, H., and Moriya, H., 2000, "Substance P and calcitonin gene-related peptide immunoreactive sensory DRG neurons innervating the lumbar facet joints in rats," Autonomic Neuroscience, 86(1-2), pp. 13-17.

[110] El-Bohy, A., Cavanaugh, J. M., Getchell, M. L., Bulas, T., Getchell, T. V., and King, A. I., 1998, "Localization of substance P and neurofilament immunoreactive fibers in the lumbar facet joint capsule and supraspinous ligament of the rabbit," Brain Research, 460(2), pp. 379-382.

[111] Beaman, D. N., Graziano, G. P., Glover, R. A., Wojtys, E. M., and Chang, V., 1993, "Substance P innervation of lumbar spine facet joints," Spine, 18(8), pp. 1044-1049.

[112] Clarkson, H. M., 2000, Musculoskeletal assessment: joint range of motion and manual muscle strength, Lippincott Williams and Wilkins, Philadelphia.